Characterization of unsteady multiphase flows in stormwater management applications

by

Jue Wang

A dissertation submitted to the Graduate Faculty of
Auburn University
in partial fulfillment of the
requirements for the Degree of
Doctor of Philosophy

Auburn, Alabama
December 15, 2018

Keywords: Geysering, Multi-phase, Resuspension, Sediment Basin, Surge, Unsteady Flow

Approved by

Jose G. Vasconcelos, Chair, Associate Professor of Civil Engineering
Xing Fang, Arthur H. Feagin Professor of Civil Engineering
Wesley C. Zech, Brasfield & Gorrie Professor of Construction Engineering and Management
Jeyhoon M. Khodadadi, Alumni Professor of Mechanical Engineering

Abstract

Intense rain events create many issues in urban areas, including flooding, overflows in stormwater systems, sediment pollution, etc. In many circumstances, flows are unsteady and characterized by multiphase flow conditions, which may lead to many difficulties when trying to understand flow characteristics and solve eventual operational problems. To understand the flow characteristics under such conditions, computational fluid dynamics (CFD) simulations, as well as field-scale experiments, were performed in this research.

Uncontrolled air pockets released from water-filled shafts can lead to geysering in stormwater systems. Such occurrences are deleterious from a public health and environmental standpoint and can cause property and structural damage. Causes, frequency, magnitude, and location of geysering events remain poorly understood, and pose practical difficulties for the design of dropshafts geometries that are less likely to experience such events. This work presents numerical investigations on air-related geysers that aims to gain insights on the mechanisms of entrapped air pocket releases and water displacement in vertical shafts. A CFD model was calibrated with experimental data and then was subsequently used in a larger geometry that allowed for the evaluation of air pocket release kinematics for a wider range of conditions. Among various findings, it was shown that water displacement was linked to entrapped air pocket volumes, initial water level in shafts and shaft diameter. In worst case conditions the displacement of free surface reached over 300% of the initial water level in the shaft. A retrofit strategy for vertical shaft geometries is proposed and evaluated with a CFD model for geyser mitigation.

Manhole cover displacement is also a hazardous operational issue that may occur in stormwater systems undergoing rapid filling during intense rain events. In various instances, the water free surface within vertical shafts can change rapidly. It is possible that the air located in the headspace of manholes will pressurize when the manhole is insufficiently ventilated. Air pressurization or direct water impact can lead to the displacement of manhole covers, with obvious impacts to the safety of pedestrians and vehicular traffic. Yet, investigations on this topic

have been limited. This work presents a study on the conditions for manhole cover displacement in shafts undergoing inertial oscillations or experiencing sudden release of entrapped air pockets. Numerical results showed that pressures associated with the sudden release of air pockets have much greater potential to cause manhole cover displacements when compared to air pressurization created by inertial oscillations within shafts. It is expected that results from this work could help mitigate such hazardous conditions.

Another application regarding unsteady multiphase flows is on flows in sediment basins. Sediment basins provide quiescent conditions that enable settling of fine particles present in runoff, mitigating environmental impacts created by excessive sediment discharges. The design of sediment basins is mostly based on empirically-based recommendations. Yet, details of the flows and settling conditions during filling and dewatering processes in sediment basins are not fully understood. The present work collected experimental data of the turbidity distribution and variation, and performed a particle size characterization in a large-scale test sediment basin to evaluate the performance of various basin treatment configurations. The result indicated that the Lamella High Rate Settler treatment with the longitudinal flow direction configuration presented the highest relative decrease in turbidity values. It also presented a more pronounced drop in turbidity between the basin inlet and outlet regions over a sequence of runs where sediments were not cleaned in the basin. The research results indicate that the small-scale high-rate settler (SSHRS) combined with the use of flocculant (PAM) can significantly reduce the turbidity of water discharged through skimmer. A series of CFD simulations were performed to assess the flow conditions for different basin length-width aspect ratios, as well as the effect of porous baffles on sediment basin flows. One outcome of this work was a model that can be used to evaluate flow conditions in sediment basins with porous baffles during filling stages.

In addition to the settling process in sediment basins, the settled particles are susceptible to undesired resuspension if, during dewatering of the basin, new flows are admitted and create an increase in velocities, shear forces, and turbulence near the basin bottom. A numerical study was performed to evaluate the benefits of confinement cells as a lining strategy for the bottom of sediment basins. CFD modeling was used to determine which geometries of confinement cells and flow conditions were more likely to succeed in decreasing turbulence and shear forces

within confinement cells. Through a comparison between experimental turbidity results and CFD modeling results, it was found a significant decrease in effluent turbidity was linked to the flow patterns in which two circulation zones appeared within the cells.

In summary, the present research mainly explores the use of CFD, as well as field experiments, to describe flows in the application of stormwater management. The major contributions include: 1) to understand the flow characteristics of air-water interactions in stormwater systems undergoing rapid filling and provide guidelines for designers on solving relevant problems associated with air-water flows; 2) to test the performance of various configurations of sediment basins and confinement cell systems in reducing water turbidity and to develop CFD models that aid in the description of flow conditions.

Acknowledgments

I highly appreciate my PhD advisor Dr. Jose Vasconcelos for his great and patient mentoring on my study and research. Dr. Vasconcelos led me into the realm of hydraulics, particularly the research topics regarding computational fluid dynamics on solving air-water two phase flows. This precious research experience will be a great foundation for my future professional career. The profession in academia of Dr. Vasconcelos is a perfect template that I will learn from and follow for my whole life. In addition to academic instructions, I also received a lot of care and encouragement from Dr. Vasconcelos, without which I may not be able to finish my PhD study.

I highly appreciate Dr. Xing Fang, Dr. Wesley Zech, and Dr. Jay Khodadadi for being my dissertation committee member, and Dr. Roy Knight for being the university reader. I took courses from you and/or worked with you. I not only learned knowledge from you but also learned the way to be professional in academia. I also appreciate other professors that I took courses from or worked with, including Dr. Prabhakar Clement, Dr. Frances O'Donnell, and Dr. Ash Abebe.

I would like to show my special thanks to Dr. Michael Perez for his work and help during my PhD training. Dr. Perez performed highly professionally when we worked together and he is the best colleague I've ever worked with. Dr. Perez also offered me a lot of constructive suggestions on my professional development, which is very important for me to develop my career plan.

I want to thank Mrs. Nikki Muller, Mr. Tim Simpson, Mr. Guy Savage, Dr. Mitchell Moore, Miss Juliana Kaiber da Silva and Mr. Bojun Dan. Without your hard work and instructive discussion, I would not be able to complete my research as I've done now. I also want to thank other colleagues and friends, including Miss Yasemin Eldayih, Miss Merve Cetin, Miss Egemen Caglar, Mr. Wenjun Song, Mr. Xiaoning Li, Dr. Gang Chen, Dr. Liping Jiang, Dr. Song Gao, Dr. Xinyu Zhao, Dr. Liang Tang, Mrs. Jiayi Xu, Dr. Hao Wu, Mr. Qian Liang,

Mr. Yusheng Ding, Mrs. Yawei Chen, Mr. Kang Sun, Mrs. Jie Zhang, and etc. Without your accompany, I will lose a lot of happiness during the past years. I would also appreciate the friends that appear in my life but were absent in the past years, it was you that made me what I am.

I also want to thank Mr. Ted Gibson and Mrs. Sherry Gibson and their families. You helped me and my wife so much to get familiar with this country and its culture and make us feel we have a family here at Auburn, which is a strong support for us to keep studying here.

This work would also thank the Alabama Supercomputer Center (ASC) for providing computing resources.

In the end, I want to show my appreciation to my parents Mr. Wenxuan Wang and Mrs. Xiaoping Wang, parents in law Mr. Jiwen Zhang and Mrs. Yuefen Xing and other family members. Thank you for your understanding of our leaving you for such a far distance and long time. I want to thank my wife Shuwei Zhang for your love, understanding, accompany, and support. You are the ultimate motivation that makes me move on without fear. I will always love you.

This dissertation is dedicated in loving memory to my grandmother Mrs. Daju Wang.

Table of Contents

List of Figures

List of Tables

List of Symbols

A	Cross sectional area of the pipe
A_f	Cross sectional area of the flow
A_s	Cross sectional area of the shaft
A_v	Ventilation area
A_v^*	Normalized A_v
B	Top width of the flow
c	Wave celerity
c_0	Initial conditions of the wave celerity
C_p	Specific heat
$C_.$	Constant value
dx	Mesh size
D	Tunnel diameter
D_p	Diameter of particles making the porous media
D_s	Vertical shaft diameter
D_s^*	Normalized D_s
D_T	Tank diameter
D_v	Darcy coefficient or viscous resistance
e	Porosity of the porous media

F_1	A blending function
F_S	Surface tension force
g	Gravity acceleration
h	Pressure head
h_a	Peak compressed air pressure head
h_a^*	Normalized h_a
h_{pc}^*	Normalized h_{pc}
H_c	Height of CCS cells
H^*	Initial air pressure head in the chamber
I	Inertial coefficient or inertial resistance
k	Turbulence kinetic energy
k_T	Thermal conductivity
L	Vertical shaft length
L_1	Distance separation between every two air pockets
L_p	Porous media length in the flow direction
L_P	Pipe length
$m_{a,0}$	Initial air pocket mass
NTU	Water turbidity in NTU
p	Pressure
P	A production term related to shear stress
$P_{eb}\&P_{kb}$	Influence of buoyancy forces

P_k Turbulence production due to viscous forces

$p_{down,0}$ Pressure at downstream of dambreak problem

$p_{up,0}$ Pressure at upstream of dambreak problem

Q Flow rate

Q_0 Initial flow rate admitted in the surge tank

R_P Resuspension parameter

S Surge tank water level

S_0 Channel slope

S_f Friction slope

S_T Energy source term

$S_{\vec{U}}$ Momentum source term

t Time

t^* Normalized t

t_0 Duration of releasing of air pocket

t_1 Duration between every two air pockets being released

T Temperature

T_h Oscillation period that is estimated for a hydro-pneumatic chamber

T_o Period of surge oscillation

U Average water velocity reaching the surge tank

$\vec{U}$ Flow velocity

$\vec{U}_i^n$ Flow velocity at node i and n^{th} time step

$\vec{U_r}$	Velocity field suitable to compress the interface
V_0	Initial conditions of the flow velocity
V_a	Volume of air pocket
V_{am}	Ambient flow velocity
V_a^*	Normalized vV_a
V_{int}	Peak velocity at the soil interface
V_x	Flow velocity
$\forall$	Air volume in the air chamber
W	Initial water level in the shaft
W_c	Width of CCS cells
x	Location at x dimension
y	Water depth
y_0	Initial water depth
Y_{FS}	Displacement of water free surface
Y_{Int}	Displacement of air-water interface
$Y*$	Normalized veridical coordinate
α	Fraction of water in the cell
$\beta\cdot$	Constant value
γ	Constant value
Δp	Pressure loss

ΔQ	Change in upward water flow rate associated to the impact of the rising water level and its impact on the ventilation orifice
ΔQ^*	Normalized ΔQ
Δt	Time step
Δx	Mesh size
ΔY	Incremental rise
ϵ	Dissipation of turbulence energy
μ	Dynamic viscosity
μ_t	Turbulence dynamic viscosity
ν	Kinematic viscosity
ν_t	Turbulence kinematic viscosity
ρ	Density
ρ_w	Density of water
ρ_a	Density of air
$\sigma_.$	Constant value
ϕ	Sphericity of the particles making the porous media
ω	Specific dissipation rate

Chapter 1

Introduction

1.1 Background

Accurately describing and predicting multiphase flows is a task of great importance in various practical engineering applications, including various aspects related to stormwater management. One important objective of such research is to improve design practices by providing deeper insights into flow characteristics. In many instances that involve flows related to stormwater runoff, unsteadiness associated with complex geometries creates important challenges to engineers, difficulting the development of designs.

One key driver in this process is related to water quality impacts. The US Environmental Protection Agency (EPA) implements across the states the National Pollutant Discharge Elimination System (NPDES). The NPDES is created to prevent pollution caused by stormwater from various human activities, including the operation of urban drainage systems, construction activities, and industrial activities. Improper stormwater management can cause significant pollution because sediments, chemicals, sanitary wastes, garbage, and other pollutants are transported by runoff. NPDES program enforces goals in terms of water quality parameters to mitigate impacts of stormwater discharge to natural water bodies.

Often the design criteria of various hydraulics structures related to stormwater management rely on the results of empirical research. While positive, it is expected that there are opportunities to improve upon existing design recommendations with the aid of modeling approaches. When properly calibrated and adjusted, numerical models can be applied to describe unsteady flows in complex geometries. This work focuses on the application of computational fluid dynamics (CFD) models to represent conditions in unsteady, multiphase flows in various contexts of stormwater applications.

1.2 Motivation

As stated above, stormwater management is an integral component of various economic activities. Without proper stormwater management, pollutants from urban drainage systems, construction sites, mining operations, and farmland will be transported to natural water bodies. This, in turn, will cause deleterious impacts on human and natural ecosystems, which should be avoided.

The first application in this research involves the description of extreme flow conditions in sewerage systems. These systems may be either combined sanitary sewers (CSS) or separate sanitary sewers (SSS), depending on whether stormwater runoff flows in the same or in separate conduits as sanitary sewerage (EPA, 2004). Older urbanized areas often have CSS conduits, and these systems are particularly deleterious to the environment during intense rain events. In such conditions, these systems may experience combined sewer overflow (CSO) episodes, which create severe environmental impacts, and contribute toward 99% or more of volume of untreated wastewater discharge every year (EPA, 2004).

One approach to resolve this problem in highly developed areas is to construct large underground storage tunnels and reservoirs to temporarily store water and avoid overflows, stemming the peak flows and enabling treatment for runoff volumes. Figure 1.1 presents a sketch of the CSO deep storage tunnel in Indianapolis, IN. Unfortunately, such strategies cannot fully eliminate operational problems, such as pressure oscillations in shafts, referred to as surging. The filling process in these tunnels during intense rain events is very complex, and open channel flows coexist with pressurized single phase flow, pressurized two-phase flow, or their combinations. Particularly in complex geometries, one-dimensional models will not be able to represent the flowing reality in the system. This research aims to apply CFD models to describe selected flow conditions involving air-water interactions in stormwater systems.

Another context in which complex stormwater application modeling can be useful is in the applications involving sediment-water flows. Certain activities such as construction, farming, mining, and etc. can mobilize large amounts of sediment, magnifying in many orders of magnitude the natural processes of erosion (EPA, 2007). Sediment discharges to the environment,

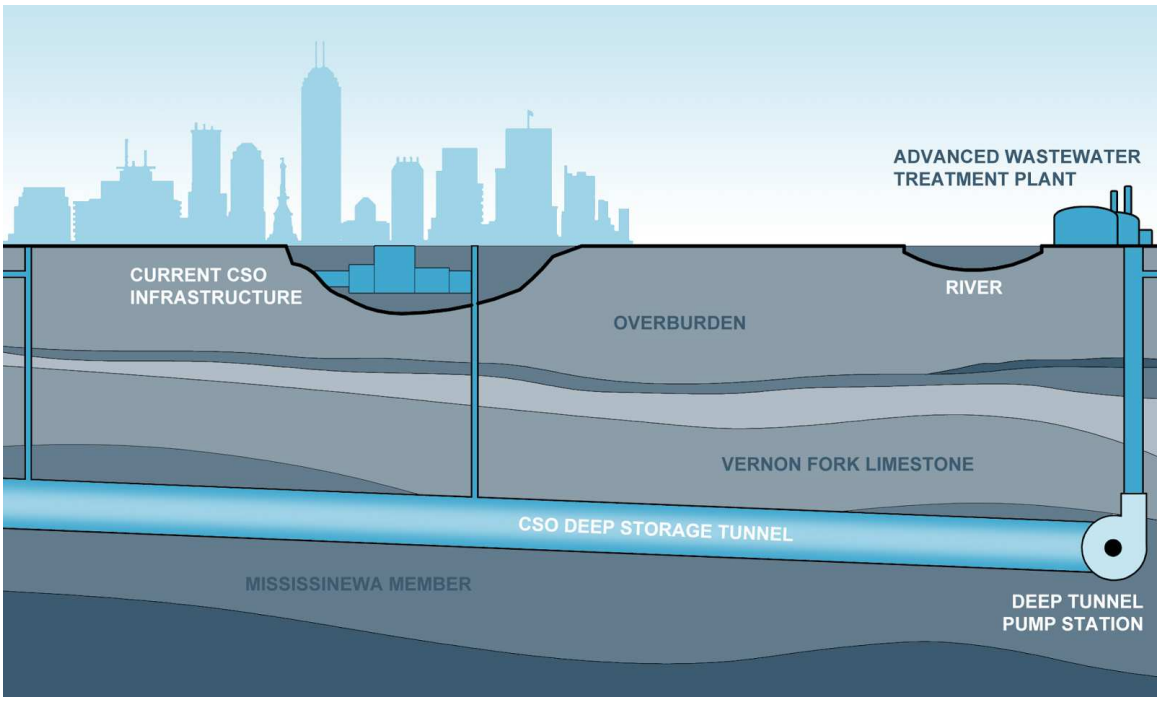

Figure 1.1: Sketch of under construction CSO deep storage tunnel in Indianapolis, IN (Overbey, 2014).

as is indicated in Figure 1.2, are an important cause of concern. Treatment for constituents presenting in the runoff can be implemented to reduce sediment pollution. Best Management Practises (BMP), such as sediment basins, are used as means to allow for water quality improvement (Alabama SWCC, 2014; CASQA, 2011; Clar et al. 2004; MDEQ, 2014). Sediment basins are structures used to control and minimize the discharge of mobilized sediments to the environment. These structures often have complex geometries and are subjected to unsteady rates of inflows. Various design aspects of such structures are based on empirical recommendations, which include length-to-width ratios, maximum depths, etc. However, it is anticipated that systematic numerical modeling of flow conditions in these basins can help corroborate or even improve these experimentally-based design guidelines. This is one of the goals of the present research.

There are also other applications in which sediment-water flows are cause of concern, such as farming and mining operations. While the rate of sediment erosion in farmland ranges from 5 to 10 percent of that on construction sites, which ranges 100 to 200 ton/acre/year, the total erosion amount is very large due to the significant amount of land use in the US dedicated to

Figure 1.2: Sediment pollution from a construction site (McLaughlin, 2015a).

farming. In the US, the total erosion from farmland is as much as 1.73 billion tons in 2007, and over 55 percent is caused by stormwater runoffs (NRCS, 2010). Mining sites, though not widely spread as farmland, can be significant pollution sources to nearby water bodies, as active surface mines can attribute the same quantities of soil erosion as a construction site per acre per year (EPA, 1976). Figure 1.3 shows a dam breach event at a mining site causing a large number of pollutants discharged to the nearby waterways. These applications, however, are not focused on the present research.

In summary, stormwater management is an important component to mitigate the environmental impacts of various human activities. It is assumed that a better and improved flow characterization can help on the design and operation of stormwater management facilities. An improved description of flows in complex geometries using numerical models that incorporate unsteadiness and multiphase flow conditions can help in stormwater management goals. Next section briefly presents a review of the current research progress in the areas focused in the present research.

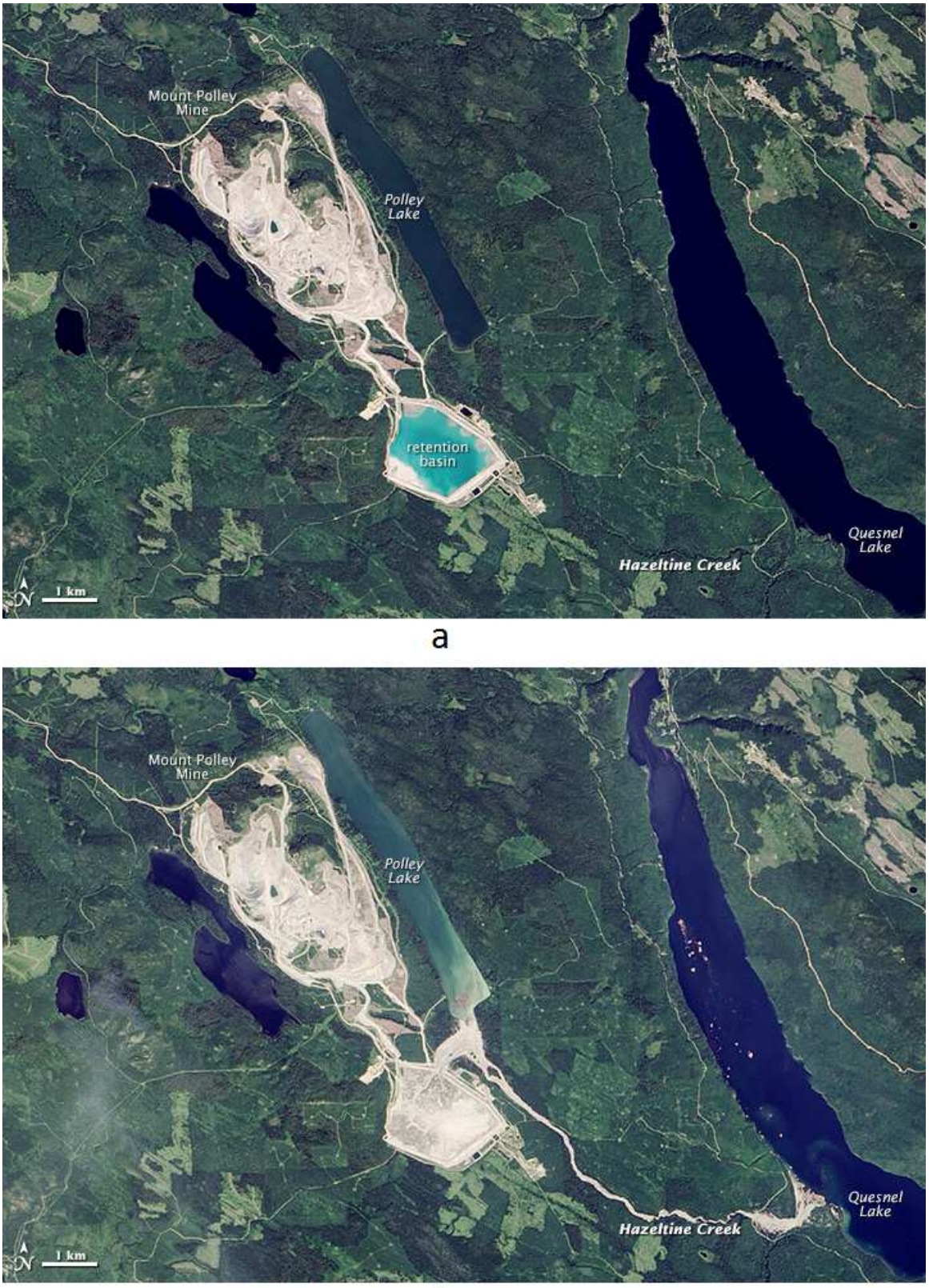

Figure 1.3: NASA aerial view of Mount Polley Mine site, British Columbia, CA, a) before the dam breach at August 4, 2014 and b) after the event (Allen and Voiland, 2017).

1.3 Brief review of current research

1.3.1 Extreme flows in urban drainage systems

Intense rain events trigger conditions that involve the rapid filling of sewers and tunnels in urban areas, which in turn lead to a host of operational problems. Some of these problems are worsened by the various processes in which large air pockets are entrapped in the filling process. The work by Li and McCorquodale (1999), Zhou et al. (2002), and Vasconcelos and Wright (2006) present various mechanisms by which air pocket may become entrapped in stormwater systems. Problems involving air-water interactions in closed conduit systems have been explored by Ramezani and Karney (2016), Vasconcelos and Wright (2016), among others. Excessive surging, vertical displacement of air in shafts, uncontrolled air release triggering geysering episodes, and the associated manhole cover displacement are the interesting topics being focused in this review.

Stormwater geysering is defined as a process that stormwater within underground tunnels returns to the grade through ventilation shafts, which can also lead to manhole cover displacement. It usually lasts for several seconds to minutes and can be very severe. Some typical stormwater geysering episodes are shown in Figure 1.4. A preliminary geysering research was presented by Guo and Song (1991), which assumed these events as caused by a single-phase inertial oscillations in shafts. The investigation by Wright et al. (2011) showed that geysering events could occur even when the piezometric head was much below grade elevation, which challenged the mechanism presented by Guo and Song. The experimental and numerical work by Vasconcelos and Wright (2011) demonstrated that uncontrolled release of large air pockets can create significant displacements of water in shafts, leading to geysering episodes. Such observations were confirmed by much larger scale laboratory tests presented by Muller and Vasconcelos (2016). More details on such experimental studies are presented in the next chapter.

Numerical modeling of these complex air-water interactions has been limited, with most of the effort focused on unsteady, one-dimensional modeling studies such as Martin (1976), Zhou et al. (2002), Vasconcelos et al. (2009), among others. However, complex geometric

Figure 1.4: Three stormwater geyser episodes in a) Saint Paul, MN, 1982, b) Minneapolis, MN, 1997, and c) Chicago, IL, 2010 (Vasconcelos et al. 2012).

characteristics of uncontrolled air pocket release from stormwater cannot be well described by one-dimensional modeling approaches. CFD models, on the other hand, can be applied to these problems, but there has been very limited research effort in this direction, as is further explored in the next chapter.

1.3.2 Sediment settling and resuspension

Research on settling and sediment basin initiated several decades ago. Processes of particle coagulation, flocculation and sedimentation have been defined and studied in the classical paper by Hazen (1904). In the context of the NPDES, EPA (1976) addressed sediment basins in coal mining operations as means to prevent uncontrolled sediment discharges off-site. Experimental research on sediment basins has been focused mostly on experimental evaluation of their performance, as exemplified by Griffin et al. (1985), Millen et al. (1997) and Thaxton et al. (2004). However, not many numerical investigations on the performance of basins were performed until much more recently. Even so, numerical studies such as the works by Naser et al. (2005), Torres et al. (2008) and Kouyi et al. (2010) focused on specific basin geometries, rather than a systematic evaluation of their performance in terms of general geometric characteristics.

Another instance of sediment-water flows is represented by sediment resuspension processes created by shear forces acting on settled particles. Resuspension processes have been studied in contexts that involve shallow lakes, bays, and ponds, and often triggered by wind and currents (Krone, 1979; Booth et al. 2000; Bentzen et al. 2009). Resuspension can occur in varying scales, from a small construction site up to continental shelf regions. For instance,

Figure 1.5 shows massive sediment resuspension event along the Florida coastline caused by a hurricane. Even while resuspension is a process that is easily noticeable in the context of erosion and sediment control on construction sites, to date this process has not been studied sufficiently in controlled laboratory conditions. Moreover, alternatives to mitigate the resuspension created by shear flows, particularly in sediment basins, have not been investigated.

1.4 Summary and structure

This research attempts to improve flow characterization on applications involving air-water flows in urban stormwater systems and sediment-water flows on sediment basins. Most of the work was centered around the application of CFD models to representing these flows, but also experimental results were collected in the context of sediment basins. This introductory chapter presented the background, motivation and a very brief literature review on the research focus of this research, which was the characterization of different types of unsteady and multiphase flows in the context of civil engineering. The structure of this document is presented below:

1. Chapter 2 presents in sequence a more complete literature review.

2. Chapter 3 illustrates an application of CFD using VOF method to represent free surface flows in a classical application of unsteady, two-phase flows, represented as the problem of dambreak.

3. Chapter 4 presents the research on stormwater geysering caused by the release of entrapped air pockets, aiming to develop and calibrate a CFD model that can replicate geysering episodes. The CFD model is then applied to larger-scale geometries to investigate the factors that affect the geyser intensity. A geometric retrofitting strategy is proposed to mitigate geyser at the end of this chapter.

4. Chapter 5 presents the likelihood of manhole cover displacement created by sudden pressurization of vertical shafts, triggered by either inertial surge or the release of entrapped air pockets.

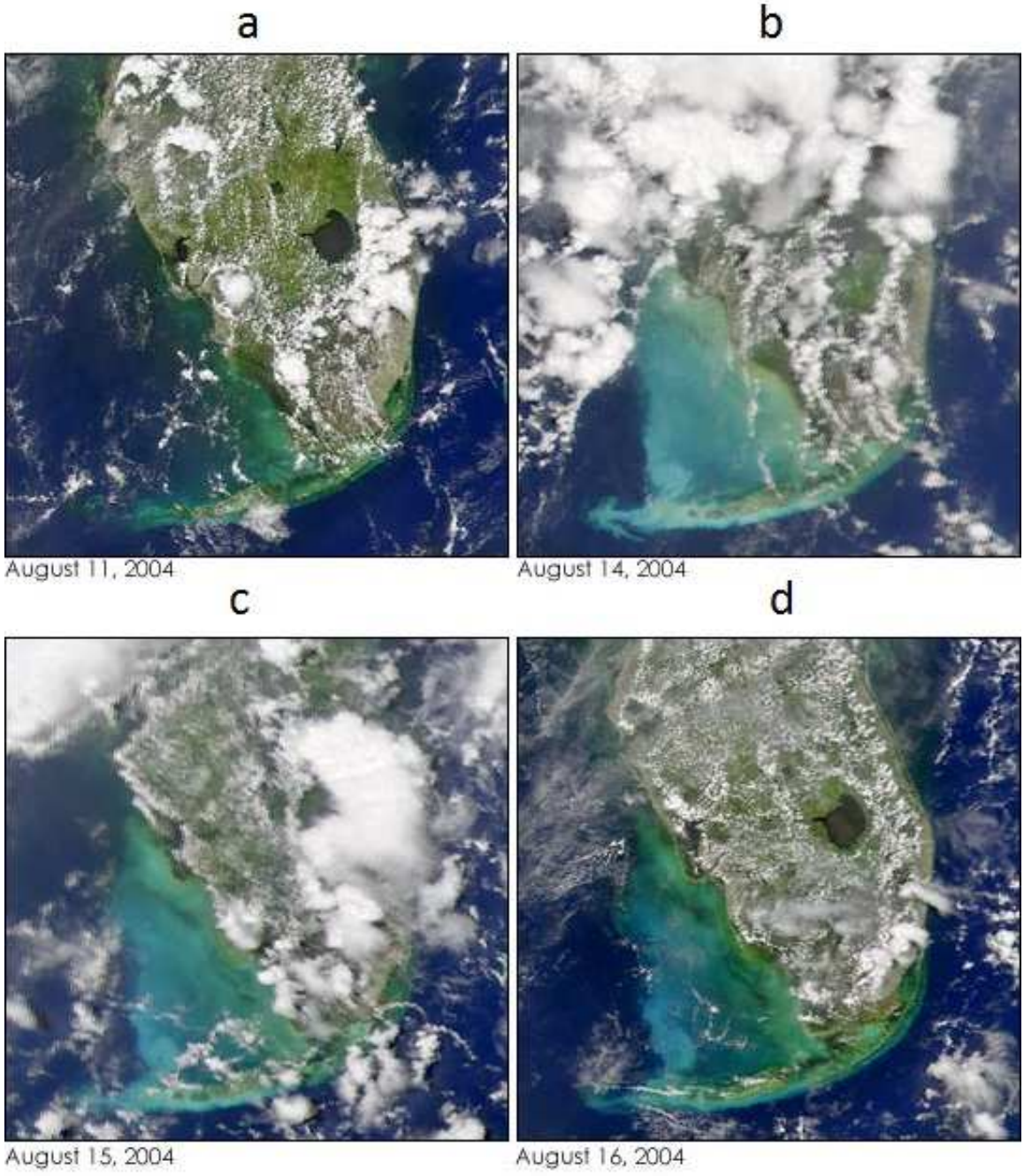

Figure 1.5: Sediment resuspension at southwest Florida caused by Hurricane Charley, August 13, 2004 (NASA, 2004).

5. Experimental and CFD study on filling and dewatering processes of sediment basins are focused on Chapter 6. Experimental work focuses on the characterization of water turbidity over different depths and water treatment with the flocculant, whereas the CFD study aims to create a model to study flow patterns within basins.

6. Chapter 7 presents a CFD research on the flow conditions that lead to soil particle resuspension, and how this can be mitigated with the use of cellular confinement systems.

7. Research conclusions are summarized in Chapter 8.

Chapter 2

Literature Review

In this chapter, the existing investigation on the selected research topics are reviewed and summarized in the following sequence 1) research on stormwater geyser in Section 2.1; 2) research on air pressurization in manholes and manhole cover displacement in Section 2.2; 3) investigation on flows in sediment basins in Section 2.3; and 4) research on sediment particle resuspension caused by shear forces in Section 2.4. At the end of this chapter, the current knowledge gaps of the research topics in this dissertation are introduced.

2.1 Stormwater geysering in urban drainage systems created by air pocket releases

Researchers have made important progress on the cause of geysering during the past three decades but mechanisms behind this phenomenon are still not fully understood. Guo and Song (1991) proposed that the geyser events in the Tunnel and Reservoir Plan (TARP) system in Chicago were related to the rapid filling process during intense rainfall events. Their research focus was on the water free surface fluctuation caused by tunnel surge that could finally lead to water discharge through the manhole. The possibilities of two-phase, air-water flow interactions were not considered.

Field research on geysering episodes in Minnesota was conducted by Wright et al. (2011). The authors found the mechanism presented by Guo and Song (1991) could not be consistent for some geysering events that were observed, which were characterized by large discharges of air. Piezometric pressure heads during the geysering episode were recorded and showed that pressure heads had not exceeded grade elevation. Wright et al. (2011) noticed that the recorded geyser episodes could be caused by the interaction of entrapped air pockets with the water initially standing in the shaft. The present research focuses on the releasing process of such entrapped air pockets.

The presence of large, entrapped air pockets in stormwater systems is attributed to large amounts of air is initially present in the systems prior to filling process when the flow realm in the tunnel is open channel flow. As water inflows continue, they gradually displace and force air discharge through ventilation shafts. According to the numerical simulation studies by Vasconcelos and Wright (2016), air pocket entrapment caused by the development of two pressurization interfaces in tunnels occurred in 163 out of 216 test cases, and 27% of the entrapped air pockets were categorized as large or very large pockets involving rapid filling conditions. When rapid inflows are observed, various air pocket formation mechanisms can also occur, as demonstrated in experiments by Li and McCorquodale (1999), Vasconcelos and Wright (2006), among others. Based on the experiments by Patrick and Vasconcelos (2015), air pocket formation can occur when inflow rates are gradual.

Once entrapped, air pockets move within tunnel systems as discrete gravity currents, as described by Baines (1991). The pocket celerity depends on various factors, such as air pocket volumes, the existence of background flows, opposition between buoyancy and drag forces, etc. Figure 2.1 shows a backward-moving air pocket motion in a horizontal slope pipe with background flows, which is affected by both background flows and shear stress (Chosie et al. 2014). However, when an air pocket of significant volume arrived at the base of a water-filled ventilation shaft, it was observed in experiments that these pockets will move vertically (Vasconcelos and Wright, 2011 and Lewis, 2011), as shown in Figure 2.2. This vertical air pocket motion created the displacement of water ahead of the pocket, which in turn could lead to discharges of a mix of air and water on the top of these shafts. This uncontrolled air pocket release phenomenon is referred to as stormwater geyser, often characterized by jets of air-water mix rising through manholes and other vertical structures. Geyser occurrence may create highly explosive discharges of poor quality conveyed runoff, which can be very damaging and result in a number of deleterious impacts.

The rise of gas pockets in vertical liquid columns has also been studied in other contexts to some extent, but not extensively in the context of unsteady stormwater flows. For instance, Batchelor (1967) presented a classical problem of the rise of a Taylor bubble (shown in Figure

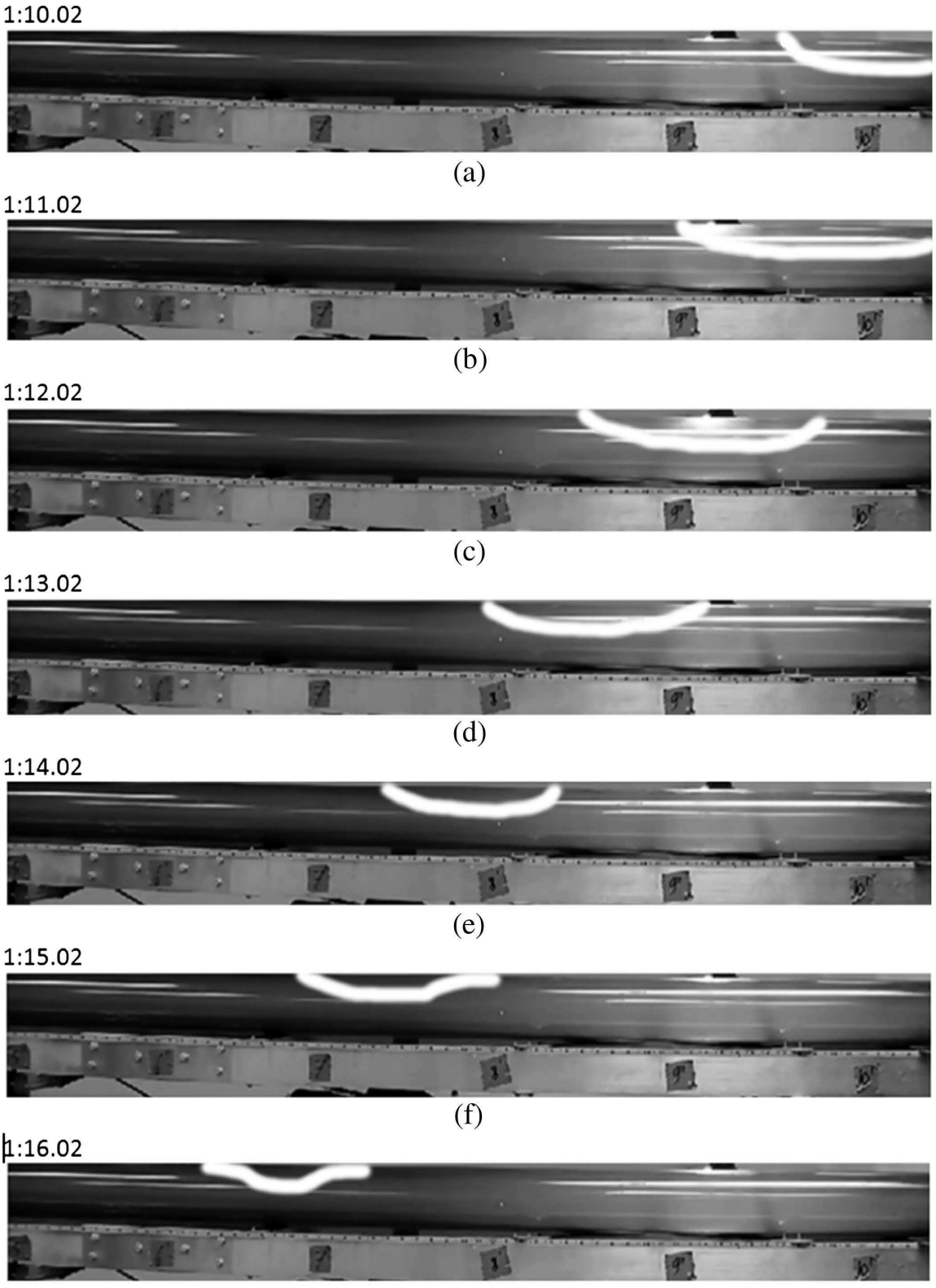

Figure 2.1: Sequence of snapshots of air pocket moving in a pipe (Chosie et al. 2014).

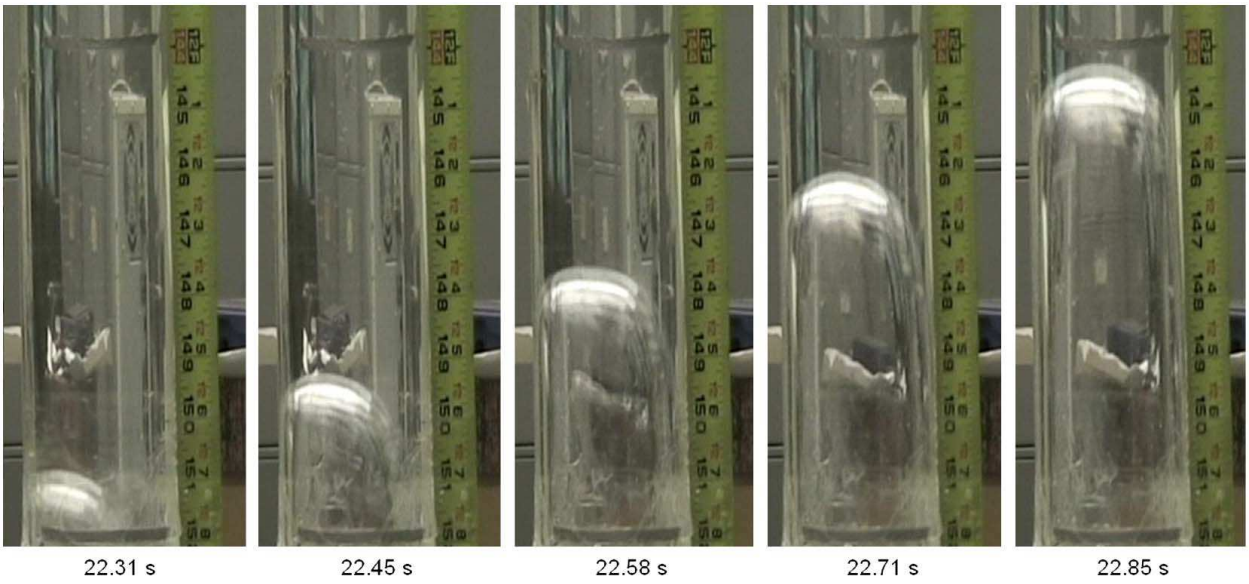

Figure 2.2: Rising motion of air pocket while horizontal motion of air pocket in pipeline is from left to right (Vasconcelos and Wright, 2011).

2.3). The experiments indicated that the rising velocity was close to $0.34\sqrt{gD}$, which is consistently smaller than the air pocket rising observations by Vasconcelos and Wright (2011) and Lewis and Wright (2012). The cause of this is unclear, but may be linked to unsteadiness of air pockets leaving horizontal pipes into vertical pipe, as well the process of air volume increase as it moves in the vertical shaft and decompresses.

Another interesting experimental study related to the release of air phases in vertical pipes was presented by Carvalho et al. (2000). The authors describe flood instability as a phenomenon created when liquid film flow moves downward in the vertical pipes, having its interface roughed by a central upward gas flow. As this counter current flow increases, the gas-liquid interface may show waves and liquid detaches from the downward flow and travels upward with the gas pocket. They consequently found that this caused a steep increase in the pressure gradient along the gas pocket. The authors proposed a scaling law relating the onset of flooding instability with the density of the gas phase rising in vertical tubes. It was shown that slugs of air with larger density rising in vertical pipes can have an earlier onset of flooding instabilities when compared to conditions where air is in atmospheric pressure. It is possible that the shearing process created by flooding instability could explain some of the spray characteristics of stormwater geyser releases, however this possibility has not explored yet.

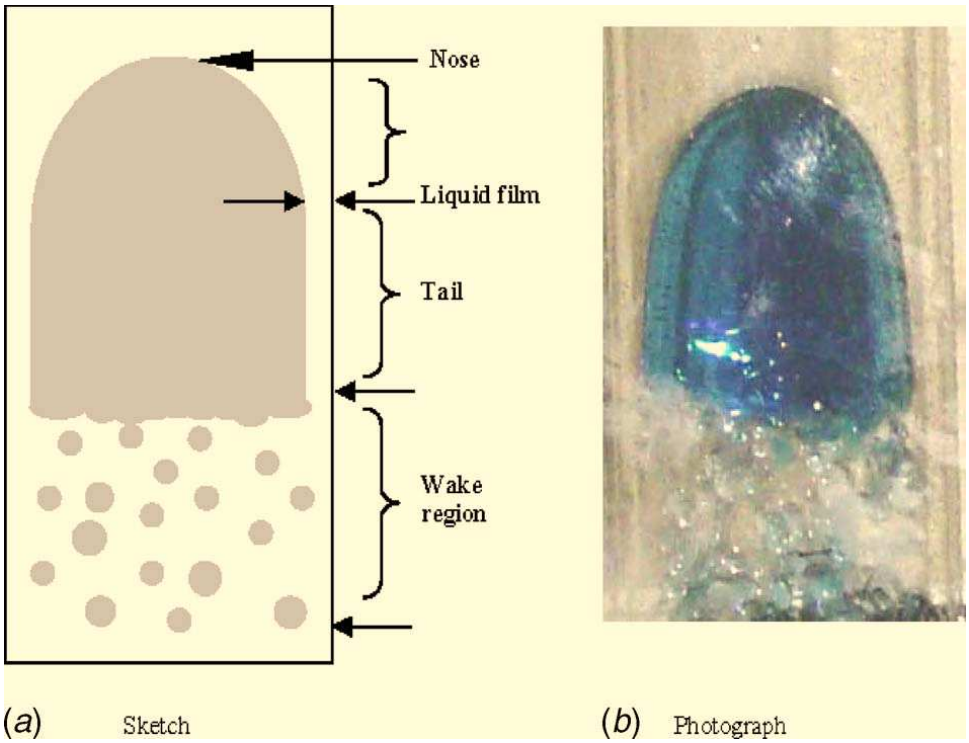

Figure 2.3: Sketch and photograph of Taylor bubble rising in water (Mandal et al. 2009).

So far, the most recent and comprehensive research on geysering events is from Vasconcelos and Wright (2011). The authors did a series of experiments to investigate the role of entrapped air in the tunnel when geyser occurred and studied the effects of selected parameters on the pressure, free surface and air water interface displacement. They observed the diameter of ventilation shaft was the critical variable that affected air pocket releasing process. Cong et al. (2017) also developed an experimental model showing that external pressure head and vertical shaft diameter were the key factors that determined the flow patterns and geyser intensity, which were further replicated by the CFD study of Chan et al. (2017). But further research on large-scale model is required since some of the details, like shear flow instabilities, were not addressed. Other relevant research like the work from Leon (2016) proposed a new mechanism that could cause geyser regarding to air pocket release, suggesting that the ex-solution of dissolved gases could be the cause of geysers in combined sewer systems.

There are not many numerical studies on geysering phenomenon to date. The first numerical work on geysering episode was possibly done by Guo and Song (1991), who attempted to describe the geysering with a single-phase discharge through the manhole. But as stated before,

single-phase model would not be able to explain all the geysering episodes. Thus alternative approach that considered the case of the water displacement caused by the rise of an air slug were proposed.

Early research regarding air-water flows on similar problem was conducted by Li and McCorquodale (1999) who applied rigid column method to track the trapped air pocket motion in pipelines. But air pocket movement in vertical shaft was not studied, during which process some essential feature like air expansion and water column rising would occur. A model based on lumped inertia analysis was then presented in Vasconcelos and Wright (2011) and further developed by Lewis and Wright (2012) for the case when the air release through vertical shaft occurred amid sustained water pressure in the system. The models were successful in representing the experimental conditions presented by the authors, but failed in attempting the describe the severity of geysering episodes observed in actual stormwater systems.

Shao (2013) developed a 2-D CFD model that used the Volume of Fluid (VOF) method to compute geysers. It was determined that small pockets did not create large water displacements, whereas larger air pockets created large water displacements and significant air phase flows upon pocket breakthrough. Although Shao's (2013) numerical model is a lot more complicated than the previous research, the lack of turbulence model and compressibility features are severe limitations. Another study that has implemented CFD on geysers was presented by Choi et al. (2014), who applied results by Vasconcelos and Wright (2011) to describe the characteristics of geysers created by the release of air pockets in laboratory conditions. The model applied a turbulence model and air phase compressibility into consideration and was able to qualitatively represent some of the measured flow features during the experimental geysering episodes. The CFD results of Shao and Yost (2018) indicated that with the aspect of driving forces, the large source, movement and/or the pressurization of the air pocket are the key factors affecting geyser. However, large-scale conditions of actual geysering events pose other modeling challenges (e.g. highly compressed air pocket) that have not been explored in either of these CFD investigations.

An interesting study by Catano-Lopera et al.(2014) involved the use of CFD models to simulate operational issues with the TARP system in Chicago. However, there was not an

attempt in that work to systematically evaluate flow conditions related to uncontrolled air releases for different geometry parameters, varying initial water levels, and different entrapped air pocket volumes. Thus this study is not of much usefulness to designers interested in mitigating effects of geysers in other urban drainage systems.

There have been almost no investigation on alternatives to mitigate geysering events. The existing research indicated larger dimension of vertical shafts was beneficial on reducing geyser intensity. However, the adoption of large-dimension shafts at all junctions may not be feasible in many cases. Construction of large-dimension shafts or retrofitting of existing small-dimension shafts to prevent geysering can have prohibitive costs.

In summary, geysering is a relevant operational issue that may impact the operation of stormwater systems, but is still not well understood. Experiments have been performed to evaluate these conditions and some of these investigations have provided relevant insights on this issue. There are difficulties in scaling these experiments considering both air and water phases while numerical method would be an alternative approach that could enlarge the model scale to replicate real world geysering episodes. In addition, numerical models can offer flow details at any location and time, with relatively less costs that is comparable to a study performed in reduced scale models. A robust and calibrated CFD model that is able to describe geysering episodes in a variety of large-scale geometries is still not available. The ultimate objective of the present investigation is to provide guidelines for mitigating and further eliminating geyser, so alternatives that can reduce geyser intensity are still warranted.

2.2 Manhole cover displacement created by sudden pressurization of vertical shafts

Manholes and shafts are integral components of stormwater infrastructure in urban areas, and allow for inspection of the system and inflows into sewers and tunnels. Manhole covers prevent people, animals, and objects from falling into the below-grade conduits. However, manhole cover displacement is a possible accident hazard to the public, particularly for pedestrian and vehicular traffic, as reported by Metcalfe (2012), Fourie (2015) (see Figure 2.4), and Crimaldi and Ramos (2016). Manhole cover displacement can have various causes. Regarding to rapid filling of stormwater systems, the inertial surge and air pocket entrapment/release in vertical

Figure 2.4: Example of a displaced manhole cover causing a traffic accident (Fourie, 2015).

shaft/manhole are two of the causes that can possibly displace a manhole cover via either pressurized air at manhole headspace or direct water impact.

In 1982, a manhole cover displacement event accompanied with geysering was recorded at St. Paul, MN (Guo and Song, 1991). It is one of the many recorded manhole cover displacement events that were caused by the return of water to the grade level. In recent, Lo (2018) recorded the moment when manhole cover was displaced by water impact. As introduced in previous section, relevant research, like Catano-Lopera et al. (2014), only focused on geyser but not on the dynamics of manhole covers, though it can be speculated that geyser discharges cause manhole cover displacements. Meanwhile, some reports (Holmes,2017; Foxnews, 2016) have also shown that the manhole cover were dislodged without necessarily reports of geysers, hence without direct impact of water phase in the cover. This may indicate that simple air pressurization in vertical structures can cause manhole cover displacement.

The pressure surge study undergoing rapid filling by Martin (1976) is instructive to the present research, which indicated that the air at the end of a closed conduit could be strongly

pressurized under limited ventilated conditions. If it was applied to stormwater system, such air pressure may be sufficient to overcome the weight of a manhole cover. A follow-up investigation by Zhou et al. (2002) observed three types of air pressurization patterns, including:

- Type 1: a relatively small pressure surge attributed to air cushion effects associated with small ventilated condition;
- Type 2: a severe water hammer pressure spike when air cushion effects are vanished associated with large ventilation; and
- Type 3: Type 1 pressure surge followed by Type 2 at the point when most air is released observed intermediate ventilated condition.

On a subsequent study, Zhou et al. (2004) got similar findings by implementing both experimental and numerical investigation under the situation of an air pocket located at the headspace of a vertical pipe end, which is similar to the present investigation.

A 2D and a 3D VOF method based CFD models were developed by Zhou et al. (2011), demonstrating that CFD models could also describe the flow physics and pressure oscillations. A separate investigation by Zhou et al. (2013) indicated that the pressure surge magnitude could be much higher when multiple air pockets exist in the pipeline. Yet, the pipe end of the models was fully sealed, resulting in Type 1 pressure surge only. A limitation of the model used by Zhou et al. (2013) is that the scale and the filling process of the model were not similar as a real manhole so that it was not capable to estimate the possibility of manhole cover displacement based on the results.

Aside from the headspace air pressurization caused by inertial surge in vertical shaft, the release of entrapped air pocket can also lead to rapid rising of free surface as introduced in previous section, which will consequently result in air pressurization for limited ventilated conditions. This is very relevant to geyser events, while the existing geyser research didn't consider the limitation of ventilation size.

In summary, manhole cover displacement undergoing rapid filling is very relevant to inertial surge and air pocket release problems in stormwater system. Relevant research on such

topic have not considered the likelihood of manhole cover displacement when the manhole has limited ventilation. As a result, the flow patterns and characteristics within manhole headspace are barely understood.

2.3 Sediment-water flows in basins

The NPDES program limits the water quality impacts in natural waterways created by various point sources of pollution, which include construction sites. Various techniques have been used in the context of erosion in sediment control on construction sites to minimize environmental impacts, as was illustrated in Alabama Soil & Water Conservation Committee (SWCC) (2014). However, the present focus of this research is to study flow characteristics of one of the sediment control approach, namely sediment basins. This section presents a summary of the research on the characteristics and performance of sediment basins.

One relevant experimental investigation was presented by Griffin et al. (1985) used Rhodamine WT dye as the tracer to study the dead storage of a basin and noticed that it depended heavily on the length-width ratio. Length-width ratio of 2:1 was suggested for the breakpoint between long and short basins. Long basins were concluded to have smaller dead zones. Millen et al. (1997) also performed experiments to evaluate the performance on reducing the mass of sediment discharge of different dewatering systems of basins. Through this study it was shown that skimmers (presented in Figure 2.5) were more efficient than traditional perforated risers, which were more commonly used back then. It also showed that in-basin barriers improved the performance of basin with perforated risers, but not with skimmers.

Research performed by Thaxton et al.(2004) assessed various baffles in sediment basins and concluded jute/coir baffles (shown in Figure 2.6) out-performed other baffle alternatives in reducing the mean flow velocity magnitude and transverse velocity variance magnitude. For example, the quickest patch velocity with the treatment of jute/coir baffles was about half of that when silt fence baffles were used in the research. The authors also found finer particles could be better captured by basin with jute/coir baffles, and that baffle alternatives based on silt fence fabric produced localized jet flows that could worsen sediment resuspension. McCaleb

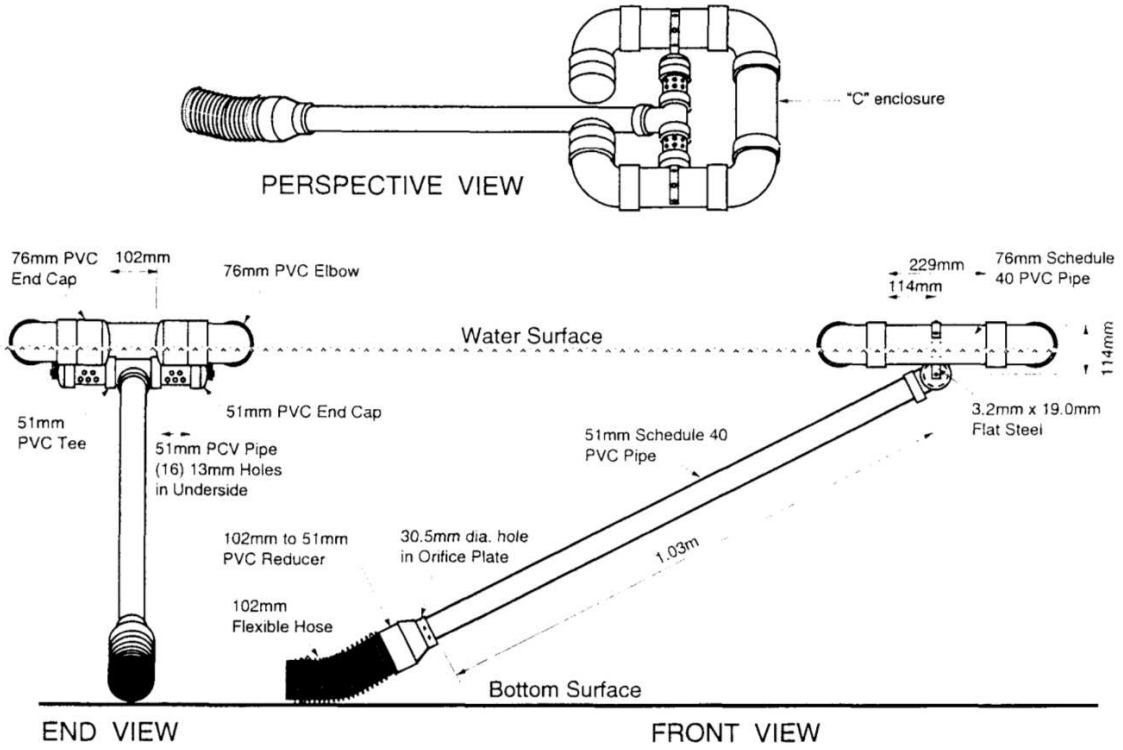

Figure 2.5: Engineering drawing of skimmer (Millen et al. 1997).

and McLaughlin (2008) systematically studied the effectiveness of five different sediment detention devices, including basins with rock outlets, basins with standing pools, and basins with skimmers. Their results indicated basins with rock outlets were relatively ineffective in retaining sediments. The basins with standing pool had greater sediment retention efficiency, and the basin with skimmer presented a retention up to 99% of sediments in certain flow conditions.

By comparison with experimental studies, the application of CFD models on sediment basin studies is much more recent. One early work was presented by Naser et al. (2005), who developed a 2D numerical model to simulate sediments removal in a rectangular sediment basin. The model successfully predicted the velocity distribution and the concentration of the suspended load. Yet, 2D models of basins are too simple to replicate the flow pattern and performances in actual sediment basins. Another 2D simulation study was presented by Lee et al. (2008), who simulated settling with flocculation in a sediment basin with FLOW-3D.

Torres et al. (2008) did both 2D and 3D CFD simulation of a large stormwater detention and settling basin. The 2D model simulated both the hydrodynamic behavior and the solid transport in basins while the 3D model predicted location of settling zones by means of

Figure 2.6: Jute/coir baffles in a basin (McLaughlin, 2015b).

Reynolds and shear stress modeling. Good correlation of settling zones between the 2D and 3D simulation predictions and field observation was obtained as shown in Figure 2.7. Kouyi et al. (2010) conducted a 3D CFD simulation of the same basin, and tried to obtain thresholds of the turbulent kinetic energy (TKE) near the bed to improve the modeling of the settling processes. Tsavdaris (2015) conducted a series of CFD simulation of various configurations of detention pond, including vegetation, a subsurface central berm, and an emergent central island. The results suggested an elliptic pond with either a subsurface central berm or an emergent central island performed best with respect to flooding risk management and gravity sedimentation potential. Yet, one limitation of these studies toward the research goals is that the size and characteristics of stormwater detention basins are not similar to construction site basins.

Another CFD work from Dufresne et al. (2009) applied Eulerian-Lagrangian approach to track sediment particles in a laboratory rectangular sediment tank. The modeled flow pattern and deposition location achieved good agreement with experimental data (shown in Figure 2.8), which showed the potential of Lagrangian methods on sediment basin flow simulation. Yet, the challenges of a performing CFD simulations in large-scale applications, involving large mesh numbers were not explored in that study.

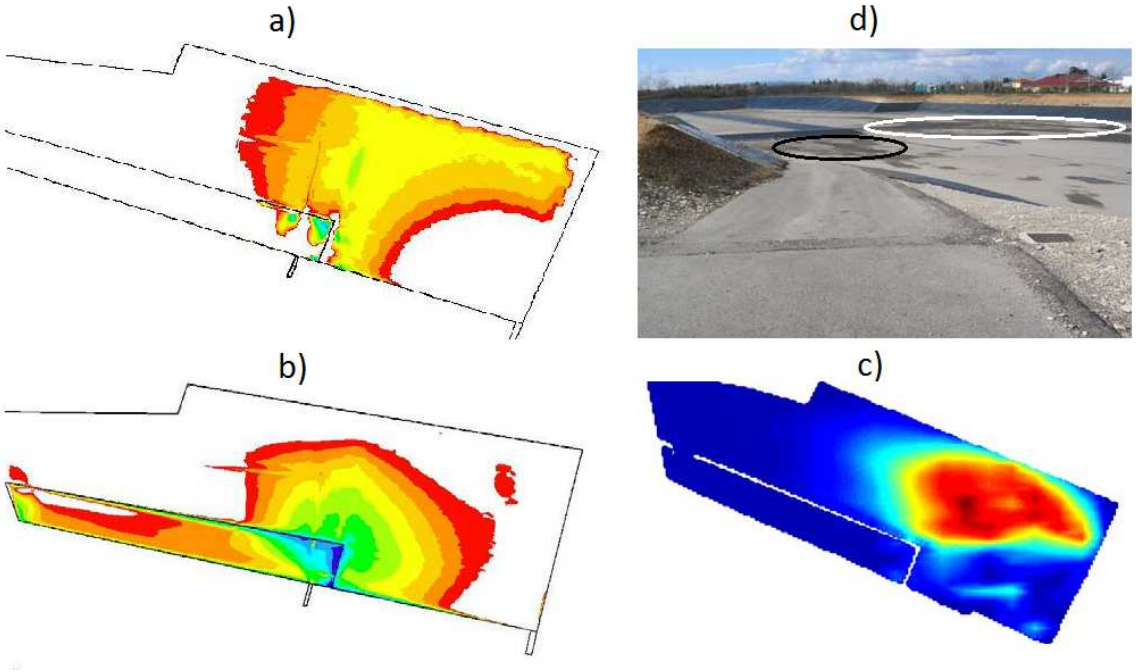

Figure 2.7: CFD estimation and observed sediment distribution at the basin bottom: a) contour of skin friction coefficient ; b) contour of Ox Reynolds stress; c) results arose from Rubar20 software; and d) real observed sedimentation zones (Torres et al. 2008).

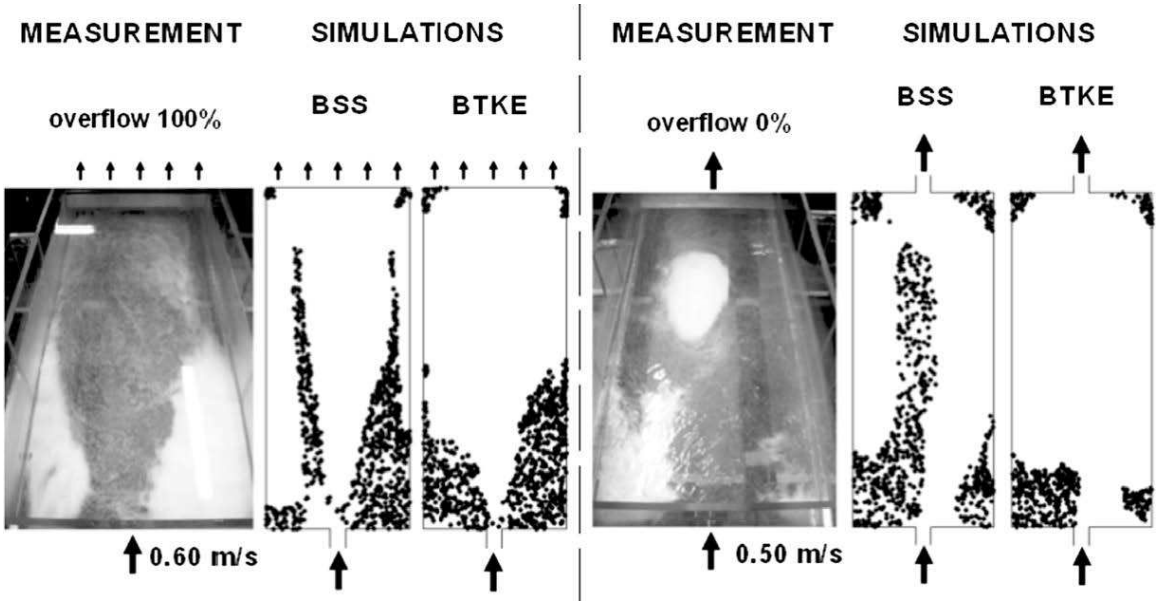

Figure 2.8: CFD estimation by Eulerian-Lagrangian approach and observed sediment distribution at detention tank (Dufresne et al. 2009).

In summary, the efficiency of sediment basins have been investigated to this date mostly through experimental studies. Key design parameters that have been considered to this date include length-width ratio, features present within the basins such as baffles and skimmers, effects of different outlet types, among others. Related numerical simulations work using CFD have been more limited, and a systematic evaluation of flows in these basins is still missing.

2.4 Resuspension of soil particles

As stated above, several strategies and practices have been used in sediment basins to improve the basin performance. Resuspension of settled sediment in basins, however, has not been considered in experimental or numerical studies to date. The process of sediment resuspension has some similarities with the classical problem of incipient motion in sediment transport (Yang , 1996). Resuspension occurs when shear force created by flow achieves a critical value that is able to mobilize soil particles. In some conditions, settling is recent and inter-granular bonds in submerged fine particles should be weak (FEMA, 2009).

Resuspension processes in the context of sediment basins have not received much attention to date. Related research focuses flow waves inducing resuspension in water bodies. Wind and currents are found to be key agents of resuspension of fine sediment in shallow water bodies. Large waves are able to suspend and transport significant quantities of sediment (Krone, 1979, Booth et al. 2000, and Bentzen et al. 2009). For example, the waves induced by winds of $4m/s$ resuspended approximately 50% of bottom sediments in Lake Salvador, Little Lake, and the lower Barataria Basin (Booth et al. 2000). Thus, it is also possible that the efficiency of sediment basins can be affected by turbulence induced by a variety of sources leading to currents that can mobilize settled particles.

One related experimental and numerical investigation was presented by He and Marsalek (2014). The authors developed a bottom grid structure (BGS) (shown in Figure 2.9), which was a rectangular grid of obstacles placed in the bottom of a settling unit, as means to improve settling efficiency. In an experimental apparatus the authors studied the settling of crushed shell particles ($\rho = 1.35g/cm^3$, sizes from $60-225\mu m$). The authors observed approximately a 74% particle removal rate when the particles were allowed to settle into such structures. During tests,

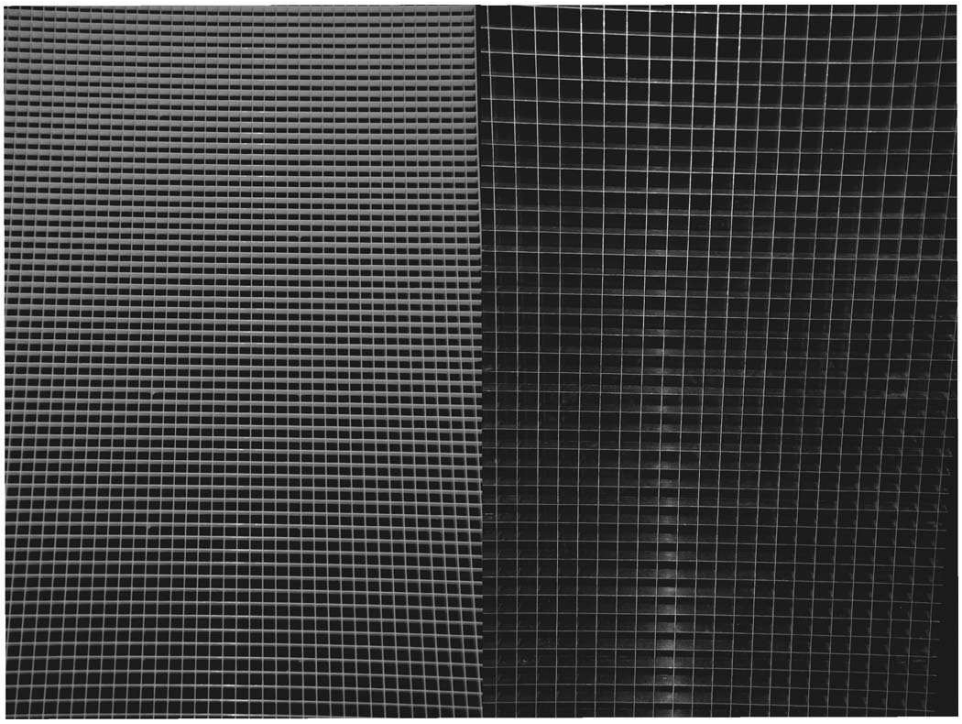

Figure 2.9: Photo of BGS developed by He and Marsalek (2014).

up to 79% of particles were removed with the most protective BGS alternative in place, which is considered as a significant improvement on the basin settling performance.

However relevant, He and Marsalek (2014) study focused more on mechanisms of particle settling instead of particle resuspension. Also, the characteristics of the particles used in the test were not consistent with soil characteristics, which are by comparison much denser and present a much wider range of particle sizes. BGS shape have similarities to cellular confinement system/cells (CCS), presented in Figure 2.10. CCS were developed by the US Army Corps of Engineering as an alternative for soil stabilization, soil improvement for vehicle traffic, channel protection, among others. However, the typical application of confinement cells involves filling the cells with rock, gravel or concrete. CCS were not considered in the context of preventing sediment resuspension.

CFD tools have been applied to study sediment-water flow interactions in a variety of conditions related to incipient motion and resuspension. Examples include Fernandez and Nirschl (2013), who studied particle motions in a cylindrical centrifuge with Eulerian-Lagrangian approach, resolving the flow field and particle motion by coupling CFD with Discrete/Distinct

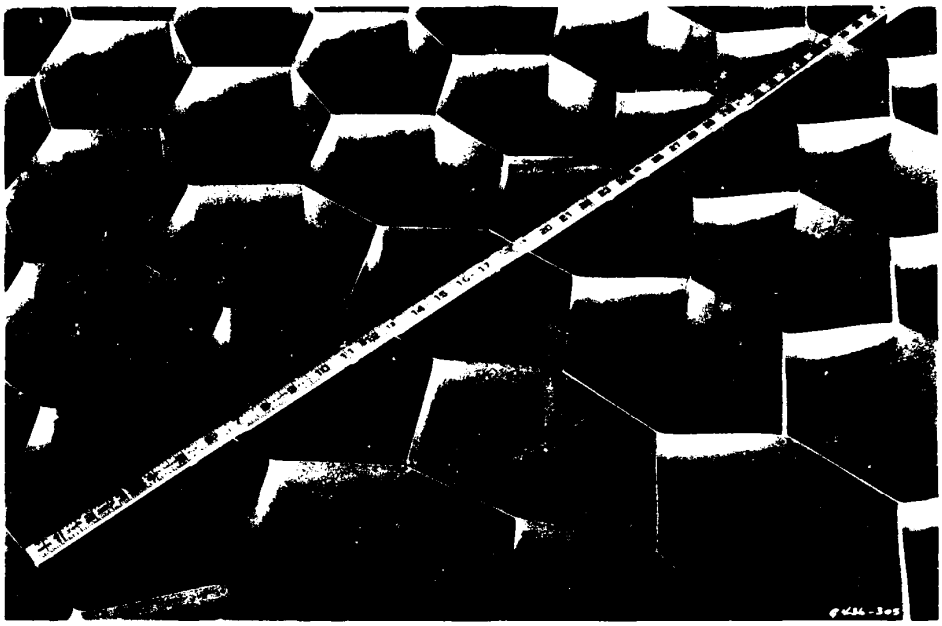

Figure 2.10: Photo of CCS for beach stabilization (Webster, 1981).

Element Method (DEM) (Cundall and Strack,1979). The advantage of the CFD-DEM model is that it takes the particle effects on the fluid phase and particle interactions into account. A simpler way is to simulate the flow field by neglecting particle effect, but using sediment transport model to resolve sediments.

Festa and Hansen (1976,1978) performed a 2D study with Boussinesq approximations to solve the estuary flow pattern and then applied this flow pattern to a suspended sediment model to simulate turbidity. Wu et al. (2000) resolved flow field by solving Reynolds Averaged Navier-Stokes (RANS) equations, and applied the simulated flow field to the suspended-load transport equation and the bed-load transport equation, and then calculated the bed deformation. An adaptive curvilinear grid was used to adjust the changing bed boundary, and effects of boundary changes were observed in water, however particle interactions were still neglected. Another alternative for sediment-water research using CFD focuses on calculating the flow field as a means to obtain insights on the observed sediment motion characteristics. This was the approach used by He and Marsalek (2014) and is also used in the present research.

2.5 Summary and knowledge gaps

Stormwater flows occur in a wide range of conditions and often involve very complex geometries. In many conditions stormwater flows are characterized by unsteadiness and multiphase conditions. This literature review on areas involving air-water interactions in stormwater drainage systems and on sediment-water flows in sediment basins point to the following knowledge gaps:

1. Rapid filling of urban drainage systems may lead to pressurized multiphase flow conditions. Among adverse operational conditions associated with such flows, geysers are one of the most severe and damaging phenomenon. Not much is known about air-triggered geysering, such as estimated pressure variations, kinematics of air pocket release and water ejection, etc.

2. Different numerical models of geysering events have been developed to date with specific objectives. However, available research has not applied CFD tools to assess the impacts of geometry characteristics (e.g. shaft diameters, lengths, air pocket sizes) to the magnitude of water displacement generated by air pocket releases.

3. Manhole cover displacement is another operational issue of stormwater systems undergoing rapid filling. It is likely that such events are caused by different mechanisms, i.e. inertial surge and air pocket release, which have received limited attention to date.

4. The performance of sediment basins have been evaluated by various experimental investigations to date, and much progress on understanding the performance of these basins have been obtained in the context of sediment control. However, detailed flow characterization is still not available. Such information would help improve understanding why certain geometry characteristics are better at retaining sediments, and possibly lead to design improvements.

5. Numerical studies on flow characterization of sediment basins have been limited, and in some other cases CFD research on settling structures are not representative of conditions

that would be anticipated in sediment basins. Similar observations can also be drawn with respect to the description of soil resuspension in sediment basins.

In Chapter 3, it is evaluated the applicability and accuracy of CFD models and VOF method in applications associated to unsteady and two-phase flows. One classical hydraulic problem that enables this assessment is the modeling of dambreak events. It is the foundation for the CFD models in the following chapters.

Chapter 3

Understanding of CFD Approach with VOF Method

3.1 Research objectives

CFD approach gradually becomes an important tool in solving hydraulic problems, particularly in the topics associated with interface tracking. The present research aims to apply VOF method and CFD models to solve relevant problems. Dambreak flows, a traditional two-phase flow with numerous analytical, experimental and numerical solutions, was selected as the model to assess the applicability of CFD and VOF method in civil engineering hydraulic application. Solutions of 1D dambreak flows yielded by different 1D and 2D numerical methods were compared with either experimental or analytical solutions. The selected modeling alternatives involve the following: Finite-volume solution using 2^{nd} order linear Lax-Wendroff scheme, 1^{st} order nonlinear Roe and HLL schemes, and a CFD modeling the NavierStokes equations (NSE) using OpenFOAM package, with interFOAM solver and standard $k-\epsilon$ turbulent model.

Numerical solutions compared with experimental results by Stansby et al. (1998) are presented first. The flow features at the initial stages of dambreak were focused on this comparison. Three upstream/downstream depth ratios and dry bed downstream cases were simulated and analyzed. The computing effectiveness of different mesh resolutions with $\frac{dx}{y_0} = 0.02, 0.10,$ and 0.20 were assessed as well, in which dx is the mesh size and y_0 refers to the initial upstream water depth. Other comparisons involve the use of analytical solutions for dambreak flows using either dry or wet bed conditions, but always neglecting bed friction. The final aim of this chapter is to evaluate the CFD modeling of two-phase flows using VOF method, which is further utilized in the following chapters to investigate the unsteady, multiphase flows.

3.2 Methodology

3.2.1 Analytical solution of dambreak flows in frictionless bed

The analytical solution derived by Ritter (1892) and Stocker (1948) is based on solving the primitive form of St. Venant Equation:

$$\begin{aligned} \frac{\partial y}{\partial t} + V_x \frac{\partial y}{\partial x} + \frac{A_f}{B} \frac{\partial V_x}{\partial x} = 0 \\ \frac{\partial V_x}{\partial t} + V_x \frac{\partial V_x}{\partial x} + g \frac{\partial y}{\partial x} = g(S_0 - S_f) \end{aligned} \tag{3.1}$$

where V_x is the flow velocity at location of x with the depth of y, g is gravity acceleration, A_f is the cross sectional area of the flow, B is the top width of the flow, and S_0 and S_f are the channel slope and friction slope, respectively. The C1 characteristic equation presented below is obtained from the integration of the Eqn. 3.1 expressed in characteristic format:

$$\begin{aligned} V_x - 2c = V_0 - 2C_0 \\ \frac{dx}{dt} = V_x + c = V_0 - 2C_0 + 3c \end{aligned} \tag{3.2}$$

in which V_0 and c_0 are the initial conditions of flow velocity and wave celerity, respectively, and V and c are the velocity and wave celerity at location of x at time t. For dry bed dambreak flows, the wave profile can be determined by:

$$\frac{x}{t} = 3c - 2c_0 \tag{3.3}$$

3.2.2 Numerical approach by solving St. Venant equation

The numerical method of solving 1D St. Venant equation adopted in this work is based on conservative form of St. Venant Equation:

$$\frac{\partial \vec{U}}{\partial x} + \frac{\partial F(\vec{U})}{\partial x} = S(\vec{U}) \tag{3.4}$$

where $\vec{U} = \begin{pmatrix} A \\ B \end{pmatrix}$, $F(\vec{U}) = \begin{pmatrix} Q \\ \frac{Q^2}{A_x} + \frac{gA_x^2}{2} \end{pmatrix}$, and $S(\vec{U}) = \begin{pmatrix} 0 \\ gA_x(S_0 - S_f) \end{pmatrix}$ where Q is the flow rate. The finite-volume solution of St. Venant Equation can be expressed as:

$$\vec{U}_i^{n+1} = \vec{U}_i^n + \frac{\Delta t}{\Delta x}(F(\vec{U})_{i-1/2}^{(n+1/2)} - F(\vec{U})_{i+1/2}^{(n+1/2)})) + \Delta t S_i^n \tag{3.5}$$

which could be applied to both linear and nonlinear schemes. The mesh size in the numerical approach by solving St. Venant Equation is based on high resolution discretization $\frac{dx}{y_0} = 0.02$, where y_0 corresponds to the initial water depth upstream from the dam prior to the flow initiation.

3.2.3 CFD approach with VOF method

The CFD approach in the present work is implemented with an open source C++ CFD application package, OpenFOAM (OpenFOAM Foundation, 2016). This tool was first developed by Weller (1998) as a field operation and manipulation (FOAM) library to create applications for CFD. The flow solvers in OpenFOAM can be applied to both single phase and multiphase flows with either laminar or turbulent NSE. The standard incompressible two-phase solver, interFOAM, is one alternative that solves RANS equations, applying the VOF phase-fraction based method (Hirt and Nichols, 1981) to track air-water interfaces. The governing equation representing mass and momentum conservations can be expressed as:

$$\rho \nabla \cdot (\vec{U}) = 0 \tag{3.6}$$

$$\rho \frac{\partial(\vec{U})}{\partial t} + \rho \nabla \cdot (\vec{U}\vec{U}) = -\nabla p + \nabla \cdot (\mu \nabla \vec{U}) + S_{\vec{U}} \tag{3.7}$$

respectively, where ρ is the average density of the fluid within a cell, t is time, $\vec{U}$ is the flow velocity vector, p is pressure, μ is dynamic viscosity, and $S_{\vec{U}}$ is momentum source term. The average density is defined as:

$$\rho = \alpha \rho_w + (1 - \alpha)\rho_a \tag{3.8}$$

with α is the fraction of water in the cell (between 1 and 0), ρ_w is the density of water and ρ_a is the density of air. Other parameters, such as viscosity, are also calculated based on the volume fractions of the two phases.

The standard $k-\epsilon$ model was utilized to resolve turbulence (Launder and Spalding, 1974). The turbulence kinetic energy k and turbulence dissipation ϵ are solved by (Matsubara et al, 2013):

$$\frac{\partial(\rho k)}{\partial t} + \nabla \cdot (\rho \vec{U} k) = \nabla \cdot \Big((\mu + \frac{\mu_t}{\sigma_k}) + \nabla k \Big) + P_k + P_{kb}\epsilon - \rho\epsilon \tag{3.9}$$

$$\frac{\partial(\rho \epsilon)}{\partial t} + \nabla \cdot (\rho \vec{U} \epsilon) = \nabla \cdot \Big((\mu + \frac{\mu_t}{\sigma_\epsilon}) + \nabla \epsilon \Big) + \frac{\epsilon}{k} \Big(C_{\epsilon 1}(P_k + P_{\epsilon b}) - C_{\epsilon 2}\rho\epsilon \Big) \tag{3.10}$$

respectively, where P_{kb} and $P_{\epsilon b}$ represent the influence of buoyancy forces, P_k is the turbulence production due to viscous forces, μ and μ_t are dynamic viscosity and turbulent dynamics viscosity, respectively, C and σ are constants. The mesh was generated with blockMesh utility in OpenFOAM, which is able to create parametric meshes with grading and curved edges (OpenFOAM Foundation, 2016).

The free surface profiles from the CFD solution in this work were obtained assuming a 50% volume of water threshold. The wave propagations were selected using the pressure threshold of 1%, 5%, and 10% of variations from the initial pressure of the bottom cell, $p_{up,0} - p_{down,0}$. For brief, 1%, 5%, and 10% threshold referred to the different variations from the initial pressure. Except where indicated, all the simulation results used in this paper were based on intermediate mesh resolution, which had square cells with size equal to $0.10y_0$.

3.3 Results and Discussions

3.3.1 Experimental comparison

In this subsection, experimental results (Stansby et al. 1998) are compared with analytical solutions, as well as CFD solutions. The length dimension was normalized by dividing by y_0, and the time dimension was normalized by dividing it by $\sqrt{y_0/g}$. From the dry bed downstream condition surface profiles shown in Figure 3.1 (a), the comparison indicated that analytical solutions underestimated the rarefaction wave speed and the CFD solutions could predict well

the rarefaction wave front propagation. Not the same accuracy was obtained with the analytical solution. At the initial stage (e.g. $t^* = 1.2$) the CFD solution underestimated the water depth right at the upstream side of the dam site, but as time went by it presented better agreement. Regarding the shockwave, the analytical solutions overestimated the shockwave propagation and the CFD solutions matched well the experimental data at $t^* = 1.2$ and 2.0 but overestimated the wave propagation at $t^* = 3.6$ and 5.0. This could be caused by flume bed that, albeit smooth, was not frictionless and decelerated the inflow front. The difference between model results and experimental thus became larger with time for the dry bed condition. Figure 3.1 (b) presented the surface profiles of a wet bed with initial condition of $10\%y_0$ of upstream water depth. Similar conclusion can be drawn about the rarefaction wave with that of dry bed case but the shockwave comparison tended to be complex. The analytical solutions of the wave front position almost agreed with the experimental data at $t^* = 1.2$, 6.5, and 8.9 but underestimated the wave front position at $t^* = 4.0$. Thus, it was not concluded that the analytical solutions predict well the shockwave propagation for wet bed downstream of a dambreak problem. The CFD solutions could qualitatively present the oscillation of the wave but tend to overestimate the wave front positions.

3.3.2 Onset of 1D flows

The analytical method and St. Venant solutions were based on 1D flow assumption and the CFD simulation in this research assumed 2D flow conditions. For the open-channel flow conditions, this difference in the formulation had an impact in the solution in the initial stages of the simulations, since vertical acceleration and velocities were not negligible. One practical consequence was that the depression wave yielded by CFD solution was consistently ahead of analytical or 1D modeling solutions. In Figure 3.2, it could be noticed that the propagations of rarefaction wave of analytical solutions closely matched those of St. Venant models, but these were lagging behind those obtained with the CFD model. Studying the trajectories of the wave front in Figure 3.5 (a), in average the trajectory of 5% pressure change threshold from CFD models was closest to analytical solution, yet the celerity of the depression wave matched the analytical celerity best with the 1% pressure change threshold. This was explained by the fact

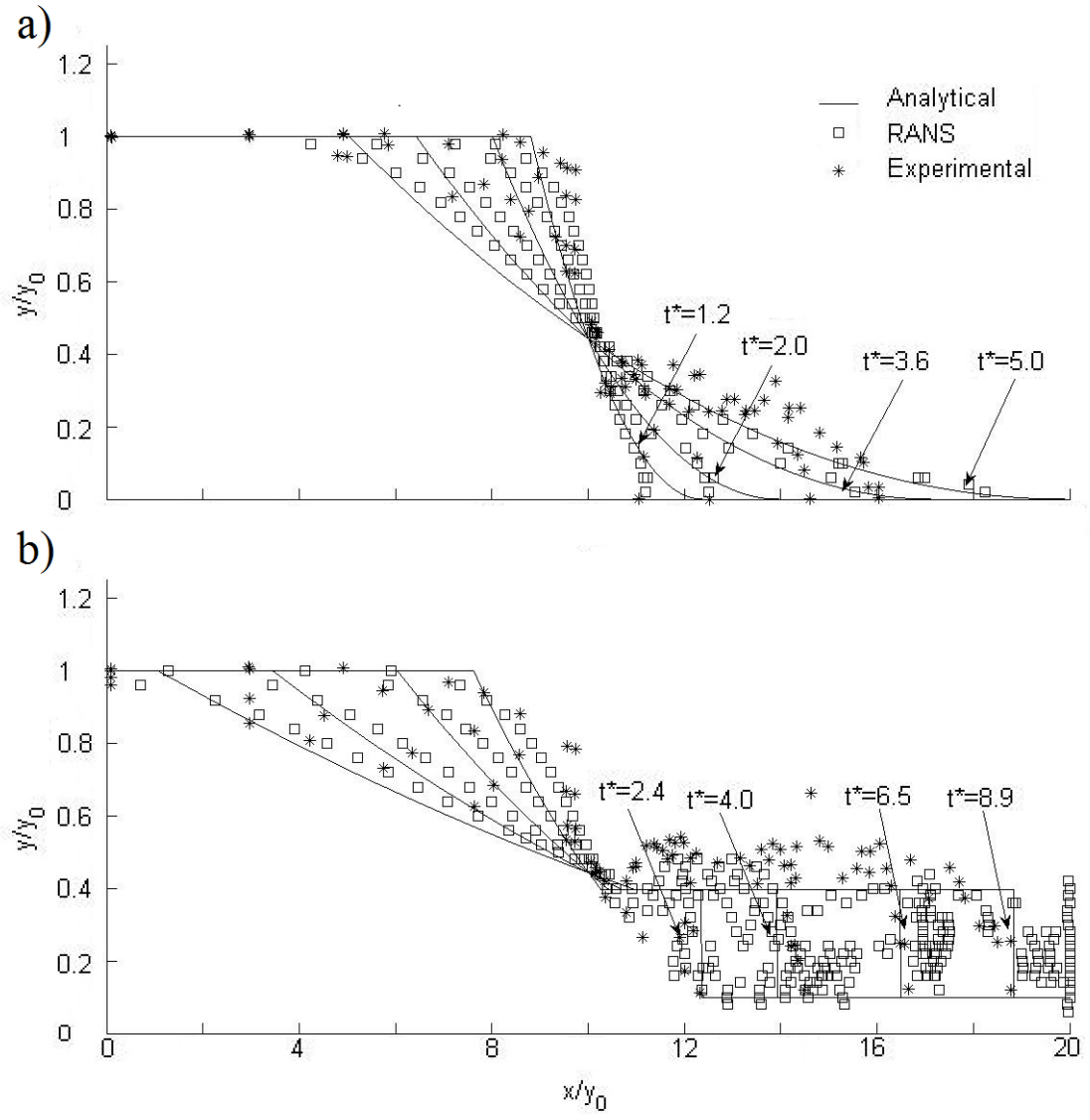

Figure 3.1: Experimental results compared with analytical solutions and CFD solutions

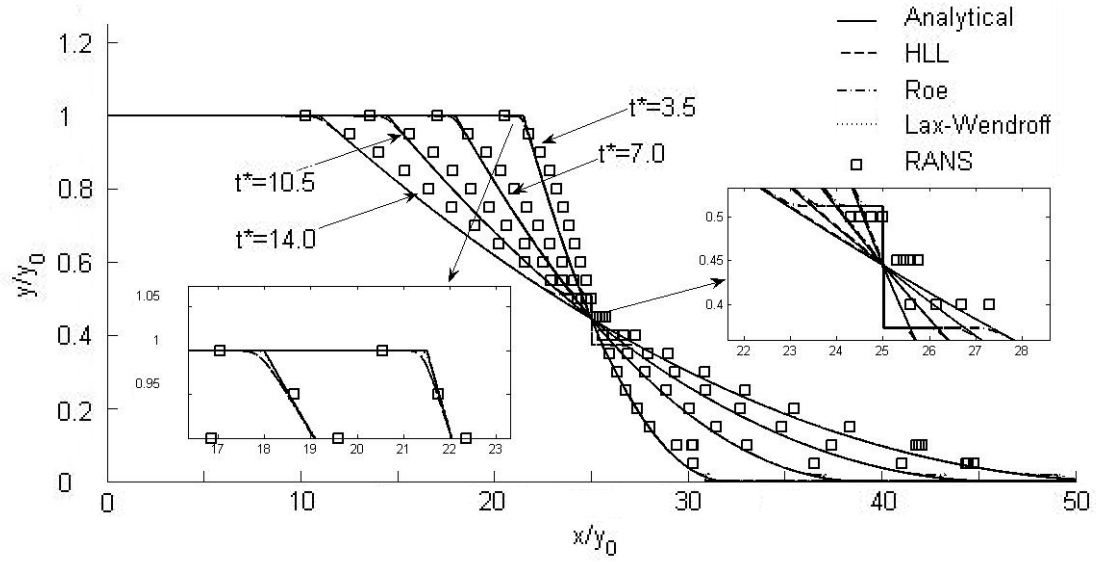

Figure 3.2: Surface profiles of dry bed downstream flow

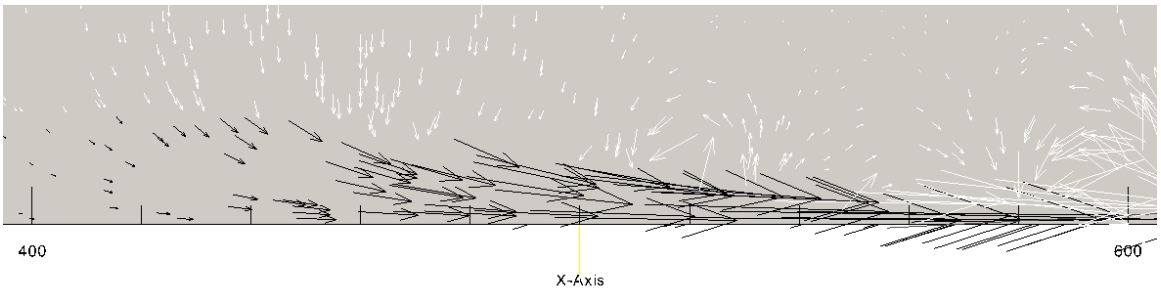

Figure 3.3: Velocity vector at $t^* = 3.5$, Dam site located at x=500m

that in the earlier stages of the simulation the CFD solution considered the 2D nature of the flow, which was not accounted properly in analytical or 1D results.

Figure 3.3 presented the velocity vector at $t^* = 3.5$. It was found that the vertical velocity upstream of the dam site position was not negligible. This explained clearly the source of the mismatch of the rarefaction wave propagations yielded by CFD and the other solution alternatives presented in this work.

3.3.3 Shockwave/bore modeling

The initial stage of the dambreak flow followed with the detailed shockwave features in this subsection. In Figure 3.2, CFD solutions of downstream surface profiles agreed well with St. Venant solutions except for Roe scheme solutions with entropy violating at the dam site, which

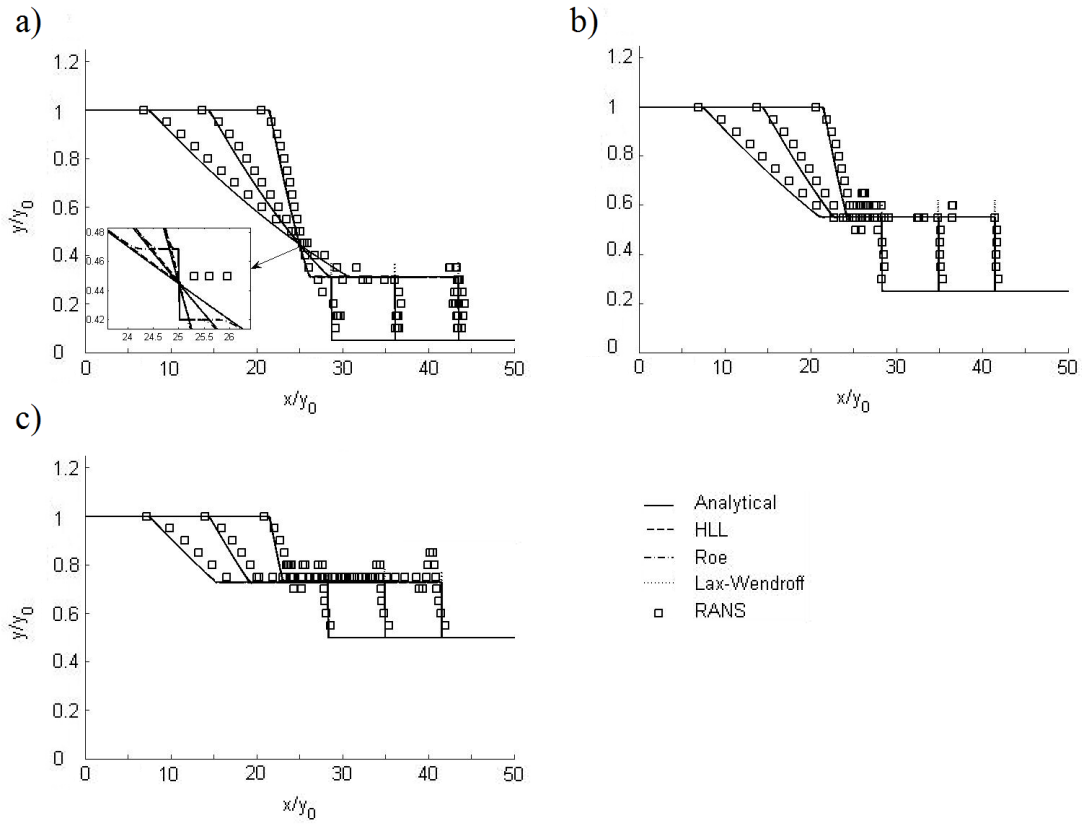

Figure 3.4: Surface profiles of (a, b, c) wet bed with 5%, 25%, and 50% downstream depth against upstream depth, respectively

also occurred in Figure 3.4 (a). However, all the numerical solutions slightly underestimated the feather tip front propagation obtained with analytical solution for dry bed condition. This was explained from the assumption of a very small (albeit non-zero) depth used in the 1D simulations. For wet bed conditions shown in Figure 3.4, the CFD solutions predict well the shock wave propagation for most tested cases. For the 50% depth ratio case shown in Figure 3.4 (c), the CFD bore front solution was ahead of the analytical and St. Venant solutions, and an undular front was observed. It was speculated that the CFD solution captured non-hydrostatic conditions that occurred when the depth ratio between the initial upstream/downstream sides of the dam was small. This condition has also been reported by Johnson (1972) and Mohapatra and Chaudhry (2004).

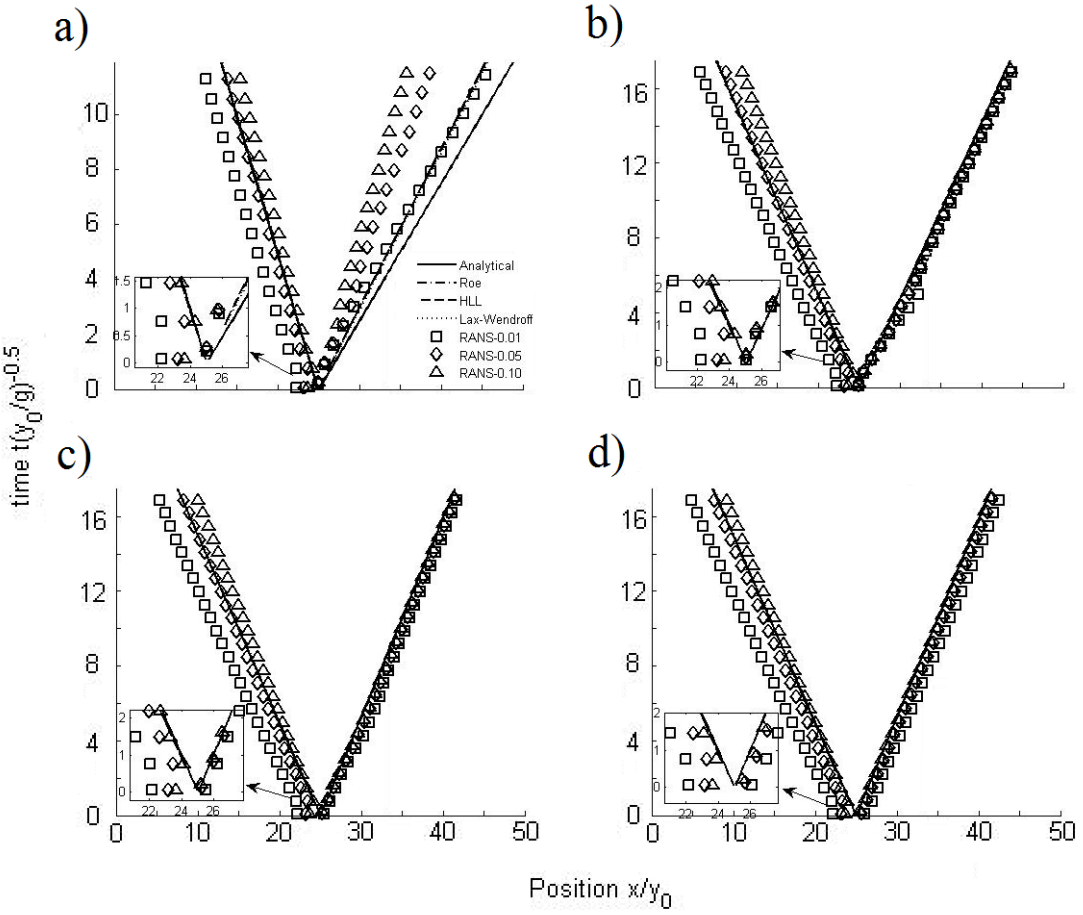

Figure 3.5: Trajectory of (a) dry bed downstream (b, c, d) wet bed with 5%, 25%, and 50% downstream depth against upstream depth, respectively

3.3.4 Depression wave and bore trajectories

Figure 3.5 presented the trajectories of both rarefaction waves and shockwaves for all depth ratio cases. It was printed that due to the 2D flow conditions at the initial stages of the flow, the rarefaction wave propagation yielded by CFD model was faster than that of the analytical solutions and St. Venant solutions. According to the trajectories, it could be concluded that the 1% pressure threshold is the best alternative to predict the rarefaction wave speed after the initial stages of the flow and the lag distance between the analytical solution and St. Venant solutions was observed only at the very beginning of the dambreak flow.

Regarding the bore front for the dry bed condition, the 1% pressure threshold trajectory agreed well with St. Venant solutions. While no simulation results were shown, lower pressure change thresholds for the CFD solution would progressively create better agreement with

analytical solution trajectories. For wet bed condition, different thresholds solutions did not present a clear trend in the comparisons between CFD and other models. For instance, the 1% threshold overestimated shockwave propagation for large downstream-upstream depth ratio, e.g. 50% depth ratio in Figure 3.5 (d).

3.3.5 Discretization impact in the CFD solution

As expected, mesh discretization influenced the computational efforts. Three different mesh resolutions were generated in this work, including $\frac{dx}{y_0} = 0.02$, 0.10, and 0.20. From the trajectory scatters of different mesh resolutions in Figure 3.6, one could note that a mesh independent solution was obtained. Besides, the computing effort in the simulations were also concerned. The CFD simulation was conducted with the small-parallel queue in Alabama Supercomputer Center (ASC), which had 2.26-2.5 GHz duo-core CPUs.

The simulations were performed with 8 cores parallel computing. The total CPU time and used memory were shown in Table 1. As the mesh size decreased from $\frac{dx}{y_0} = 0.2$ to 0.1, it cost 1.6-3.5 times more total CPU time and used 0.1-0.5 times more memory. However, as the mesh size changed from $\frac{dx}{y_0} = 0.1$ to 0.02, it cost about 100-200 times more total CPU time and used 2.6-4.2 times more memory. By examining the trajectory scatters in Figure 3.6, no clear accuracy improvement was observed between $\frac{dx}{y_0} = 0.1$ and 0.02. Therefore, in order to save computing resources, it is not recommended to refine the mesh in dambreak simulations beyond this mesh size of $\frac{dx}{y_0} = 0.1$.

3.4 Summary

The present chapter has compared and discussed different approaches (analytical, St. Venant, and CFD solutions) to 1D dambreak problems. Our findings could be summarized as follows:

- Analytical solutions underestimated the rarefaction wave propagation;
- Dambreak flow was 2D rather than 1D flow at the initial stages of the simulation because the vertical velocity/acceleration was not negligible, which in turn affected the simulation of the depression wave;

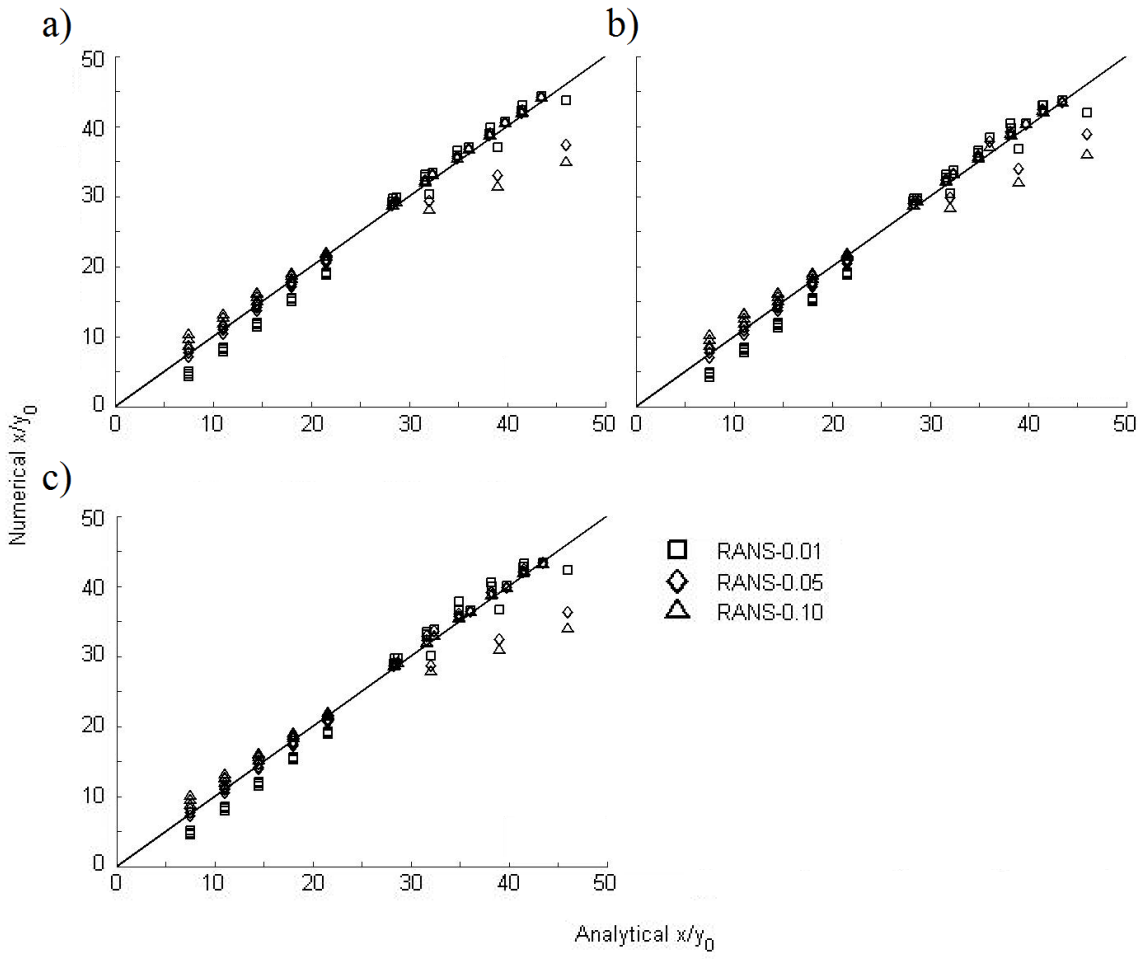

Figure 3.6: Trajectory Scatter of different mesh resolutions, $\frac{dx}{y_0}$ = (a) 0.20 (b) 0.10, (c) 0.02, data including different depth ratios cases

- Celerity of flow features predicted by CFD models based on lower pressure change thresholds agreed more closely with celerity from analytical solutions; and
- CFD mesh resolution $\frac{dx}{y_0} = 0.1$ was the most efficient alternative for mesh discretization for the purpose of this comparison between CFD and 1D modeling predictions.

The following chapter applies the CFD model with VOF method on another application, presenting a series of investigation on stormwater geysering caused by air pocket release.

Chapter 4

Flow Characteristics of Stormwater Geysering Caused by Air Pocket Releasing

4.1 Research objectives

As pointed out earlier, flow characteristics of stormwater geysering caused by air pocket releasing have been systematically studied by Vasconcelos and Wright (2011). However, the apparatus dimensions are not comparable with those of actual stormwater systems. One overarching goal of the investigation is to evaluate the displacement of water in conditions approaching real stormwater systems, with the goal of providing some guidelines to mitigate geyser events. As a results, CFD modeling need to be applied in conditions representing large scales and a series of systematic tests need to be implemented. In order to achieve this, four major objectives are proposed:

- To apply and calibrate a CFD model to describe the displacement of water in the vertical shaft of a series of experimental tests;
- To use the same CFD modeling strategy in larger scale conditions to understand, among other characteristics, the general trend of water displacement created by air pocket release from these shafts;
- To apply the CFD model on simulating geyser episodes created by the release of a sequence of air pockets;
- To propose and assess a geometric retrofitting strategy that can mitigate geyser triggered by the release of air pockets.

4.2 Methodology

4.2.1 Solver and governing equations

As explored in the previous chapter, the VOF method based CFD solver in OpenFOAM, interFOAM, is capable to describe unsteady two-phase flows. One limitation of interFOAM, however, is that it does not account for the compressibility of the air phase. As a result, early attempts in this investigation of simulating the process of air release and geyser events with interFOAM were not entirely successful. It was noticed that air compressibility was relevant even in the experiment scale used in the experiment by Muller and Vasconcelos (2016), which was later verified by the findings from Chan et al. (2017) that the air compression is one of the key factors in geyser process. An alternative interFOAM solver, compressibleInterFOAM, which is able to simulate non-isothermal immiscible flows, was adopted. The two-phase NSE with VOF method solved by compressibleInterFOAM can be expressed as Svenungsson (2016):

$$\frac{\partial \rho}{\partial t} + \nabla \cdot (\rho \vec{U}) = 0 \tag{4.1}$$

$$\frac{\partial (\rho \vec{U})}{\partial t} + \nabla \cdot (\rho \vec{U} \vec{U}) - \nabla \cdot (\mu \nabla \vec{U}) - \rho g = -\nabla p - F_S \tag{4.2}$$

$$\frac{\partial (\rho C_p T)}{\partial t} + \nabla \cdot (\rho \vec{U} C_p T) - \nabla \cdot (k_T \nabla T) = S_T \tag{4.3}$$

$$\frac{\partial \alpha}{\partial t} + \nabla \cdot (\alpha \vec{U}) + \nabla \cdot (\alpha (1 - \alpha) \vec{U_r}) = 0 \tag{4.4}$$

where ρ is the average density of the fluid within a cell, $\vec{U}$ is the flow velocity vector, μ is dynamic viscosity, g is gravity acceleration, p is pressure, F_S is the surface tension force, C_p is the specific heat, T is temperature, k_T is thermal conductivity, S_T is the energy source term, α is the fraction of water in the cell (between 1 and 0), and $\vec{U_r}$ is a velocity field suitable to compress the interface. Equations 4.1 to 4.3 represent mass, momentum, and energy conservations, respectively. Equation 4.4 is related to the compression effects on the interface. The standard $k - \epsilon$ model was applied to resolve the turbulence in current model as well. It should be noticed the boundary layer thickness in the present research was smaller than the mesh size.

The mesh in this section was generated with both blockMesh and snappyHexMesh (OpenFOAM Foundation, 2016), and the later is a polyhedral mesh generator that morphs existing mesh into the required mesh by cutting the mesh with the boundaries. The model setup, as well as mesh independence study, is introduced separately based on different geometric models in the following subsections.

4.2.2 Modeling of experimental conditions

The CFD model of geysering research was based on the scale model apparatus of a portion of a stormwater storage tunnel presented in Muller and Vasconcelos (2016). As shown in Figure 4.1, the apparatus contained one 13.7 m long, 302 mm diameter approximately horizontal tunnel, one about 4.8 m long vertical shaft of varying diameters (D_s =102 mm, 153 mm and 202 mm) connected at 10.7 m from the upstream point of the tunnel, one lateral 6 m long, 202 mm diameter air chamber to store and release air pocket with volume of V_a =0.1-m^3 or 0.2-m^3, and two reservoirs (volume 1.1 m^3 each) used to sustain pressures in the system during the air pocket releases.

Prior to the air pocket release, the system was filled with 2.5 m of water measured from the springline of the horizontal pipe, and the air phase in the lateral air chamber was set at preselected pressure values that represented the pressures in the water side of the apparatus. All the simulations involved water in quiescent conditions and the initial temperature in the simulation domain was setup as 27^{o}C, which was also applied as the value of fixed temperature boundary condition in the CFD model. The water level recorded with video cameras and pressure data collected with transducers at the location of P1, P2 and P3 shown in Figure 4.1 were used for the CFD model calibration. The CFD model replicated most of the apparatus details so that experimental results could be used to support the development of the model, helping to identify more adequate formulations and mesh characteristics. The model setup for different conditions are shown in Table 4.1.

The CFD model in the present work was created with the main objective of representing the kinematics of the air-water release in the experimental conditions. For the CFD simulation of the experimental apparatus model, three mesh resolutions were considered in the mesh

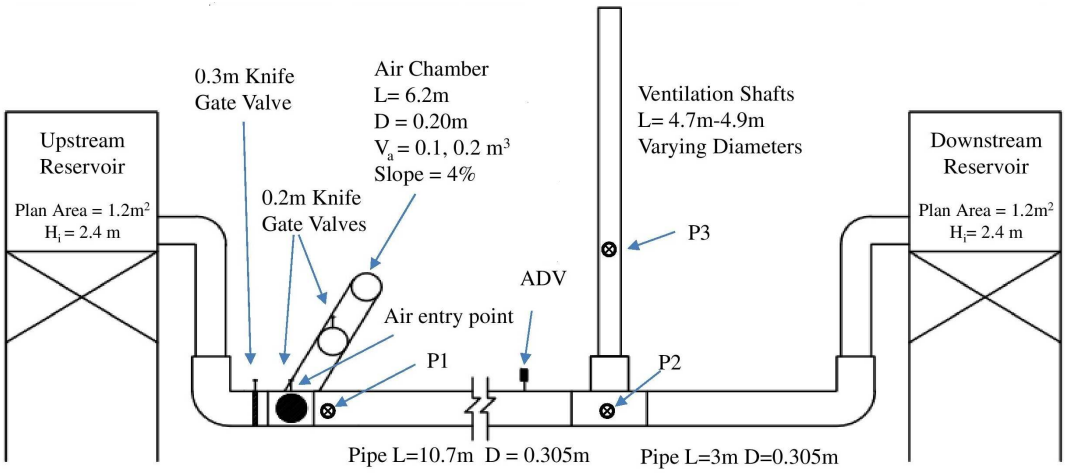

Figure 4.1: Sketch of experimental apparatus simulated with CFD approach

Table 4.1: CFD simulations model setup of experimental apparatus conditions

Shaft Size	Air Pocket Volume	
D_s =102 mm, L =4.74 m	0.1 m^3	0.2 m^3
D_s =153 mm, L =4.72 m	0.1 m^3	0.2 m^3
D_s =202 mm, L =4.88 m	0.1 m^3	0.2 m^3

independence study performed in the simulation of the experimental conditions (using a 153 mm diameter vertical shaft). The approximate mesh cell counted in the 153 mm diameter shaft were $5,000$ (1.4 million in the whole mesh), $44,000$ (2.2 million whole mesh), and $352,000$ (3.9 million whole mesh) for coarse, intermediate, and fine mesh sizes, respectively. As is shown ahead in Figure 4.4, the results of refined mesh converged to experimental data. Reasonably good agreement was achieved with the intermediate and fine mesh options, and intermediate mesh size was selected to perform most of the numerical simulations of this study.

4.2.3 Modeling of large-scale air pocket release

Once adequate CFD model setup was achieved and discretization was selected, a series of larger-scale simulations using a larger hypothetical tunnel geometry with varied sizes were performed using the modeling strategy applied to represent the experimental results. The hypothetical larger scale geometry was in general similar to the one used in the previous subsection model with means to sustain the water pressure with a reservoir and the presence of a single ventilation shaft in the horizontal pipe. Two key geometric differences were the absence of an

Table 4.2: Range of numerical variables considered in the CFD simulations of uncontrolled air pocket release in larger scale geometries

Variable	Range considered	Normalized range
Initial air pocket volume	V_a=1.0, 5.0, 10 and 50m^3	$V_a^* = Va/D^3$=1, 5, 10 and 50*
Initial water level at vertical shaft	$Y_{FS,0}$=10, 20 and 50m	($Y_{FS,0}/L$)=0.067, 0.133 and 0.333
Diameter of the ventilation shaft	D_s=0.25, 0.50 and 1.0m	$D_s^* = D_s/D$=0.25, 0.50 and 1.0

* Limited number of cases simulated with air pocket volume $V_a^* = 50$.

upstream reservoir, and the much longer vertical shaft of 150 m, of varying diameters. The horizontal tunnel diameter was 1 m and the length in most simulations was set to 60 m, not accounting the additional length that stored the initial air pocket volume. As it would be explained in the section presenting the modeling results of the larger-scale CFD study, in few cases the horizontal tunnel length was increased.

Compared to the CFD model setup of experimental apparatus model, a wider range of conditions was simulated for the large-scale model. Four different air pocket volumes were simulated, with three initial water depths in the vertical shaft and three different vertical shaft diameters. A total of 30 different conditions were tested, and are presented in Table 4.2. For all simulations, it was assumed that the roughness of the tunnel and vertical shaft walls was smooth. Also, it was assumed that the reservoir and vertical shaft were open to the atmosphere, and the air and water temperature was 27^o C.

4.2.4 Modeling of the release of a sequence of air pockets

The modeling studies discussed in subsection 4.2.2 and 4.2.3 focused on investigating geysers caused by the release of a single air pocket. Another CFD model was developed to study geysers triggered by the release of a sequence of air pockets. The geometry and boundary conditions of the models are sketched in Figure 4.2. The model was symmetric so that the computational effort could be reduced. The horizontal tunnel had a total length of 62 m with the diameter (D) of 1 m, containing the upstream inlet and downstream outlet. A vertical ventilation shaft, with the diameter (D_s) of 0.5 m, was located at 30 m downstream from the tunnel inlet. Above the vertical shaft, a 4 m-diameter, 15 m-height cylindrical open boundary

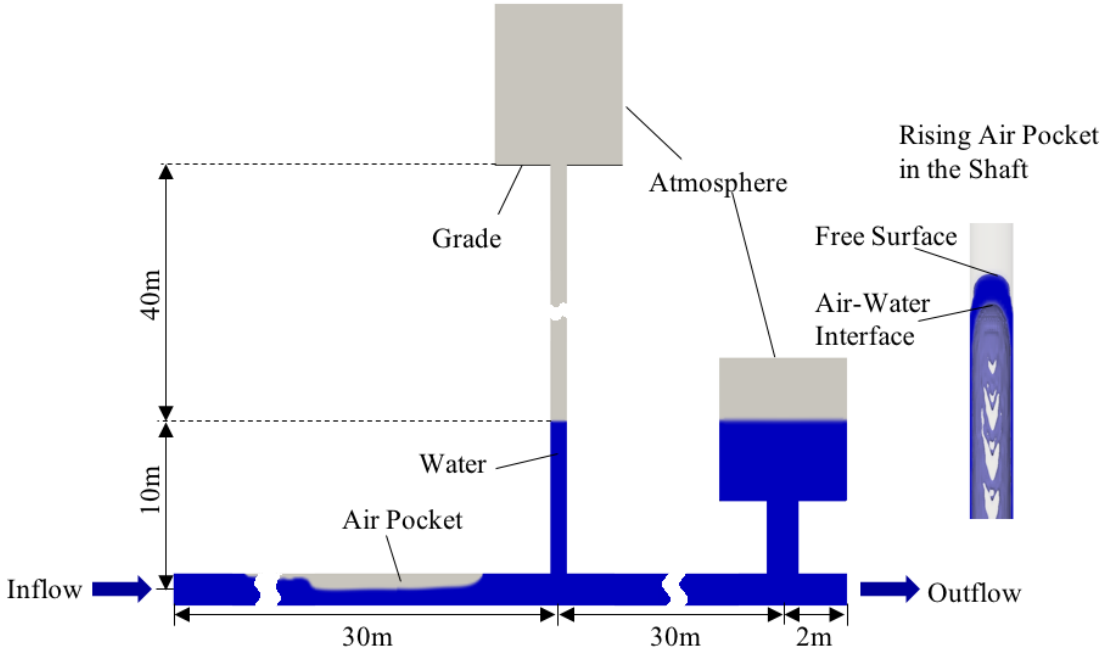

Figure 4.2: CFD model geometry and the boundary conditions

was added to investigate geyser after overflow. A 4 m-diameter downstream reservoir, open to the atmosphere, was located 2 m-upstream from the tunnel outlet to maintain pressure. In order to reduce computational effort, a 1 m-diameter vertical pipe was used for connecting the tunnel and reservoir. The initial water elevation in both vertical shaft and reservoir was set at 10 m. A constant ambient flow velocity (V_{am}) in the tunnel was setup as 1.566 m/s, which corresponds to $0.5\sqrt{gD}$. All the wall boundaries were setup with the same roughness of smooth concrete, and the initial temperature of the system was setup as 27^o C.

These simulations compromise flow characteristics when one single air pocket was released versus a sequence of smaller pockets with spatial separation. In the current model, a fixed volume of air pocket of $20m^3$ was released from the inlet using varying patterns for different scenarios, including one air pocket of $20m^3$, two air pockets of $10m^3$ each, and four air pockets of $5m^3$ each, following the steps below:

- The inlet boundary was setup as air phase inlet for a duration of t_0 to inject the first air pocket;

Table 4.3: Flow condition setup of the release of a sequence of air pockets

Scenarios	V5	V10	V20 (Baseline)
Total volume of air pocket (m^3)	20		
Volume of single air pocket (m^3)	5	10	20
Number of air pocket being released	4	2	1
Ambient flow velocity (V_{am}) (m/s)	1.566		
Duration (t_0) of the releasing of each air pocket (s)	4.07	8.14	16.28
Duration (t_1) between every two air pockets being released (s)	8.14	16.28	NA
Distance separation (L_1) between every two air pockets (m)	12.75	25.49	NA
Initial water elevation in the system (m)	10		

- The inlet boundary was then setup as water phase inlet for a duration of t_1 to separate the first and the second air pockets with a distance of $L_1 = t_1 Va$, while the first air pocket develops as gravity current and propagates downstream;

- Following Step 2, repeat Step 1 and 2 till the total volume of air pocket was completely injected, and the inlet boundary was then setup as constant water phase.

The details of the flow condition setup are listed in 4.3.

4.2.5 Modeling of geysering with extended shaft lower rim

The geometric model in the present subsection was based on the large-scale model in Section 4.2.2 with the retrofit of the extension of the lower rim of the shaft, as shown in Figure 4.3, comprising one 1 m diameter, about 60 m length horizontal tunnel with additional lengths added to account for the volume of air that will be released. The model was fitted with one large reservoir connected at downstream of the system to sustain pressure during the air pocket releasing, following the approach adopted by Lewis and Wright (2012). The water-filled vertical shaft was positioned approximately mid-length in the water section of the horizontal tunnel, and had 0.5 m diameter and 100 m of vertical length. For all tested conditions, the volume of air being released was equal to $20m^3$, and the initial water level in the vertical shaft was set to 20 m.

The lower rim of vertical shaft is extended toward the springline of horizontal tunnel by varying lengths, referred to as L_{es}. A total of six conditions have been simulated, with L_{es} values equal to 0.2 m, 0.30 m, 0.35 m, 0.4 m, 0.5 m, and no extrusion case. The thickness

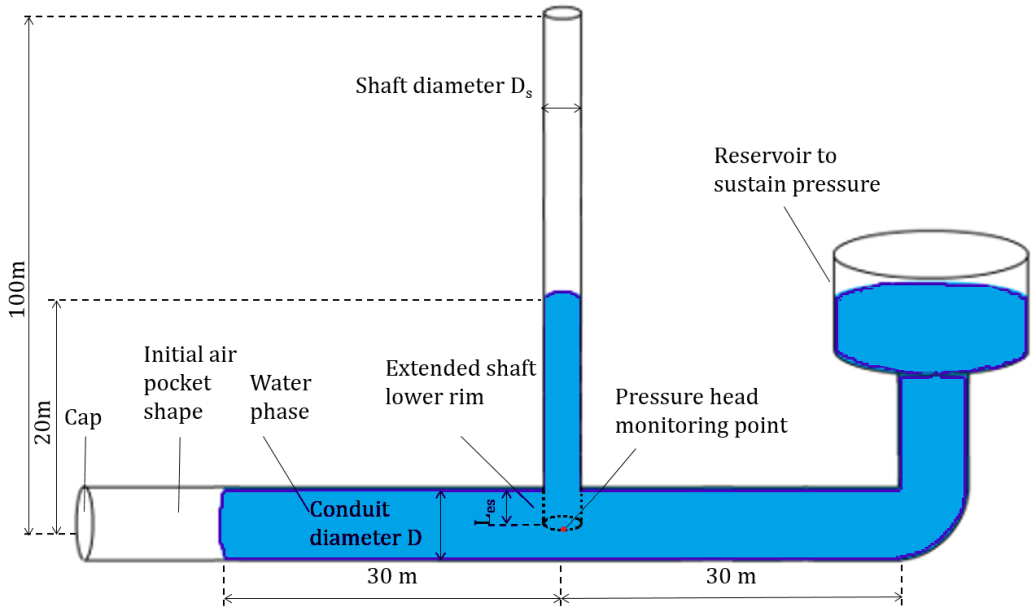

Figure 4.3: Sketch of the tunnel geometry represented with the CFD model

of the extended portion of the shaft walls was set as zero for simplicity. The roughness of all the walls in the system was assumed as smooth concrete, the shaft and tank were open to the atmosphere, and the initial temperature in the system was 27^o C.

4.3 Results and discussion

4.3.1 CFD comparison with experimental results

The first objective of the present chapter is to assess the ability of the compressibleInterFOAM solver to represent the experimental conditions. The CFD model was applied for all experimental cases, including three vertical shaft diameters and both 100L and 200L air pockets. In this work it was selected the condition with $D_s^* = 0.50$ (150 mm) and $V_a^* = 3.5$ (100L) to illustrate the characteristics of the numerical solution. In general, the other simulated conditions yielded comparatively good agreement with the experimental data, particularly with respect to the simulated displacement of the rising water free surface and air-water interface.

Figure 4.4 presented the comparison of the normalized displacement of the water free surface in the shaft (Y_{FS}) and air-water interface of the rising air pocket (Y_{Int}). Time was

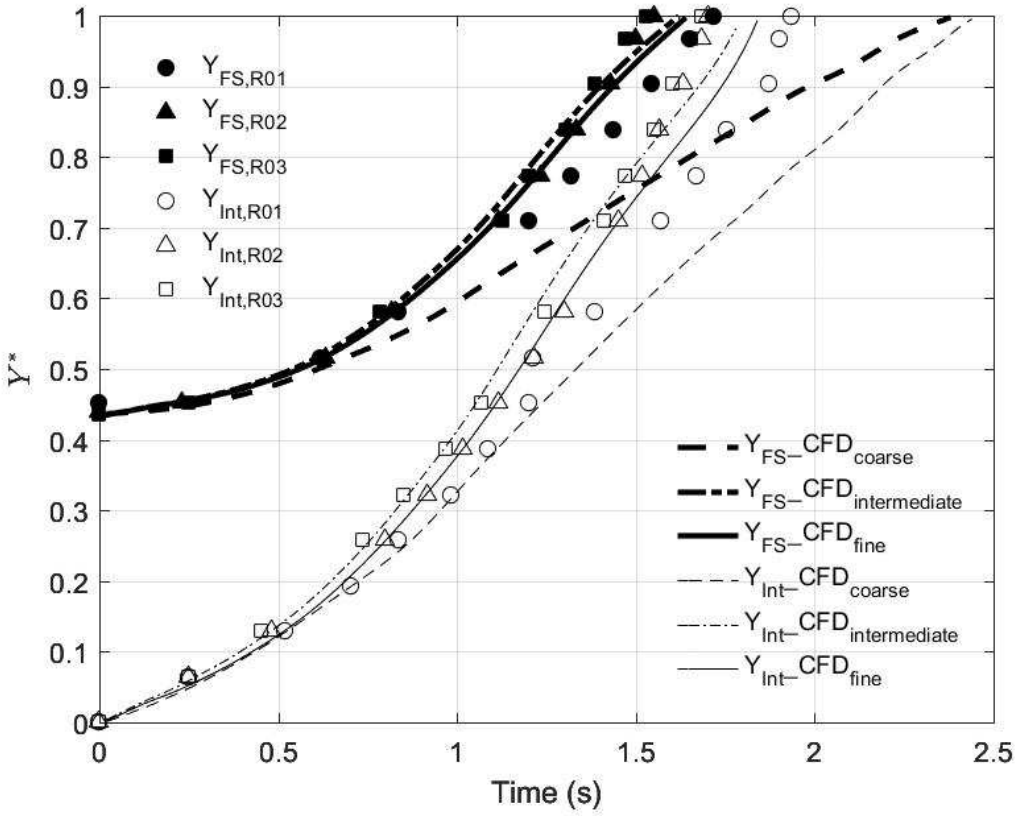

Figure 4.4: Normalized free surface and air-water interface displacement

referenced to the instant when the air pocket leading edge became visible in the vertical shaft. It was noticed that CFD modeling results match the measured data well, considering the natural variability among experimental repetitions. This agreement improved with the discretization, as was noticed comparing results obtained with the coarse mesh with intermediate and fine mesh results. It was also noticed that for both CFD and experimental results the air pocket and water column above the pocket rising process ended within 2 seconds, except for the results obtained with the coarse mesh.

Pressure head measured by transducer P3 (normalized by the shaft length L) were compared to CFD predictions at that location in Figure 4.5. In this run, water levels at the shaft were slightly 1.0 m above transducer P3 as air pocket arrived in the shaft. Simulated pressures presented the general trends observed during the experiments. This included the sharp pressure drop and rise after the pocket arrival at the shaft and the trend of maximum and minimum pressure head oscillations. Results with the intermediate and fine mesh sizes were similar, and in

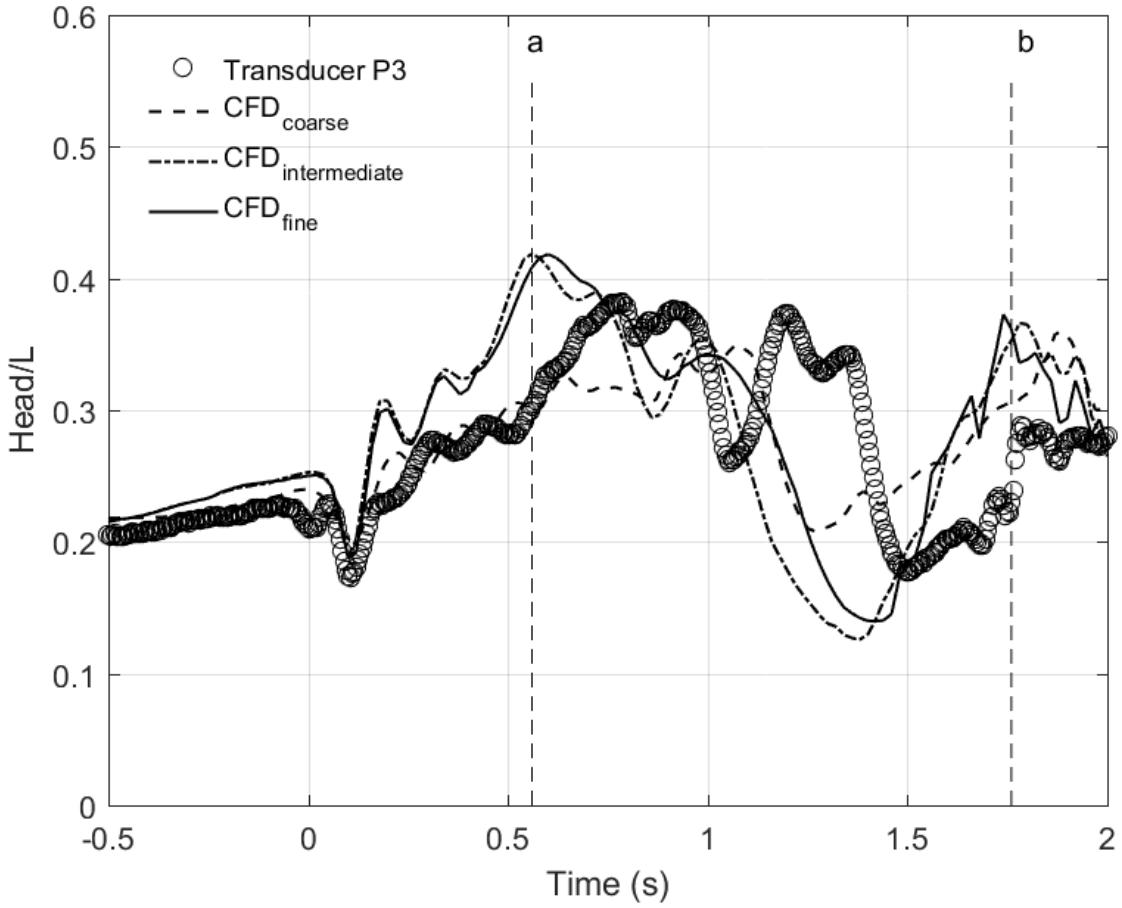

Figure 4.5: Normalized pressure head at transducer P3 on the shaft side. Vertical dashed lines referred to the time in the simulations when a) air pocket leading edge reached transducer P3 elevation; b) and air pocket breakthrough at shaft rim.

general yielded a closer match to the events observed in the experiments when compared to the coarse mesh results. Also, CFD-simulated pressure head results never exceeded the shaft rim elevation, even during geysering occurrence. The CFD pressure results were not as accurate as the simulation of the Y_{FS} and Y_{Int}, as there was over-prediction of pressure oscillations magnitude. There was also a delay between the CFD prediction of the air pocket arrival at transducer P3 and air pocket breakthrough at the shaft rim ranging from 0.1 to 0.2 seconds.

Results from this evaluation were considered positive, particularly with regard to the predictions of the free surface and interface coordinates during air pocket release. It led to the next group of numerical simulations, involving air releases in large geometries, as is presented in the following subsection.

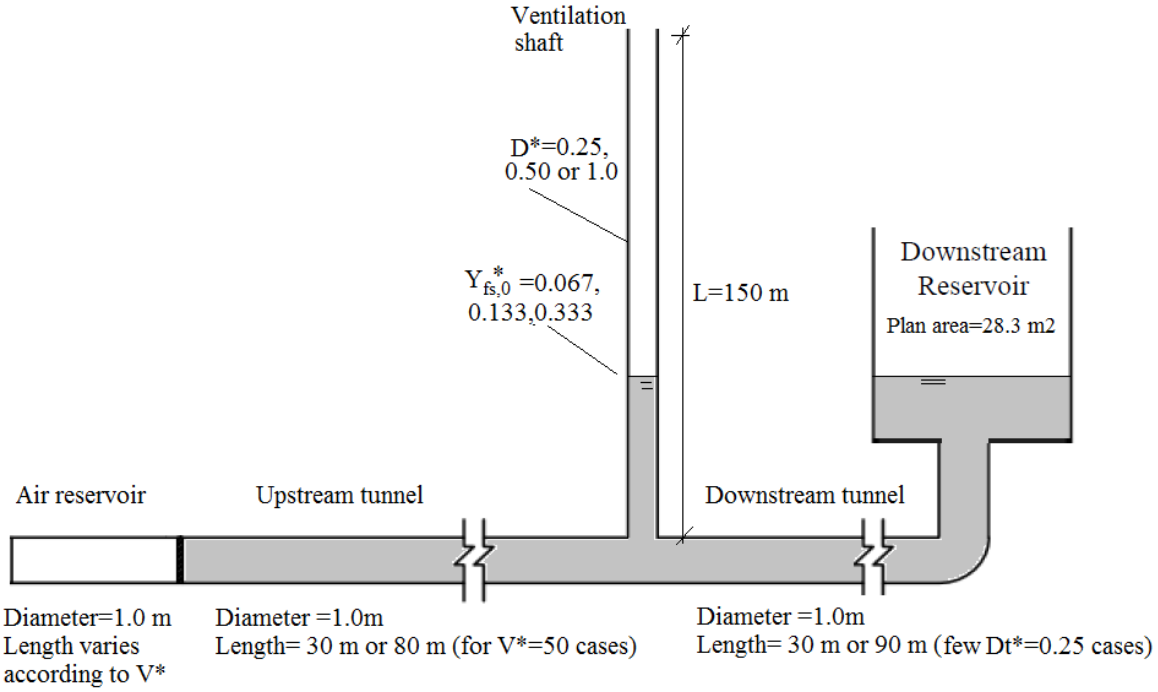

Figure 4.6: Geometric characteristics used on the large-scale CFD model. Conditions in the figure were representative of the start of the simulation.

4.3.2 CFD results of air pocket release in large geometries

As stated in the methodology section, a systematic evaluation of the effects of air pocket release using CFD was performed involving geometries that were larger than the ones used in the experiment by Muller and Vasconcelos (2016). The geometry used in this stage of the CFD result was in general similar to the one used in experiments, except that the upstream reservoir was absent, and is presented in Figure 4.6. The reservoir upstream was removed simply to reduce the size of the computational domain and thus speeded up computation. Air pockets would be released from this upstream end, at the opposite end from the water reservoir that sustains the pressure in the system. This study considered varying shaft diameters, initial water levels and air pocket volumes, using the CFD model developed in the stage of experimental results comparison. The range of tested conditions are presented in Table 4.2. The mesh size to tunnel/shaft diameter ratios that was used in this phase of the work was the same used in the intermediate mesh resolution of the CFD simulations representing the experimental conditions, which would also be applied in the rest of the CFD models regarding to pipeline systems.

The choice of air pocket volumes to be included in the numerical simulations was based on the work by Vasconcelos and Wright (2016). Air pockets volumes were categorized as small ($V_a^* < 2$), intermediate ($2 < V_a^* < 10$), large ($10 < V_a^* < 50$) and very large pockets ($V_a^* > 50$). As shown in Table 4.2, this stage of CFD simulation considered four pocket volumes ranging from small into very large air pockets. Simulation results involving $V_a^* = 1$ did not indicate any significant displacement of Y_{FS} in shafts for all D_s^*. Such results therefore would not be included in the present discussion. Also, it is pointed out that simulations with $V^* = 50$ were performed only for three cases: 1) $D_s^* = 0.50, Y_{FS,0}^* = 0.067$; 2) $D_s^* = 1.0, Y_{FS,0}^* = 0.133$; and 3)$D_s^* = 1.00, Y_{FS,0}^* = 0.333$. These tests with very large pockets needed a longer horizontal tunnel length filled with water of 110 m, with 80 m distance from the location the pocket was released to the base of the vertical shaft.

Figure 4.7 presents some typical flow patterns at the shaft junction as the air pocket entered the shaft. The three conditions represented were: (a) $D_s^* = 0.25$, $Y_{FS,0}^* = 0.133$, and $V_a^* = 10$; (b) $D_s^* = 0.50$, $Y_{FS,0}^* = 0.133$, and $V_a^* = 10$ and (c) $D_s^* = 1.00$, $Y_{FS,0}^* = 0.133$, and $V_a^* = 10$. As it is shown, the small shaft diameter ($D^* = 0.25$) did not capture larger fractions of the air pocket traveling in the horizontal tunnel, and the captured fraction increased with the shaft diameter. The maximum thickness of the rising air pocket core was not displayed in the figure, as it occurs along the centerline of the shaft.

This outcome was reflected in the amount of air mass in the vertical shaft when breakthrough occurred at the shaft rim, shown in Figure 4.8. Results in this figure were normalized by the initial amount of air in the system at the beginning of the simulation. Depending on the initial volume of air pocket and the initial water level in the shaft, the air mass fraction in the shaft ranged from 0.11 to 0.22 for $D_s^* = 0.25$, from 0.10 to 0.53 for $D_s^* = 0.50$ and from 0.14 to 0.71 for $D_s^* = 1.0$. There were few important remarks related to results presented in Figure 4.8. First, lower air mass fractions in the shafts may be linked in real stormwater systems to occurrences of multiple geysers, considering that simulations performed here were interrupted soon after breakthrough occurred. Second, small fractions of air mass in the shaft were noticed when very large air pockets $V_a^* = 50$ were released, which again was a possible indication that some large pockets could be ejected through a sequence of geysering events occurring in

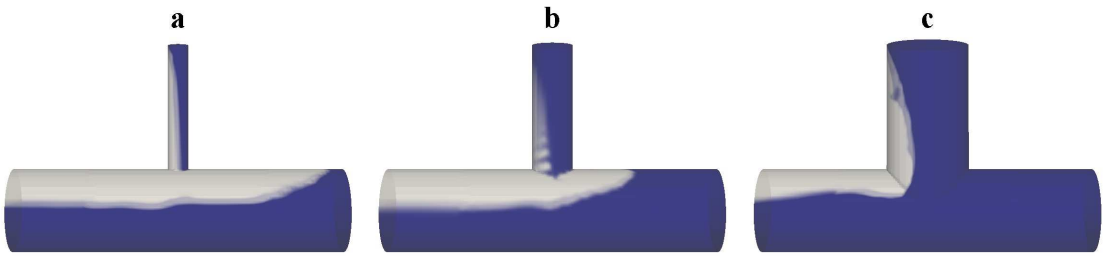

Figure 4.7: Typical early-stage air release patterns at shaft junction for large-scale simulation predicted by compressibleInterFOAM

succession rather than a single large geyser event. Finally, for a given value of $V_a^*$and $Y_{FS,0}^*$, the fraction of air within a shaft increased with D_s^*, a result that was intuitive based on the flow patterns presented in Figure 4.7.

One key objective of this work was to estimate the amount of water displacement during uncontrolled air release in shafts. Figure 4.9 presents simulated results of maximum incremental rise of the free surface ΔY_{FS}, normalized by $Y_{FS,0}$. It was noticed that $\Delta Y_{FS}/Y_{FS,0}$ values were influenced by the shaft diameter D_s^*, a result that was consistent with the experimental tests and with earlier investigations. While $\Delta Y_{FS}/Y_{FS,0}$ calculated with D_s^* values of 0.25 and 0.50 were similar, this value had decreased significantly when $D_s^* = 1.0$. These simulated $\Delta Y_{FS}/Y_{FS,0}$ could be potentially useful in estimating the maximum rise of water rise in stormwater shafts during uncontrolled air releases, and assess whether these displacements would have the potential of raising the free surface to grade and triggering geysers.

The maximum upward free surface velocity values in the vertical shafts are presented in Figure 4.10. These values, which were normalized by $\sqrt{gD}$, are useful because they were related to the air displacement within shafts and potentially to manhole cover displacement. Results presented in Figure 4.10 indicated that highest maximum velocities were observed for smaller $Y_{FS,0}$, a result that was expected since shorter initial water levels were linked to smaller inertia, and would be more easily accelerated. The maximum free surface velocity increased with air pocket volumes, and it was speculated whether this could be linked to the effect of decompression of larger air pocket volumes to the free surface location. Finally, an interesting result was that the highest normalized free surface velocities were observed for $D_s^* = 0.5$ and $Y_{FS,0} = 0.067$, with maximum velocity exceeding 24 m/s within the shaft. It was possible that

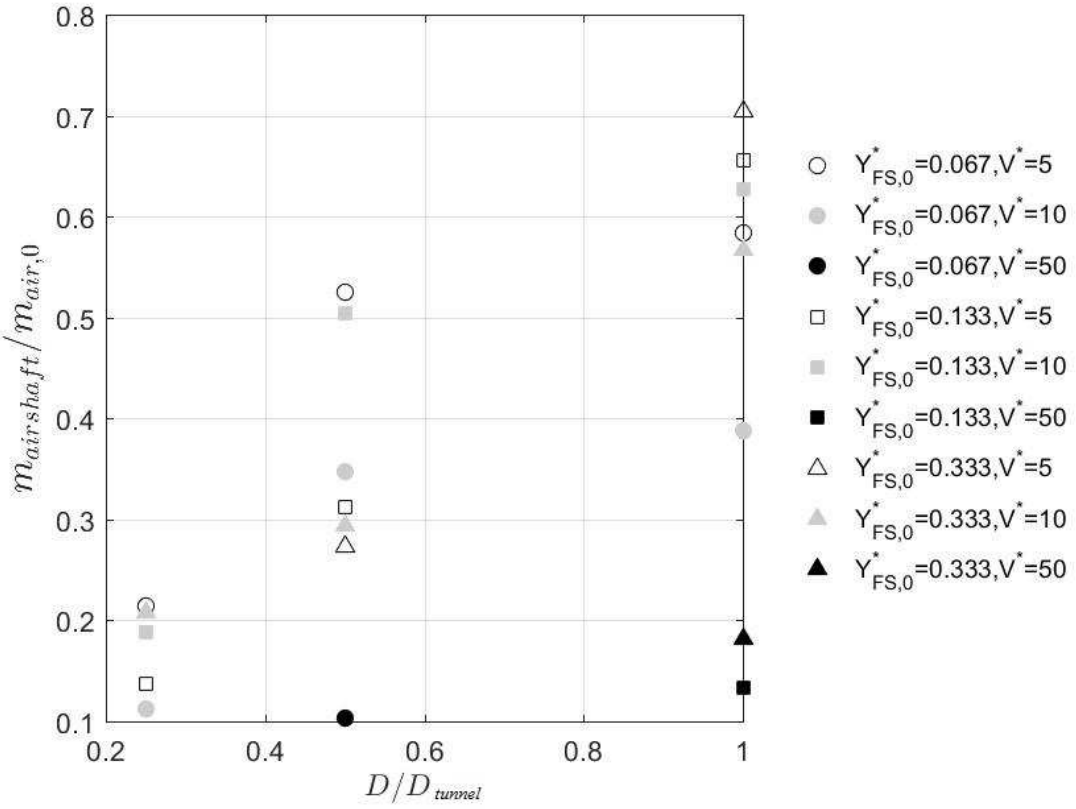

Figure 4.8: Normalized mass of air pocket captured in the shaft prior to air pocket breakthrough

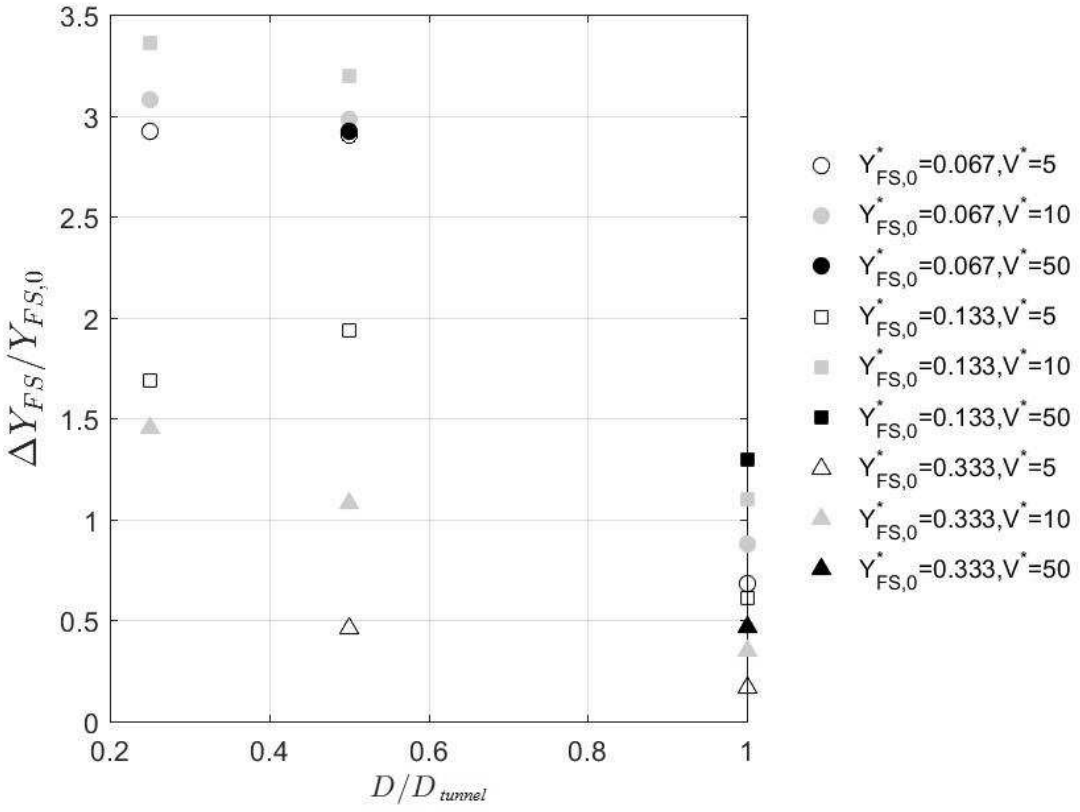

Figure 4.9: Normalized maximum incremental free surface displacement

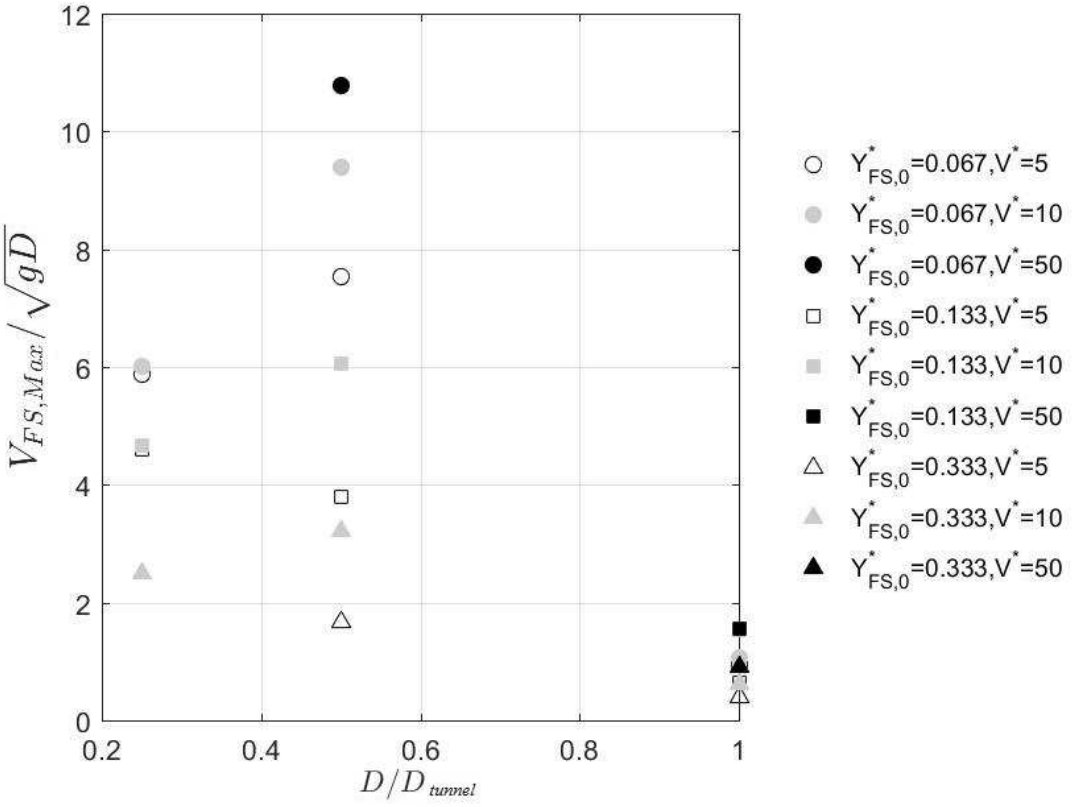

Figure 4.10: Normalized maximum free surface velocity

such outcome was linked to the ability of this shaft diameter to discharge larger fractions of air. There was a good agreement between the maximum velocity of the free surface calculated with the CFD model and the corresponding interface velocity $V_{Int,Max}$. The best-fit equation ($R^2 = 0.989$) relating $V_{Int,Max}$ and $V_{FS,Max}$, presented in Figure 4.11, is:

$$V_{FS,Max} = 0.970 V_{Int,Max} - 0.705 \tag{4.5}$$

The CFD model was also used to study the change in pressure at different locations in the vertical shaft as air pockets were admitted then expelled. Figure 4.12 presented the results for the case when $D_s^* = 0.50$, $Y_{FS,0}^* = 0.133$, $V_a^* = 10$, in which L was the physical length of the shaft. The following events were identified in the figure during the air release: a) air pocket entered the shaft; air pocket leading edge reached predetermined of elevations b) $Y^* = 0.033$, c) $Y^* = 0.067$, d) $Y^* = 0.100$ and e) $Y^* = 0.133$; f) water started to refill the base of the shaft;

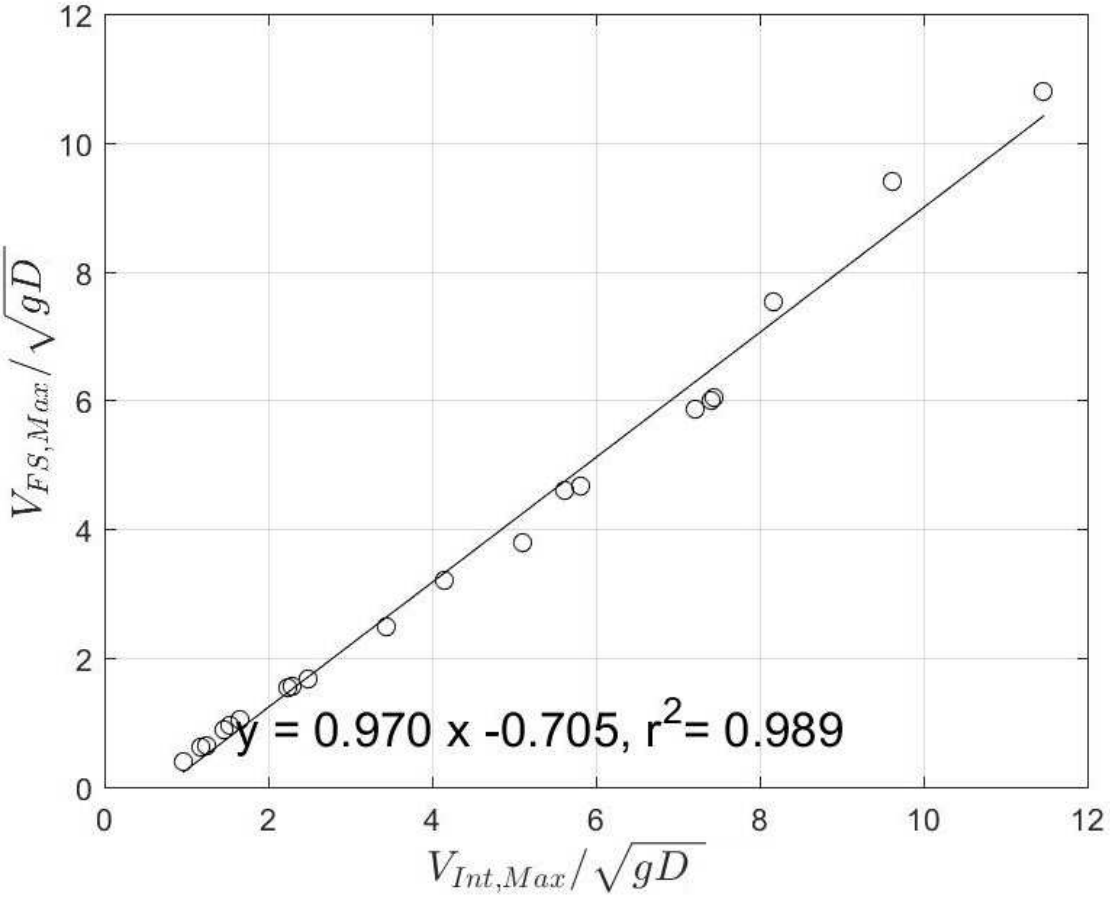

Figure 4.11: Normalized water-air interface velocity vs. free surface velocity

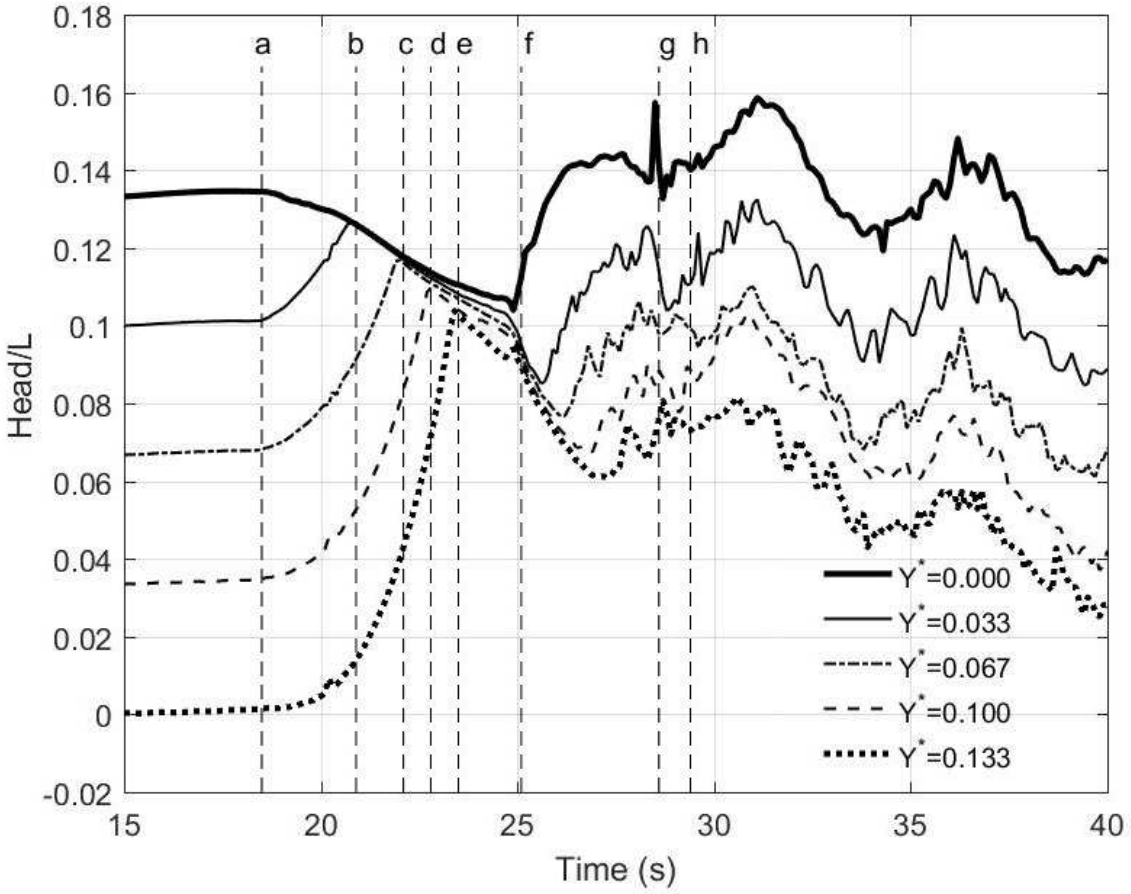

Figure 4.12: Normalized pressure head at different shaft elevations for case $D_s^* = 0.50$, $Y_{FS,0}^* = 0.133$, $V_a^* = 10$

g) water free surface reached the maximum elevation; h) air pocket breakthrough occurred. In this simulation, the maximum water level reached by the free surface was 83.8 m.

Pressure results prior to 18 seconds show that conditions were quasi-hydrostatic within the shaft. In the earlier stages of the pocket advance, between 18 and 25 seconds into the simulation, the air pocket delimited two regions in the flow. From the base of the shaft to the leading edge of the air pocket there was the air phase, which showed a decline in the pressure head (of about $0.03L$). Prior to the arrival of the air pocket to the elevation, simulated pressures were rising because of the displacement of the water surface ahead of the pocket motion. Between the markers e) and f) a difference in the air phase pressure head of $0.01L$ it was noticed.

At about t=25 s, the tail of the horizontal air pocket reached the base of the shaft, and water started refilling it. A complex flow pattern was observed at lower elevations of the shaft, with

a mix of air and water still rising in the flow. Pressure recovery was detected first at the base of the shaft, and this recovery propagated over a short time to the locations at higher elevations. This complex flow pattern continued from this point onward. After 30 seconds in the simulation there was no identifiable large air pocket in the shaft, but only a complex air-water bubbly mix that underwent inertial oscillations while discrete bubbles migrated upward.

The CFD results in this subsection led to a better understanding of the characteristics of air pocket releasing and the consequent geyser. The effects of the shaft diameter, initial air pocket volume, as well as initial standing water elevation had been explored. However, the knowledge on the ways of releasing air pocket, particularly the release of a sequence of air pockets, is still limited, which motivated the research on this theme.

4.3.3 Modeling of geyser created by the release of a sequence of air pockets

Figure 4.13 presents the evolution of geyser events triggered by the release of a single large air pocket ($V_a* = 20$). Time t=0s corresponded to the moment when the air pocket was injected into the horizontal tunnel. Not surprisingly, the air pocket became as gravity current and traveled downstream as described by Benjamin (1968), shown in Figure 4.13a. The white arrows in the figure represented the constant ambient flow velocity. Once the air pocket arrived the base of the ventilation shaft, it would move vertically and displace the initial water in the shaft, shown in Figure 4.13b and 4.13c. Figure 4.13d showed that after the air pocket rising and expansion, reverse flows from downstream tunnel was generated, probably because of the low pressure region at the shaft base. As the reverse flow traveled upstream, it could block the shaft base and refill the shaft, which separated the air pocket into two. Meanwhile, a strong geyser occurred and reached to the elevation over 10m above the grade (Figure 4.13f). Finally, the second portion of the air pocket was admitted at the shaft bottom and discharged as shown in Figure 4.13g, triggering geyser. The duration of this geyser event caused by the single large air pocket release lasted about 15 s.

For the multiple air pocket releasing scenario, i.e. V5 and V10, similar flow pattern would appear for the first released air pocket as described in Figure 4.13a, 4.13b, and 4.13c. One minor difference was that the air pocket was compressed from both sides for both Scenario V5

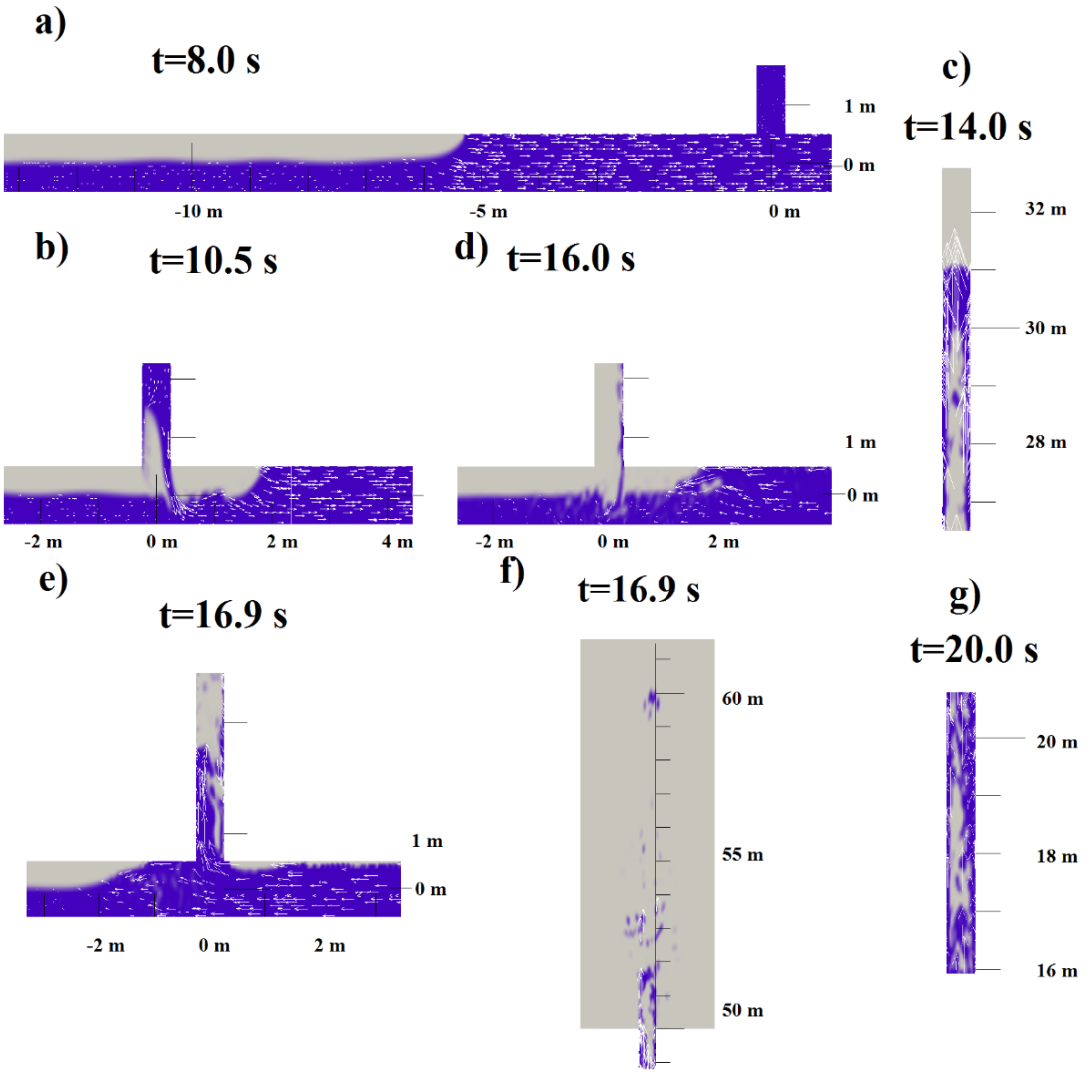

Figure 4.13: Evolution of the air pocket release and geyser from Scenario V20 (white arrows represent velocity vectors): a) air pocket traveling in the horizontal tunnel; b) air pocket admitting in the vertical shaft; c) air pocket moving upward and displacing water in the shaft; d) reverse flow propagating towards the shaft; e) reverse flow refilling the shaft and separating the air pocket into two; f) geyser occurring and reaching the maximum elevation; and g) the second portion of the air pocket releasing

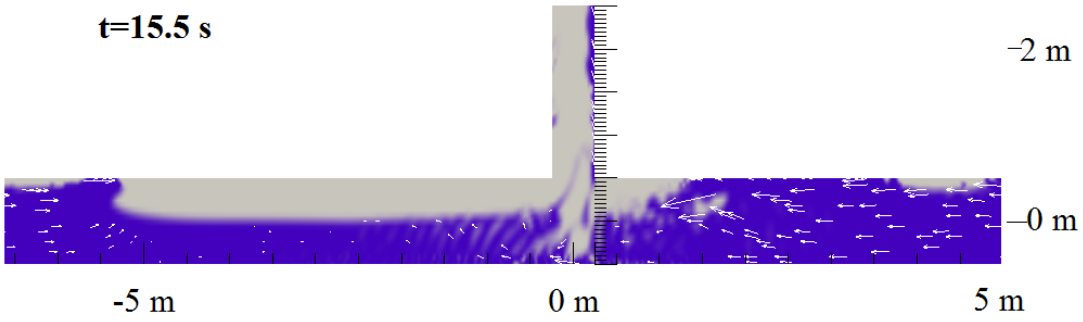

Figure 4.14: Flow compressing the air pocket from both sides from Scenario V10

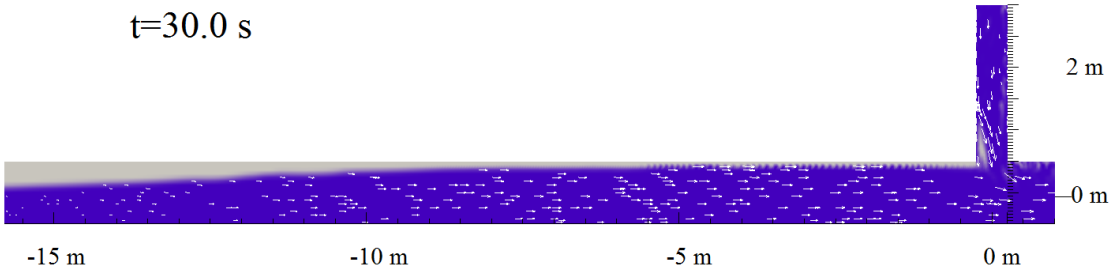

Figure 4.15: Wedged-type air pocket form Scenario V10

and V10 when the reverse flow appeared, shown in Figure 4.14. The lack of such flow pattern for Scenario V20 could be attributed to the model setup since the upstream tunnel was not long enough, Because of this flow pattern, the smaller air pockets investigated here were less likely to be separated by the flow reversal.

The first significant difference came from the second air pocket motion in the horizontal tunnel. Since the first air pocket release process would not able to expel all the air volume, a thin layer of long air phase tail was left behind at the pipe. This thinner layer interacted with the second released air pocket. As describe in Figure 4.15, the air pocket developed a long, wedge-like leading edge after interacting with the leftover of previous air pocket, instead of the original blunt leading edge of gravity currents.

The air pockets with wedge-like front changed the flow pattern as they entered the vertical shaft. As shown in Figure 4.16 from Scenario V10, when the first air pocket, having a blunt leading edge, entered the vertical shaft, it could immediately take over the majority of the vertical shaft cross section area; by comparison, when the second air pocket, having a wedged

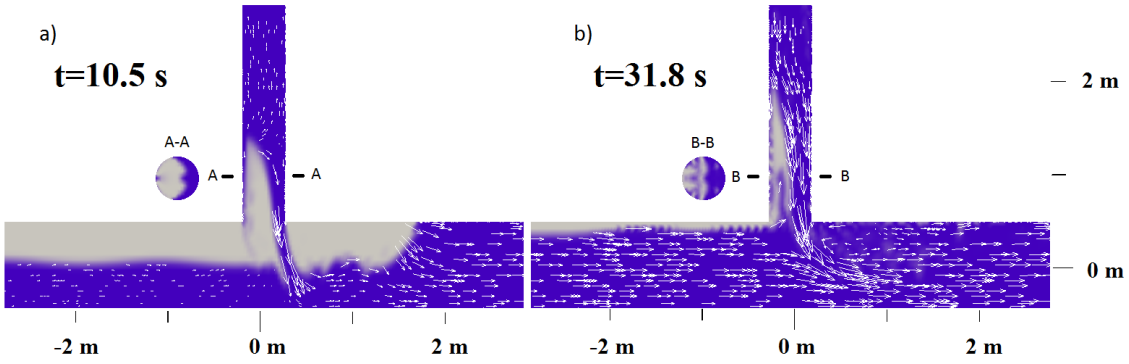

Figure 4.16: Symmetry plane and cross-section with velocity vectors of the air pockets when entering the shaft from Scenario V10: a) the first released air pocket; b) the second released air pocket

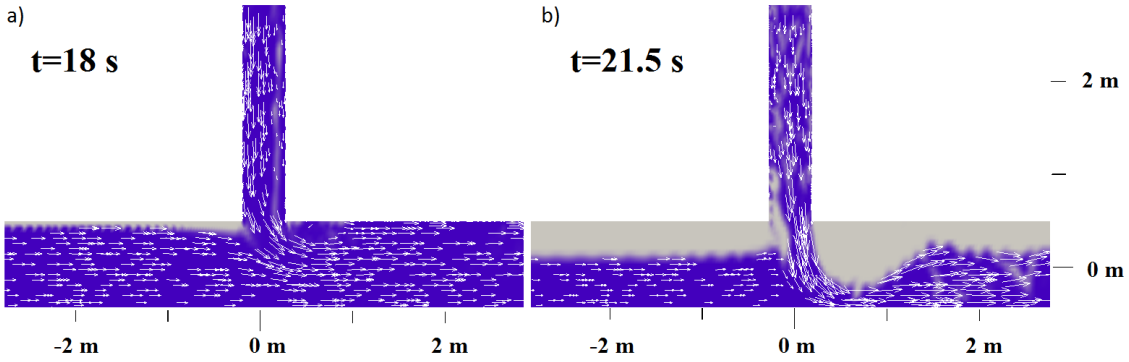

Figure 4.17: The second released air pocket with velocity vectors from Scenario V5: a) the leading edge arrived the shaft base; b) the leading edge started to move upward.

leading edge, entered the vertical shaft, it started to bubble gradually instead of occupying most of the shaft cross-section. This greatly reduced the water displacement within the shaft because of the downward flush as shown in Figure 4.16b.

However, the simulation results of Scenario V5 indicated that the bubbling flow pattern described in Figure 4.16b could be eliminated in some cases. Figure 4.17 presented an interesting phenomenon that the air pocket was barely admitted the shaft to the water flushing at the earlier stages of the vertical air flow.

The simulation results presented very complex flow patterns for the various Scenarios. Figure 4.18 and 4.19 presented the displacement and velocity evolution of the air-water interface, denoted by IF, and water free surface, denoted by FS, in the ventilation shaft, respectively. It should be noted that the air-water interface and water free surface could only be clearly

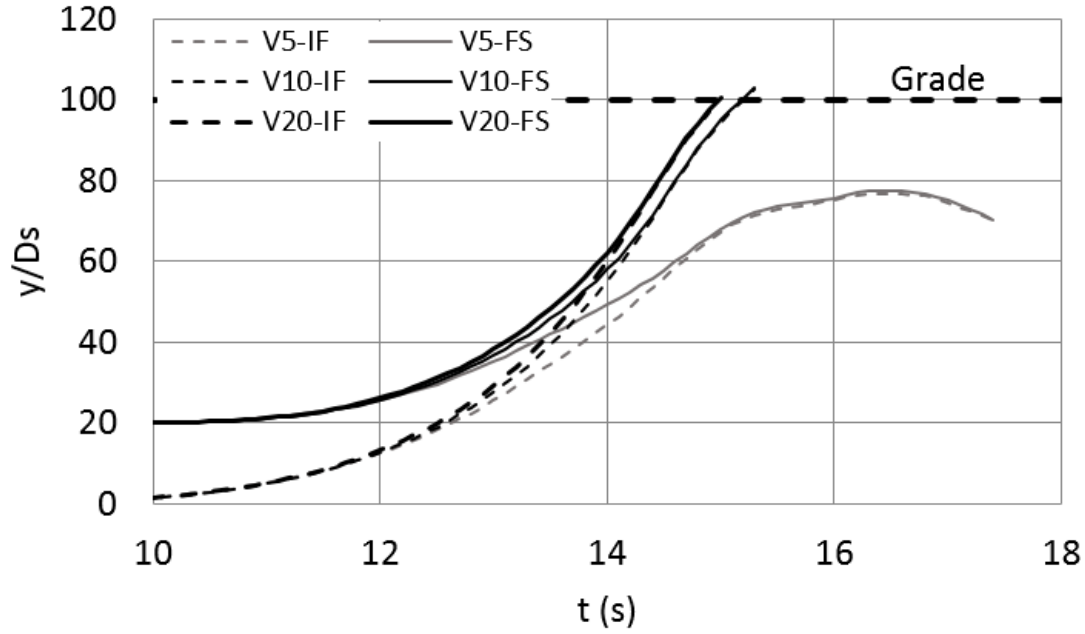

Figure 4.18: Evolution of normalized air-water interface (IF) and water free surface (FS) displacements

tracked during the release of the first air pocket due to the bubbly mix of water and air after the first release. Intuitively, it was possible to assess that for conditions involving larger volume of the initial air pocket released the free surface reached higher elevation. However, the fact of no significant difference between the Scenario V10 and V20 indicates that the effects of air pocket size on the initial water displacement would decrease when the air pocket size is sufficiently large.

Figure 4.20 presented the simulated maximum evolution of water/water droplets with the threshold of the water volume fraction greater than 0.1. According to this figure, several geyser events could be identified, including the 15 s-long geyser that was presented early for Scenario V20. This sequence of geyser breakthrough from Scenario V20, showing that a single large air pocket was also able to trigger several breakthroughs, implied that a single large air pocket could break into several air pockets, as expected in the previous subsection.

The results of Scenario V5 showed that the maximum water/water droplets increased dramatically from the first release of air pocket to the second one, and then gradually decreased for the following two pockets. In details, the water/water droplets could be displaced only up

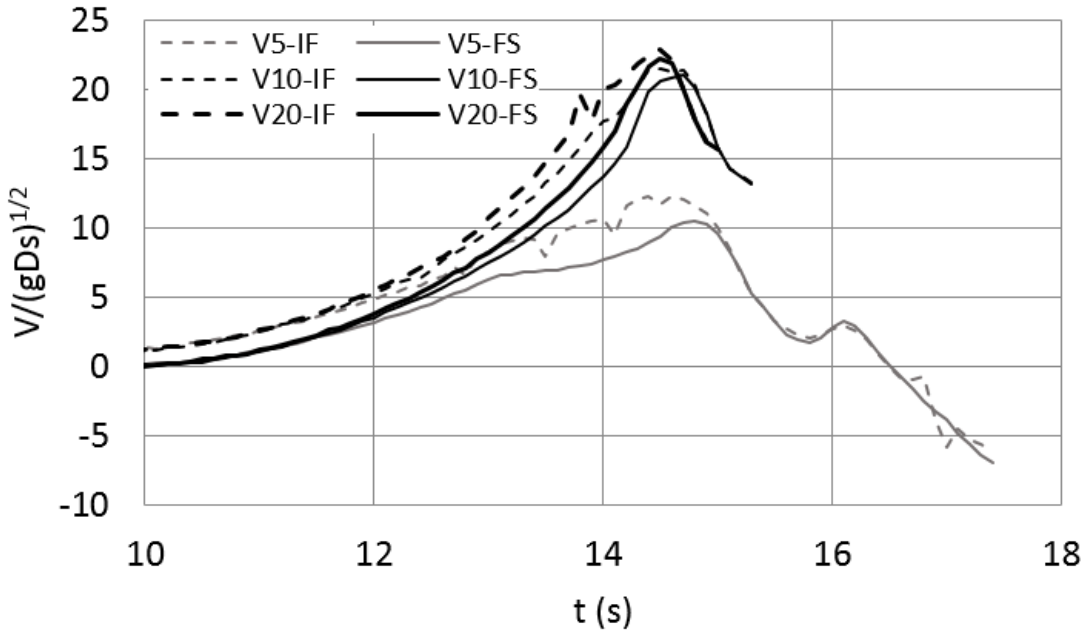

Figure 4.19: Evolution of normalized air-water interface and water free surface velocities

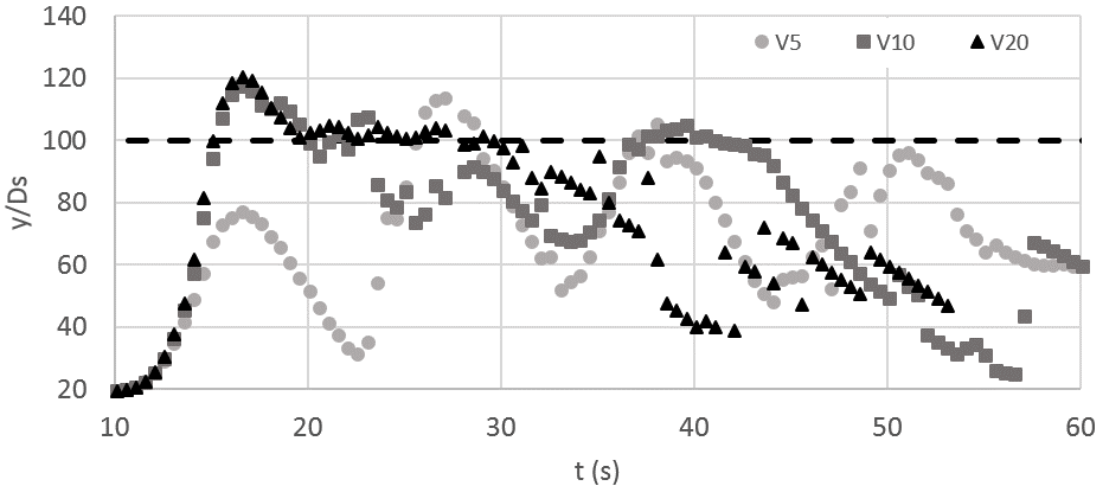

Figure 4.20: Evolution of normalized maximum elevation of water/water droplets

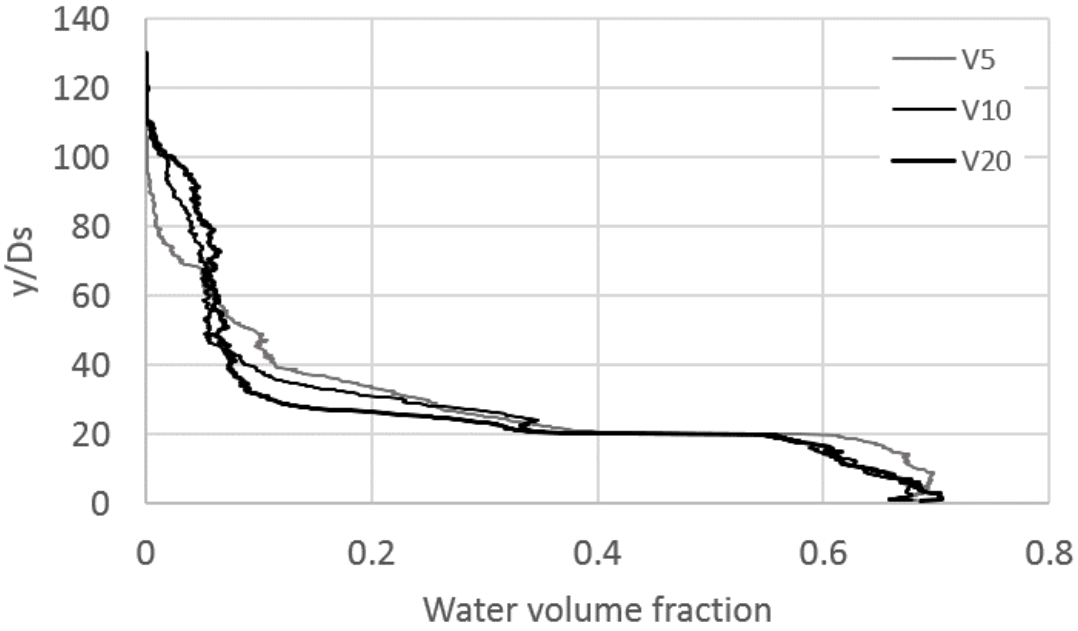

Figure 4.21: Time-averaged ($0 < t < 53s$) water volume fraction distribution along the shaft elevation

to 38.8 m by the first air pocket, yet that could be 57.1 m for the second release, 53.4 m for the third one, and 49.3 m for the fourth one. Such observation could possibly be attributed to the water inertial oscillation and the existence of more air-water mixture after the first air pocket being released. In comparison, the highest water/water droplets elevation induced by the second air pocket release was lower than the one induced by the first one for Scenario V10, which agreed with the observation that more volume of water flows from the shaft into the tunnel when the second air pocket was admitted.

It is proposed a new method to describe the geyser intensity by time-averaging the water volume fraction during the air pocket release events. The higher volume fraction value of Scenario V10 and V20 at high elevation in Figure 4.21 is linked to more intense geysers, while their relatively low value at lower elevations represented faster release of larger air pockets.

Figure 4.22 presents the pressure oscillation results at shaft location for all air pocket release simulations. Comparing the results of Scenario V10 and V20, it was noticed that the release of the first air pocket generates similar pressure oscillation patterns. But the lowest

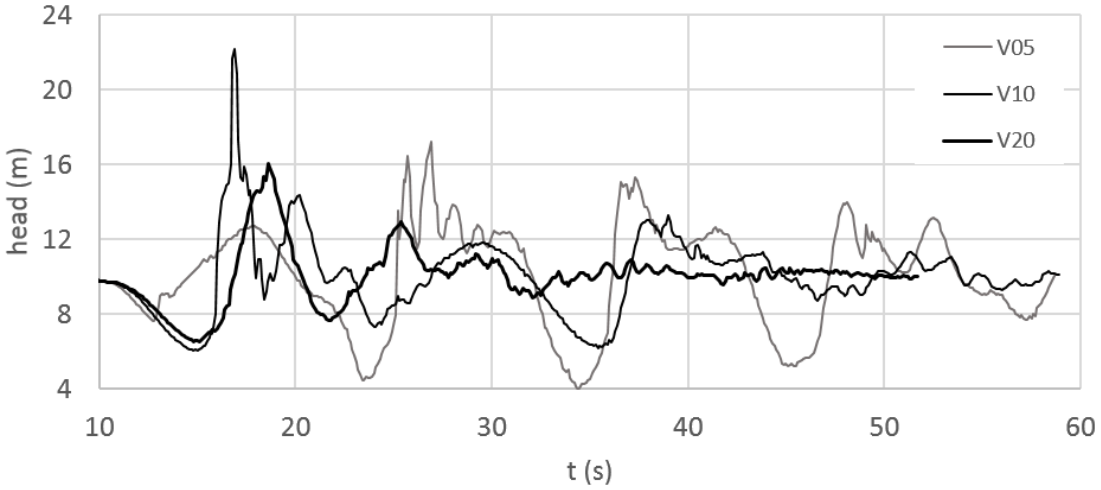

Figure 4.22: Pressure oscillations monitored at the bottom of the ventilation shaft

pressure head at about t=15 s in Scenario V10 is consistent with the observations of flow reversal in this case. It was also interesting to find that in Scenario V5, the magnitude of pressure oscillation was magnified by the sequence of air pocket release while the first air pocket could cause only about half value of the pressure oscillation magnitude caused by the following ones. In contrast, the pressure oscillation magnitude of Scenario V10 was not magnified by the second released air pocket, which could also be attributed to the longer separation of the two air pockets. Clearly, this conclusion can not be generalized as it is conditioned to the geometry that was used in this work.

Figure 4.23 is very similar to Figure 4.22 but relates the pressure evolution and flow velocity at 0.5m downstream of the shaft bottom. It is interesting to notice that the reverse flows, with a maximum magnitude of 4m/s, corresponded to pressure recovery at the shaft bottom. It was also noticed that no reverse flow was observed when the first air pocket was released for Scenario V5, which created the smallest changes on water/water droplet elevation. Such flow feature may indicate that the existence of reverse flow at the shaft bottom region is relevant to the geyser intensity.

So far, the present research resulted in a validated CFD model that described the geyser flows associated with air pocket release through vertical shafts. Many flow characteristics are

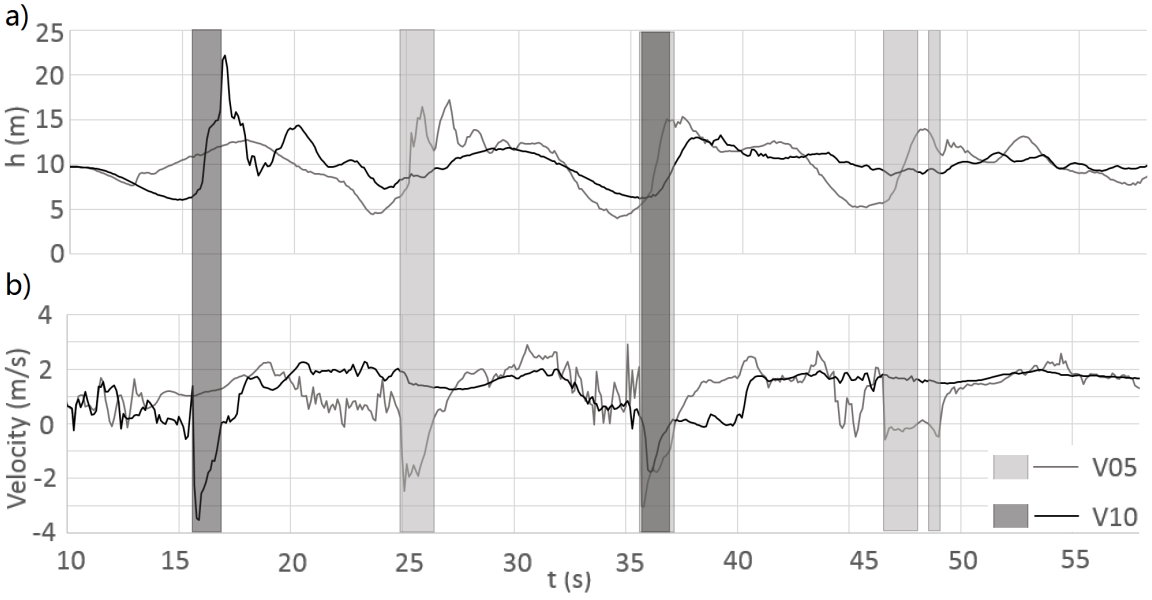

Figure 4.23: Pressure oscillations monitored at the bottom of the ventilation shaft

presented, but there was no focus on proposing a mitigation strategy . This is the focus of the next subsection.

4.3.4 Assessment of a retrofit strategy in dropshafts impacted by geysering

The initial objective of the present subsection is to evaluate the effectiveness of varying lengths of shaft extensions (L_{es}) into the horizontal tunnel with the goal of eliminating air release through water-filled shafts. This study took one possible ratio between shaft diameter and horizontal tunnel diameter ($D_s/D = 0.5$) as the selected condition for all numerical runs. Such conditions was shown to create significant free surface displacement as introduced previously. By extending different length of the shaft lower rim, less air was expected to be discharged and smaller free surface displacement were expected. Similar as the geyser simulations introduced earlier, once the air pocket is released in the horizontal pipe advanced toward the vertical shaft as a gravity current, with the leading edge velocity approximately equaled to $0.5\sqrt{gD}$. After few seconds into the simulation, the air pocket reached the shaft, and varying amounts of air were diverted into the tower due to varying L_{es}/D.

The simulated results of the captured air mass by the vertical shaft, normalized by the initial air pocket mass ($m_{a,0}$) are presented in Table 4.4. These results indicate that less air

Table 4.4: Air mass and maximum free surface velocity

Variable	L_{es}/D					
	0	0.2	0.3	0.35	0.4	0.5
Normalized air mass captured by shaft*	0.5041	0.3300	0.2450	0.0594	0.0231	0.0177
Maximum free surface velocity (m/s)	16.5	7.7	6.0	0.9	0.3	0.3

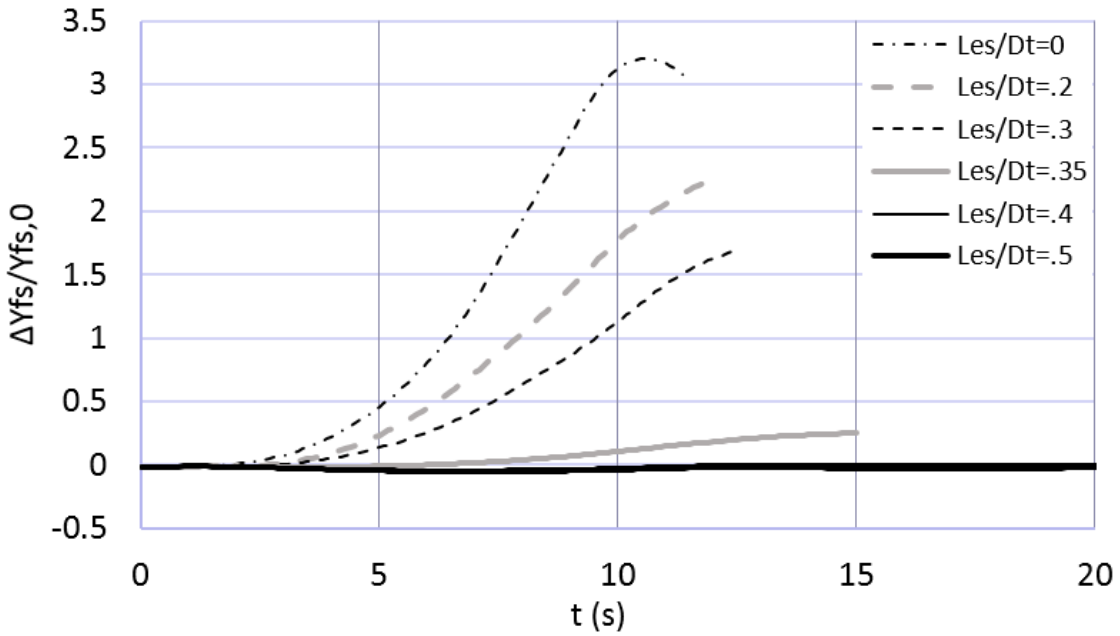

Figure 4.24: Normalized incremental free surface displacement

mass would be discharged for increasing L_{es}/D_t. With $L_{es}/D = 0.5$ extension, less than 2% of the initial air pocket mass was discharged through the shaft, while over 50% of initial air pocket mass was discharged when $L_{es}/D = 0$. Numerical results indicated that the captured air mass decreased significantly by elongating the extension from $L_{es}/D = 0.3$ to 0.35, which implied the effectiveness and efficiency of this retrofit strategy is sensitive to this geometry variable at this range.

As the amount of air discharge in the shaft increased, so did the measured displacement of the water free surface in the shaft. Large displacements could lead to geysering, thus this was an important variable to investigate in these studies. The free surface displacement was represented here in terms of the incremental displacement ΔY_{fs}, normalized by initial water depth $Y_{fs,0}$, and results are presented in Figure 4.24. The initial time (t=0) corresponded to the moment when the air pockets reached the location where the shaft was located.

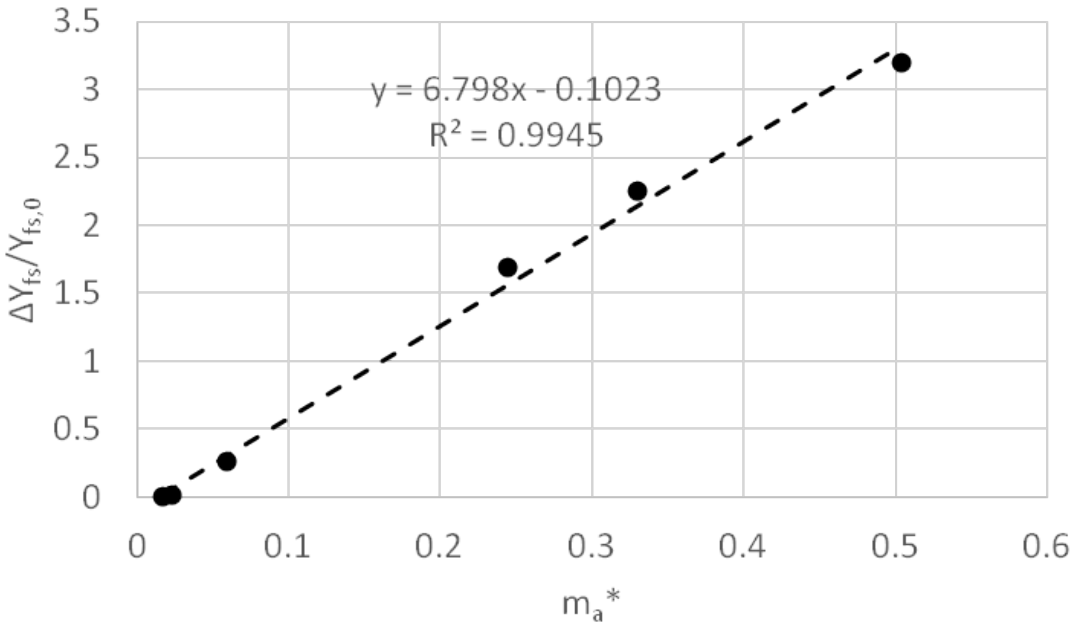

Figure 4.25: Dependence of free surface displacement with captured air mass for varying conditions of L_{es}/D

The results indicated that for the lowest L_{es} values, very small free surface displacements were predicted. Particularly, when $L_{es}/D = 0.4$ and 0.5, significant free surface displacement was virtually eliminated. For cases with $L_{es}/D \leq 0.35$, the amount of air pocket created an interface that resembled a Taylor-Davis bubble, which created significant mass displacement of water as it rised and expanded in the vertical shaft. This process was completed when the air pocket breakthrough atmospheric air. Following breakthrough there was a complex air-water flow pattern in shafts resembling a chaotic bubbly flow, but the free surface elevation did not reach the same levels observed for conditions with smaller L_{es} values during the initial air pocket rising phase.

Another correlation between the maximum free surface displacement and L_{es}/D can be illustrated through Figure 4.25, in which m_a^* is plotted against $\Delta Y_{fs}/Y_{fs,0}$. With larger L_{es}/D the mass of air that was captured in the shaft decreases. A quasi-linear relationship is noticed between captured air mass and shaft free surface displacement. While interesting, this result also can not be generalized to other shaft geometries.

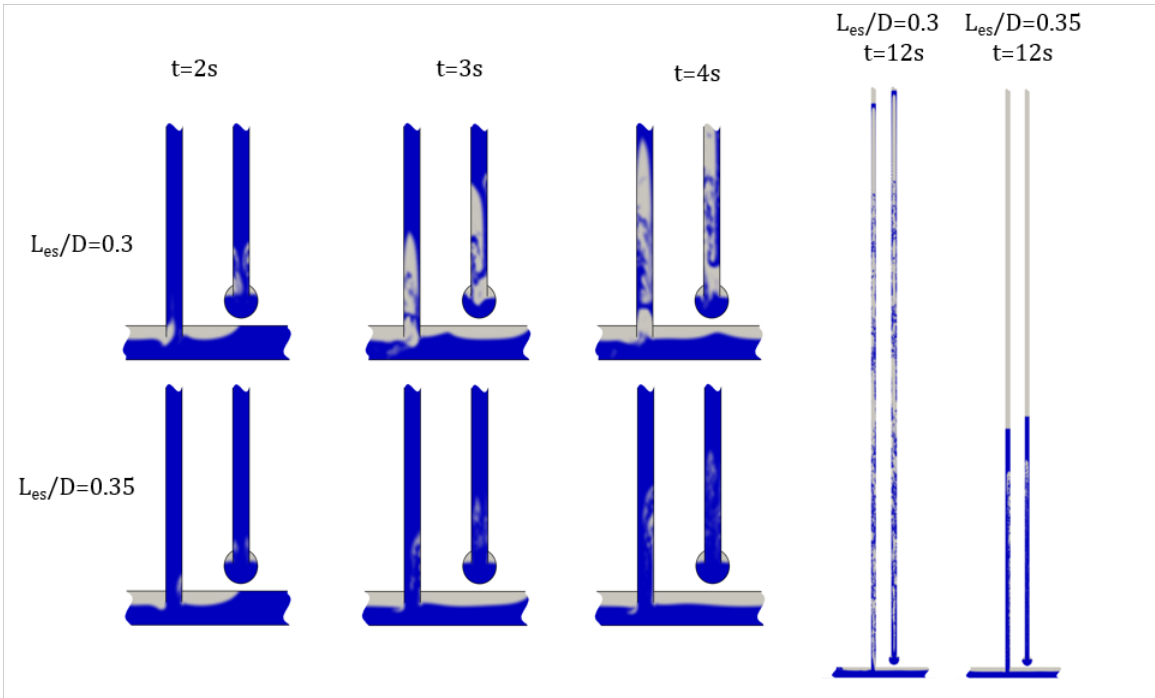

Figure 4.26: Evolution of air releasing through different L_{es}/D conditions

Figure 4.26 presented the evolution of air releasing through the shafts for cases in which the amount of captured air varied significantly. The figure presented the symmetric plane views of the air motion at different times and the cross-section views of the shaft station. It is noticed that the small difference shaft extrusion of $\Delta L_{es}/D = 0.05$ resulted in much larger air discharge into the shaft.

A comparison of the simulated pressure head results at the horizontal conduit centerline, immediately below the vertical shaft, is presented in Figure 4.27. Pressure head results were normalized by the vertical length of the shaft. With the shaft lower rim extension, the magnitude of the pressure head oscillation can be significantly reduced. Particularly when $L_{es}/D > 0.35$, the oscillation is small enough to be ignored in practical terms. Consistently with results from previous experimental investigations on the release of large air pockets, pressure head results were much smaller than the elevation of the maximum free surface during the air pocket release process.

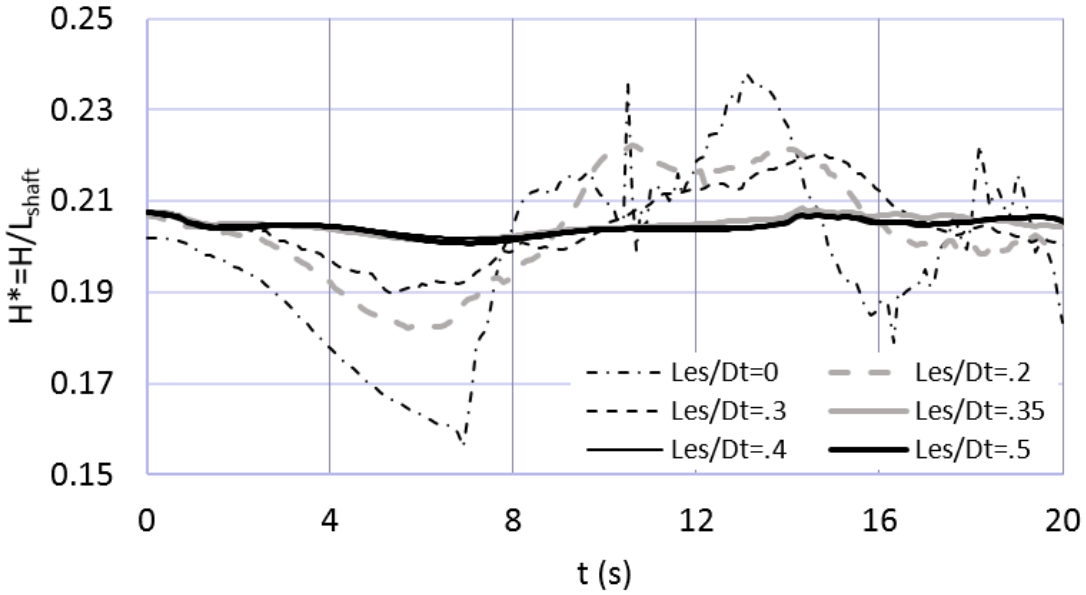

Figure 4.27: Normalized shaft bottom pressure head at the springline level

4.4 Summary of findings

This chapter focused on investigating the flow characteristics of geysering triggered by the release of air pocket through vertical shaft. Compared to most studies presented to date, a CFD model implemented using CompressibleInterFOAM was calibrated with experimental data from a larger-scale model. Then large-scale models representing a hypothetical stormwater system was simulated, considering various configurations. A retrofit strategy that can mitigate geyser was proposed and assessed as well.

The comparison between the CFD model and experimental results from Muller and Vasconcelos (2016) showed good agreement regarding the kinematics of the water and air-water interface during the air pocket release. The simulated pressures were not as accurate, however the general trend measured pressure oscillation were fairly well represented. The modeling of a hypothetical large-scale model focused on the potential displacement created by the air pocket release, thus the length of the vertical shaft was made large. The model indicated that the fraction of the original air pocket in the system that is released by the shaft increased with the shaft diameter. The displacement of the free surface also varied with D_s^*, with significant $\Delta Y_{FS}/Y_{FS,0}$ values for $D_s^* = 0.25$ and $D_s^* = 0.50$, and decreased values for smaller air pocket

volumes. The velocity of free surface motion increased with air pocket volume and smaller initial water levels in the shaft. These kinematic results of free surface maximum rise and velocity were potentially useful in the context of design of stormwater systems to avoid geysering episodes.

The calibrated CFD model was then applied to the situation where a sequence of air pockets were released. The results showed that the release of a single large air pocket could cause significant water displacement in the shaft and also created a series of continuous breakthroughs, accompanied with large magnitude of pressure oscillation. The release of a sequence of smaller air pockets was also able to generate a sequence of geyser events. It was noticed that the air pocket with wedge-shaped leading edge appeared when following previously released air pockets and this had effect on the rate of air release in the shaft. In addition, the water fluctuation and geyser intensity can be magnified by the release of a sequence of small air pockets. Since geysers were often visualized as a sequence of events (Wright et al. 2011)) similar as Scenario V5, this finding was can be representative of actual stormwater geyser events.

This chapter, in the end, evaluated the strategy of extending the lower rim of the shaft on mitigating geyser. Since air pockets occupied mostly the upper half of conduits as they propagated in stormwater systems, the goal was to prevent significant air discharge in smaller dropshafts, which could cause geysering. Rather, by creating these extensions in dropshafts, the fraction of discharged air decreased to a point in which the displacement was no longer noticed, as was indicated on the numerical simulation results presented in the present work. This portion of research was still at its early stage and investigation would be completed with more detailed CFD simulations and some experimental data collection illustrating the benefits of positive L_{es}/D. The idea was to assess to what extent such extensions could control air discharge in shafts with other D_s/D ratios, as well other air pocket volumes. Also, it is important to assess what are the impacts of such extensions in terms of energy losses in the conduits when flow was pressurized.

Our findings indicate that new designs of stormwater ventilation shafts should avoid using shaft diameters less than 50% of the tunnel diameter, and preferably 100% of tunnel diameter or more. Shafts with small dimensions can have a displacement of free surface up to 340%

of the initial water level elevation, this these adverse situations can lead to geysers. One effective method that can mitigate these operational issues is the retrofit strategy presented in current chapter, and use geometries and inflow control to reduce the air likelihood of air pocket formation.

There are significant knowledge gaps yet to be addressed in future research. For instance, the flow instability during the air slug vertical motion and expansion has not been discussed. Other modeling approaches to simulate the air release applying CFD, for instance adopting more sophisticated turbulence modeling approaches, as well more systematic study on the effects of wall roughness in the simulation results. Other interesting large scale conditions still to be simulated with CFD should include situations where there is an ”air-core” condition. This corresponds to the case described in Wright et al. (2011), when the air pocket breaks through the upper surface, but it is still present in the base of the shaft. Large pressure gradients are expected in such cases, and the intensity of geysers predicted by the CFD simulations are expected to be impacted.

The following chapter continues to present addmitional CFD research related to air-water interactions in stormwater system undergoing rapid filling conditions. The focus is on the manhole cover displacement caused by the air pressurization and water-structure impact when inertial surge and air pocket release appears in the system.

Chapter 5

Manhole Cover Displacement Created by Sudden Pressurization of Vertical Shafts during Rapid Filling of Stormwater Systems

5.1 Research objectives

In Chapter 4 a validated CFD model had been developed to describe the flow characteristics of stormwater geysering caused by air pocket releasing and then applied to understand the general trend of water displacement created by air pocket releasing through large scale stormwater shaft. Typically, physical and numerical description of these systems assume unrestricted ventilation for the shafts. However, in many conditions ventilation is limited with the absence of contact with atmosphere, except through manhole cover ventilation. When these covers limit ventilation, it is possible that air pressurization will be observed during rapid filling, and displacement of the manhole covers becomes possible.

The present chapter evaluated the likelihood of manhole cover displacement created by air water interactions in manholes, including both inertial surge and release of air pocket through vertical shafts. To achieve this objective, a systematic investigation using CFD was performed with the following goals:

- to describe air-water flow conditions associated with inertial oscillations and limited ventilation; and
- to study vertical air-water flows in shafts with restricted ventilation caused by uncontrolled air pocket release.

The follow up sections describe the methodology used in the work along with the CFD model validation, results and associated discussion based on the findings of the numerical simulation and analysis of the findings. Conclusion and recommendations for future work are also presented.

5.2 Methodology

5.2.1 CFD model approach

The CFD simulations in the present chapter were performed using compressibleInterFOAM. The starting point for the development of the present model was the validated CFD model and hypothetical large-scale CFD model presented in subsection 4.3.2. The only variation introduced in the model used to study air pocket release was to limit the ventilation at the top end of the vertical shaft, as indicated in Figure 5.1(c).

5.2.2 Validation of surging simulation with CFD model

Prior to applying CFD to determine air pressurization in manhole headspace due to inertial mass oscillations, a model validation step was required. It was decided to compare CFD model predictions with analytical solutions presented by Parmakian (1963) for surge tanks connected to closed conduits in transient flow conditions. This conditions had some similarities with inertial oscillations in dropshafts and manholes when stormwater systems were undergoing rapid filling. As is shown in Figure 5.1(a), a partially filled pipe fitted with a surge tank at the downstream end was rapidly filled by forcing a predetermined pressure at the upstream end. The analytical solutions provided by Parmakian (1963) were in terms of surge tank water level S, the average water velocity reaching the surge tank U, and period of surge oscillations T_o, as presented in equations 5.1, 5.2, and 5.3, respectively.

$$S = \frac{Q_0}{A_s}\sqrt{\frac{A_s L_P}{Ag}}\sin\left(\sqrt{\frac{Ag}{A_s L_P}}t\right) \tag{5.1}$$

$$U = \frac{Q_0}{A_s}\cos\left(\sqrt{\frac{Ag}{A_s L_P}}t\right) \tag{5.2}$$

$$T_o = 2\pi\sqrt{\frac{A_s L_P}{Ag}} \tag{5.3}$$

where Q_0 was the initial flow rate admitted in the surge tank, A_s was the cross-sectional area of the surge shaft, L_P was the pipe length, A was the cross-sectional area of the pipe, and g was the gravity acceleration.

The geometric conditions used in the validation of surge modeling had the following characteristics: the pipe diameter was 0.1 m, pipe length was 10 m with 1% slope. The surge tank located at the downstream end had a 0.2 m diameter and was 1.15 m tall. The initial water level was such that it reached 50% of the pipe diameter at the point it connected with the surge tank. At the upstream boundary condition the pressure head was fixed at a level 0.50 m above the pipe crown elevation at that location.

In parallel with the model validation, a mesh independence study was performed with the total mesh numbers of 178K, 558K and 919K for coarse, intermediate, and fine mesh sizes, respectively. As is shown in Figure 5.2, the results from the comparison between the CFD modeling results and the analytical model predictions by Parmakian were in good agreement for all mesh sizes tested. Figure 5.2 indicated that the free surface oscillation amplitude and velocity of CFD model agreed with the analytical solution very well in the first oscillation cycle. Subsequent oscillations were not well represented since the analytical solution neglects damping effects. It should also be noted that the analytical solution started from the equilibrium water level whereas the CFD solution started at the initial condition shown in Figure 5.1a. The results with the intermediate mesh size overlapped with the results of coarse mesh and fine mesh, thus this mesh size was selected for the rest of the modeling tasks involving surge oscillations.

5.2.3 Validation of air pressurization with CFD model

One of the major objectives of the current chapter was to replicate the air compression at the headspace of the vertical shaft. In order to achieve this goal, the experimental data presented by Zhou et al. (2011) was used to validate the CFD model. The experimental conditions were a 7 m initial upstream water pressure head and empty pipe at the downstream end of the horizontal pipe apparatus (Figure 5.3). The pressure was monitored near the head pipe end in the manner shown in Figure 5.3. The CFD model implemented the setup shown in Figure 5.3 except without ball valve. It is thus assumed that the opening of the valve is instantaneous rather than the valve of 0.05 to 0.1 s presented by Zhou et al. (2011).

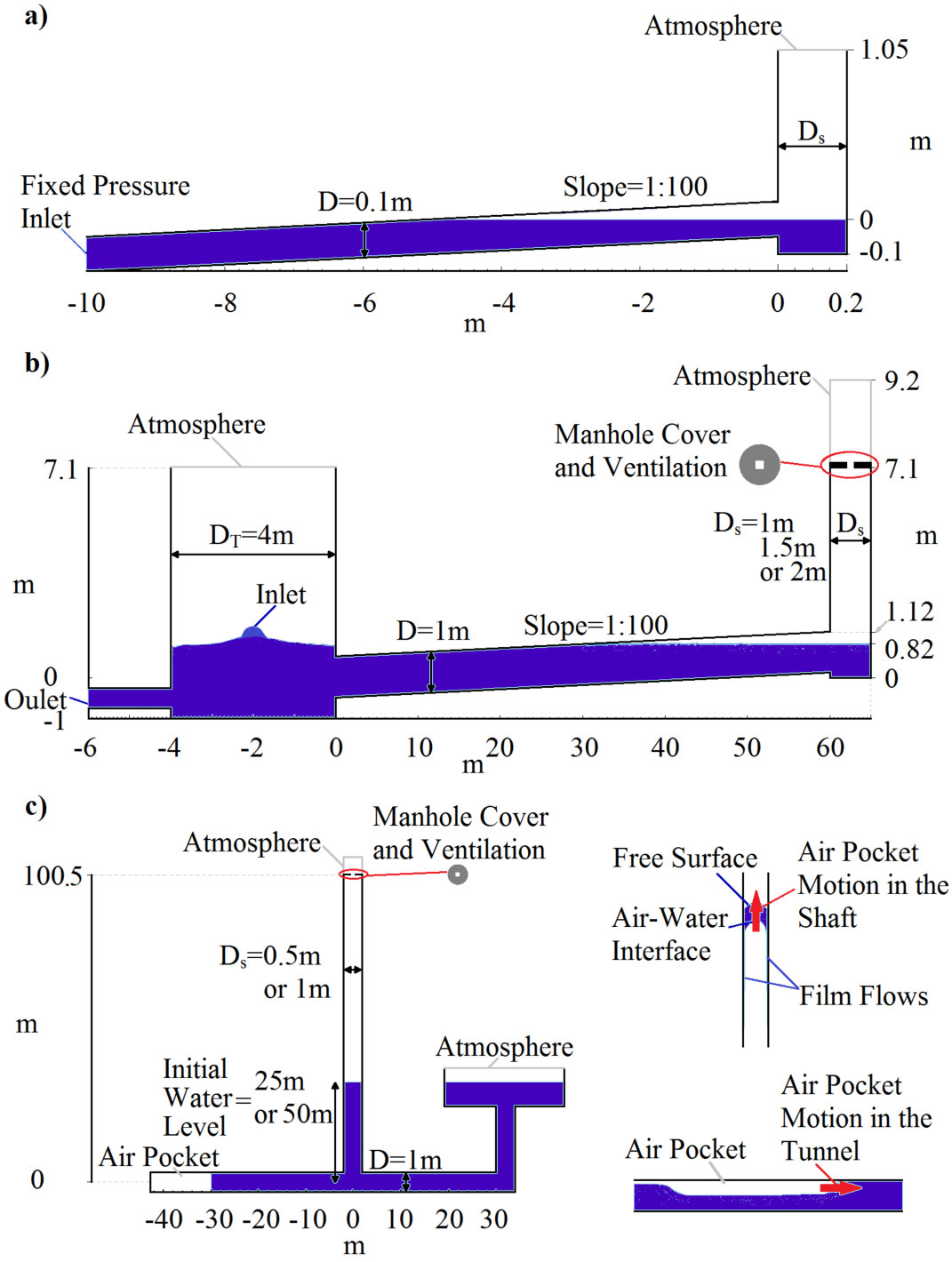

Figure 5.1: Model sketches: a) Validation Model, b) Inertial Surge Model, and c) Air Pocket Release Model

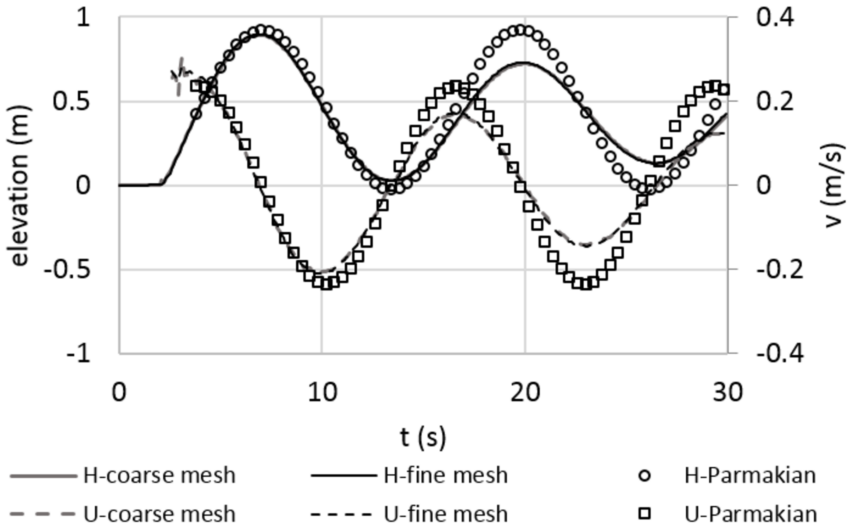

Figure 5.2: Water free surface elevation and flow velocity evolutions in Validation Model

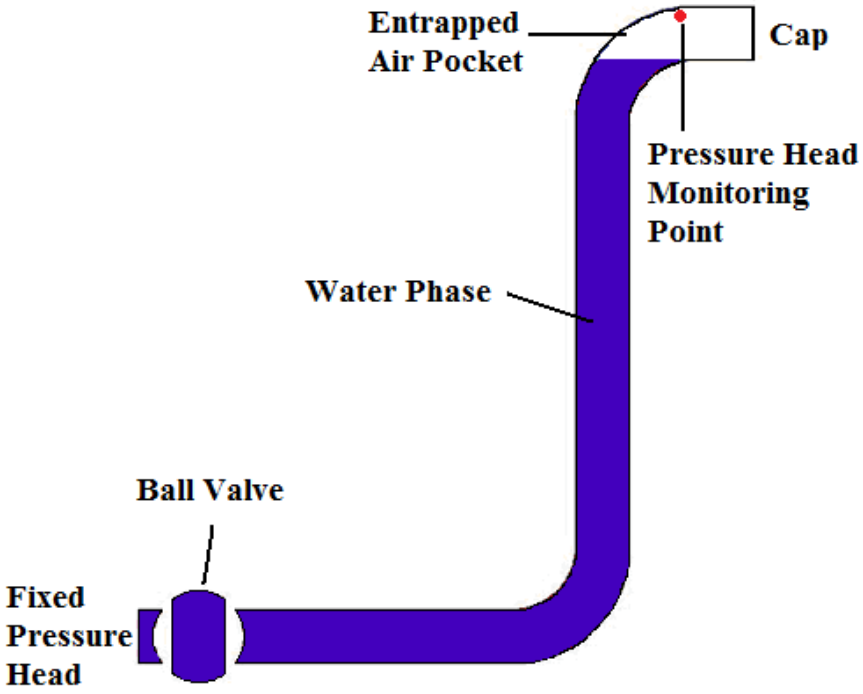

Figure 5.3: Experimental model sketch from Zhou et al. (2011) and boundary condition setups

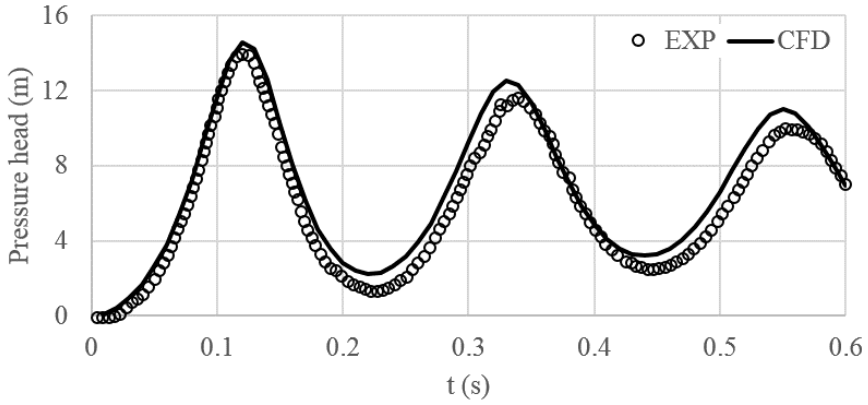

Figure 5.4: Comparison of air pressurization between 3D CFD simulation from the present work and experiments from Zhou et al. (2011)

As described in Zhou et al. (2011), the high-pressure water advanced in the pipe when the valve was opened, leading to compression of the air pocket at the end of the system. As the air was compressed, its pressure exceeded the upstream reservoir pressure, leading to a deceleration of the column and eventual reversal of the water motion back toward the supply reservoir. The pressure head of the air pocket would oscillate as it underwent such compression and expansion. Figure 5.4 showed a comparison between the CFD simulated air pressure head with the experimental data. There was good agreement, with just minor differences of pressure head and oscillation frequency.

5.2.4 Modeling details and variables used in CFD investigation

After model validation tasks were completed, systematic simulation of various rapid filling conditions was initiated in two stages. The first stage evaluated conditions of air pressurization and water impact to manhole lids. The second stage evaluated air pressurization associated with the release of large air pockets in water-filled vertical shafts. In both of these stages same ventilation conditions were used. Also it was always assumed bolted (i.e. fixed) manhole covers, in other words there was no change in ventilation area despite of pressure rise.

The CFD model aimed to study the mass oscillation in shafts with limited ventilation was performed with the presence of a downstream shaft where inflows were admitted, as shown in Figure 5.1b. This change was introduced since it was more representative of stormwater

systems than simply rapid filling of a pipe with limited ventilation as shown in Figure 5.1a. The choice of a larger dimension shaft was motivated to differentiate the natural oscillation period between the downstream and upstream shafts, and with this prevent u-tube oscillations. This group of modeling results is referred herein as *Inertial Surge Model*.

This geometric model contained a 4 m diameter downstream tank with height of 8.1 m, which was fully-ventilated, and fitted with an outflow port. This downstream tank was connected to an upstream vertical shaft through a 60 m long tunnel, with a diameter D equal to 1.0 m and with 1% slope. Different values for the upstream surge shaft diameter D_s were considered in the study: 1.0 m, 1.5 m and 2.0 m. The location of the ventilation orifice within the manhole cover of the upstream shaft matched the overflow elevation of the downstream tank. This geometric configuration was similar to the one used in the inertial oscillation validation model, with differences in the scale, the presence of the downstream tank and ventilation restrictions.

A fixed inflow rate was admitted in the tank at a normalized fixed rate equal to $0.5\sqrt{gD^5}$. This created a backwater in the tunnel linking the shafts. The resulting depth in the tunnel as it connected with the upstream shaft was 0.82 m. While the inflow was unchanged, the outflow port at the downstream tank was closed to emulate the arrival of a flow pressurization front in the system. This flow closure created the back-up of the inflows into the tunnel, which in turn led to surging in the upstream shaft. Taking the plan area of the upstream shaft A_s as a reference, six ventilation areas A_v in the manhole cover were considered: A_v equal to 0%, 1%, 2%, 5%, 10% and 100% of A_s. Ventilation areas were normalized by the plan area of the upstream shaft $A_v^* = A_v/A_s = A_v/(0.25\pi D_s^2)$. The first and last conditions were the extremes of zero ventilation and fully ventilated conditions. The initial temperature in the system assumed in the model was set as 27^oC. In the simulations was it assumed that the manhole cover was fixed and would not move.

The second stage of the investigation on manhole cover displacement corresponded to conditions related to the uncontrolled release of entrapped air pockets, illustrated in Figure 5.1(c), and was referred to as *Air Pocket Release Model*. The model in essence corresponded to the CFD model presented in Chapter 4 with restriction in ventilation. These series of simulations

Table 5.1: Range of numerical variables considered in the CFD simulations of Inertial Surge Model and Air Pocket Release Model

Variable	Inertial surge	Air pocket release	
Water level in vertical shaft (m)	25.0	25.0	50.0
Shaft diameter D_s (m)	1.0, 1.5, 2.0	0.5, 1.0	0.5
Normalized ventilation area A_v^*	0.00, 0.01, 0.02, 0.05, 0.10 and 1.00		
CFD model mesh numbers	539k to 1,188k	1,122k to 2,332k	1,375k to 2,248 k

considered two different shaft diameters $D_s = 0.5$ m and 1.0 m, six different ventilation areas A_v^*, and different initial water levels (either 25 m or 50 m) in the shaft where air escaped. A 1 m diameter, 72.7 m long tunnel was used in the system , with the initial 12.7 m length comprised of the air phase (equal to 10 m^3) that was released in the beginning of the the simulation. The total length of the vertical shaft was 100 m, and it was located 30 m away from the location where the air pocket was released. This distance was sufficient to allow the pocket to fully develop in a discrete gravity current, as illustrated in Baines (1991) and Chosie et al. (2014). At the opposite end of the solution domain a reservoir was placed to sustain pressure while the air pocket was released. A summary of all tested variables was presented in Table 5.1, and in all 36 different conditions were simulated between the two stages of CFD investigations.

5.3 Results and Discussion

The Inertial Surge Model results included water and air pressure results as a function of time, ventilation area or changes in the water flow rate as the water level interface reached the manhole cover. These results are presented in Figure 5.5 through Figure 5.10. Results associated with the Air Pocket Release Model on the other hand are presented in Figure 5.13 through Figure 5.15.

To create some means for comparison and help in the analysis of the pressure results obtained in these simulations, there was a need to consider a manhole cover with an specified size and weight. Clearly there was a wide range of manhole cover commercially available, so it was decided to assume an hypothetical manhole cover to be used in the analysis. This manhole cover had a mass of 50-kg, weight of 490 N, diameter of 0.50 m and plan area of 0.196 m^2. Thus, when gauge pressures underneath the manhole cover reached 2,495 Pa (or 0.25 m of

pressure head) the weight of the manhole cover would be overcome by this pressure and there would be the possibility of manhole displacement if this was not bolted, which was the case considered in the present simulations.

5.3.1 Inertial Surge Model results

Figure 5.5 presented the water pressure head variation predicted at the bottom of the shaft for Scenario $D_s/D = 1$. The water pressure head prior to reaching the manhole cover elevation (referred to as MHCE) can be represented into two components, a steady rising component and a sinusoidal type oscillation component. The former is attributed to the overall filling process of the system. The latter is attributed to a surging process under ventilated conditions ($A_v^* \geq 0.01$). The observed period of $15.6s$ of the surges modeled with CFD is well in agreement with the 15.5 s value that results from using equation 5.3. In contrast, the pressure head of the condition without ventilation ($A_v^* = 0$) evolved significantly different from others, with a steadier growth, much smaller pressure oscillation amplitudes with a smaller oscillation period of 9 seconds. This period was smaller than the oscillation period that was estimated for a hydro-pneumatic chamber, presented in equation 5.4:

$$T_h = 2\pi\sqrt{\frac{\forall\, L}{H^* g A}} \tag{5.4}$$

where $\forall$ was the air volume in the air chamber, L was the tunnel length, H^* was the initial air pressure head in the chamber, and A was the tunnel cross-sectional area. During the process of air pressurization in the upstream shaft with no ventilation, the cycles of compression and expansion of the air in the no-ventilation scenario were complex. Water level reached a minimum that created cyclical intrusions of air in the near-horizontal tunnel. This could explain the discrepancy between the hydro-pneumatic chamber period and the modeled pressure oscillation period, however this still needed further investigation.

Figure 5.5 indicated that eventually water pressure head reached the manhole cover elevation, and subsequently water surface impacted the manhole cover causing pressure spikes. The elimination of air within the shaft due to the rising of the water free surface was associated to

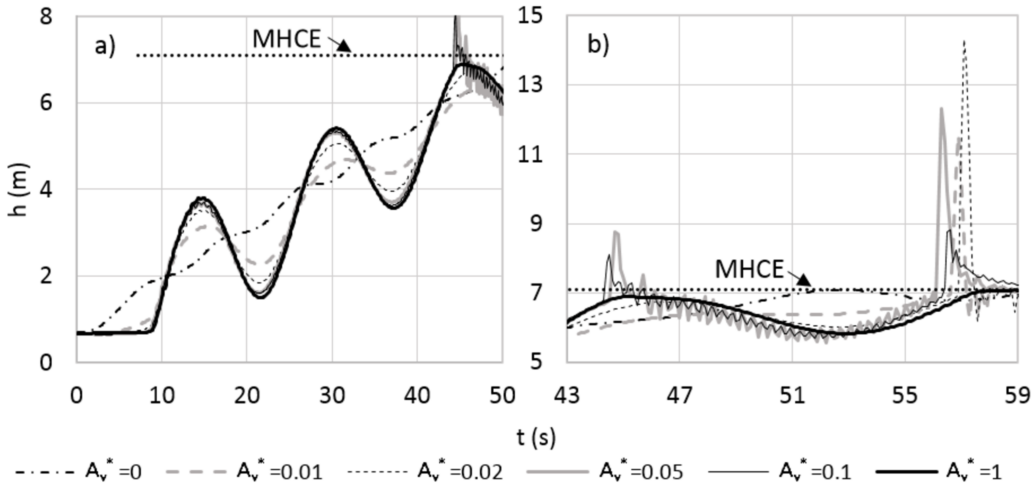

Figure 5.5: Water pressure head evolution at the bottom of the shaft ($D_s/D = 1$) a) filling process, and b) details when water free surface approaching the manhole cover elevation (MHCE)

air pressurization, referred to as h_a. Smaller ventilation areas ($A_v^* = 0.01$ and 0.02) created an air cushioning effect that in general decreased the water level rising velocity. Eventually all air was eliminated in a situation analogous to the collapse of an pocket near an air valve during the priming of a water main. The pressure spikes observed as the air phase underneath the manhole cover collapsed were related to near-instantaneous changes in water flow rates across following the air collapse, as is further discussed ahead. It was very important to note that these CFD results were highly dependent on geometric characteristics and inflow rate, and was difficult to extrapolate the results presented here to other conditions. Results for the cases D_s=1.5 m and 2 m followed the same trend, albeit with a more gradual rate of pressure rise, and were not presented here for brevity.

Figure 5.6 presented the variation of air pressure head (gage) h_a predicted at a location immediately below the manhole cover up to the moment when the air phase collapsed for conditions when $D_s/D = 1$ and 2. The secondary vertical axis was used only for the zero ventilation case ($A_v^* = 0$). It was intuitive to notice that higher air pressures were associated with smaller shaft diameter and ventilation areas. It is also interesting to notice that the first pressure oscillation peak was consistently larger than subsequent ones.

The relationship between ventilation area A_v^* and peak air pressure head was presented in Figure 5.7, and as it would be anticipated peak h_a^* ($= h_a/D_s$) were associated with smaller A_v^*.

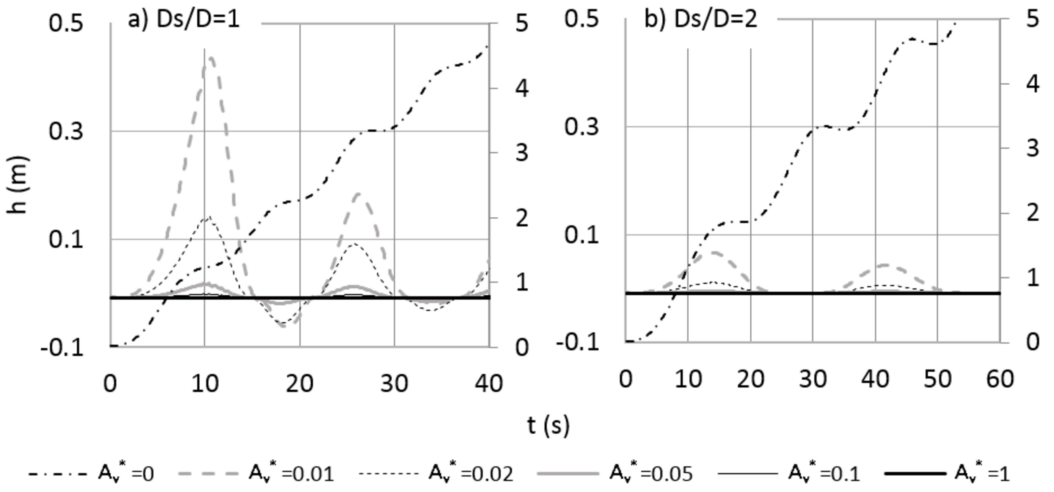

Figure 5.6: Air pressure head evolution at the lower surface of the manhole cover prior to the air pocket collapse (Inertial Surge Model) a) $D_s/D = 1$ and b) $D_s/D = 2$. The secondary axis was used only for results where $A_v^* = 0$.

However, the diameter of the vertical shaft also had an impact in the solution, since surging effects were more pronounced as D_s/D values decreased. It is noticed that the results with $D_s/D = 1$ were consistently larger than other vertical shaft diameters. Figure 5.7 presents the threshold pressure needed to overcome the weight of the hypothetical manhole cover, represented in the legend as *MHC motion*. It can also be noticed that only when $D_s/D = 1$ and $A_v^* \leq 0.01$ the peak air pressure exceeded the threshold for motion of manhole covers. These results suggest that air pressure associated with inertial oscillations is not a likely cause for manhole cover displacement episodes.

When air was completely evacuated through the ventilation water phase reached the manhole cover and created pressure spikes, referred to as h_{pc} linked to the collapse of the air phase. These spikes were predicted by the CFD model, as is shown in Figure 5.8, with results for $D_s/D = 1.5$ omitted for brevity. In a first inspection it was noticed that h_{pc} values were much larger than the values associated with air pressurization. As is pointed in Table 5.2, for all cases in which the water reached the manhole cover, the peak pressures are large enough to result in a manhole cover displacement. *A priori*, it appeared that there was no strong relationship between water pressure results and both A_v^* and D_s/D. Peak h_{pc} values (normalized by shaft diameter D_s) for all D_s/D cases are presented in Figure 5.9 in terms of A_v^*. It was noticed that h_{pc}^* in general decreased with larger A_v^*, however some results appeared counterintuitive. For

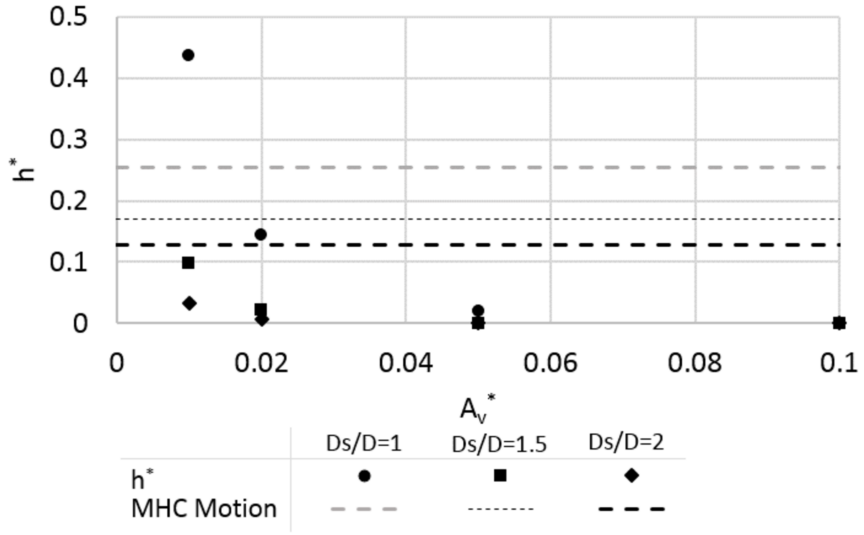

Figure 5.7: Normalized maximum air pressure head (h^*) vs. normalized ventilation area (Inertial Surge Model)

instance, peak h^*_{pc} values for $D_s/D = 1.5$ exceeded the ones simulated for $D_s/D = 1.0$ when $A^*_v \leq 0.02$ and there was a increase in peak as A^*_v increased from 0.01 to 0.02 for $D_s/D = 1.0$ case.

These results could be better understood with the aid of Joukowsky equation (Wylie et al. 1993), since peak h^*_{pc} should increase with the change in upward water inflow rate ΔQ associated to the impact of the rising water level and its impact on the ventilation orifice. Prior to reaching the ventilation, two factors influence the upward water velocity and flow rate: 1) air pressurization and cushioning effect; and 2) surging, which continually created changes in the velocity as indicated in Figures 5.2 and 5.5. After water reached orifice elevation the ventilation size would obviously be an important variable restricting water outflow. The relationship between h^*_{pc} and ΔQ (normalized by $\sqrt{gD_s^5}$) was presented in Figure 5.10, and it could be noticed that for a given value of D_s the normalized values of h_{pc} increased with ΔQ^*. As pointed, all values of h_{pc} exceeded the threshold to create a manhole cover displacement. These results suggested that the impact of water under a manhole cover could be a common cause for manhole cover displacement for stormwater systems undergoing rapid filling.

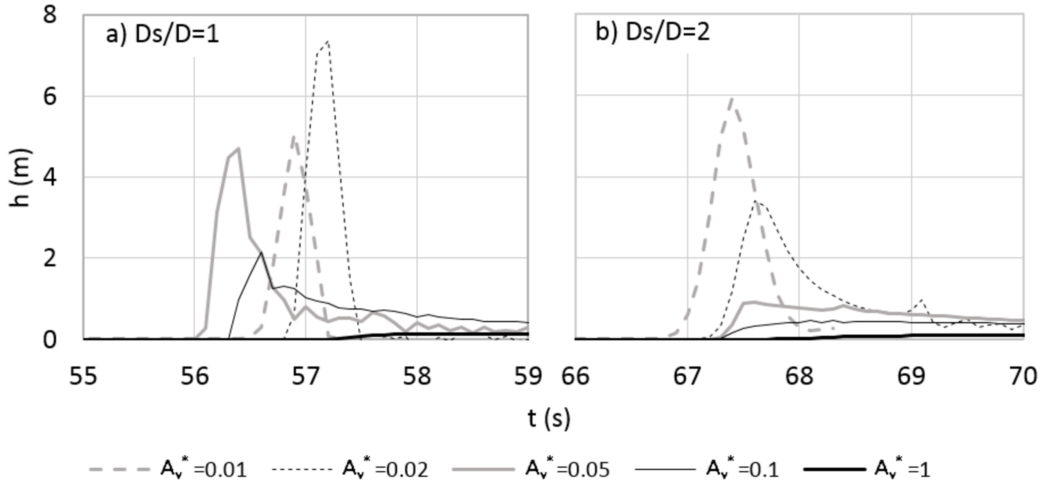

Figure 5.8: Pressure head evolution on the lower surface of manhole cover with air pocket collapse (Inertial Surge Model) a) $D_s/D = 1$ and b) $D_s/D = 2$

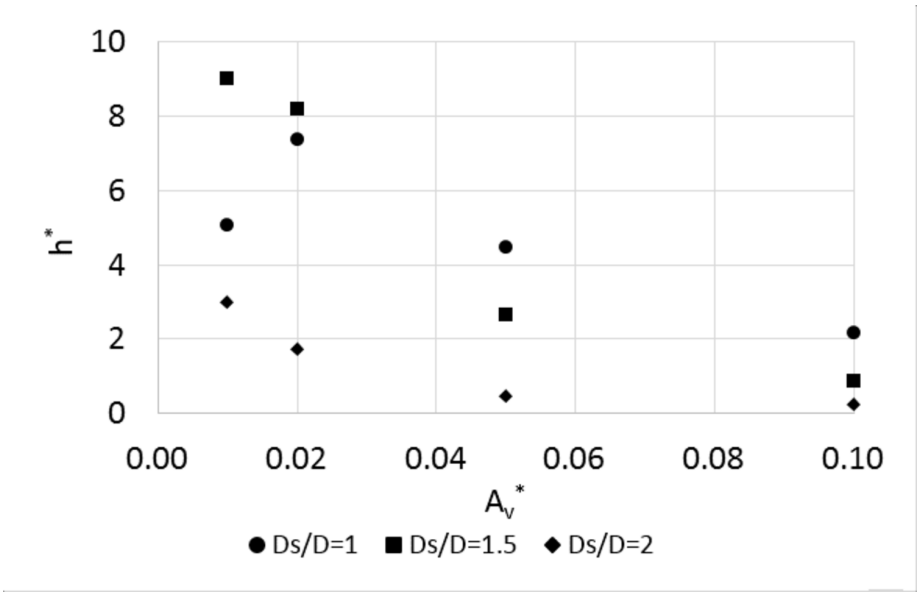

Figure 5.9: Normalized pressure spikes (h^*) vs. normalized ventilation area (Inertial Surge Model)

Table 5.2: Maximum air pressure heads and pressure spikes at the lower surface of the manhole cover (Inertial Surge Model)

Scenario	$h_a, h_{pc}(m)$		
	$D_s/D = 1$	$D_s/D = 1.5$	$D_s/D = 2$
$A_v^* = 0.01$	$0.44, 5.07$	$0.15, 13.57$	$0.07, 5.93$
$A_v^* = 0.02$	$0.14, 7.37$	$0.03, 12.26$	$0.01, 3.41$
$A_v^* = 0.05$	$0.02, 4.48$	$< 0.01, 3.96$	$< 0.01, 0.91$
$A_v^* = 0.1$	$< 0.01, 2.16$	$< 0.01, 1.29$	$< 0.01, 0.48$

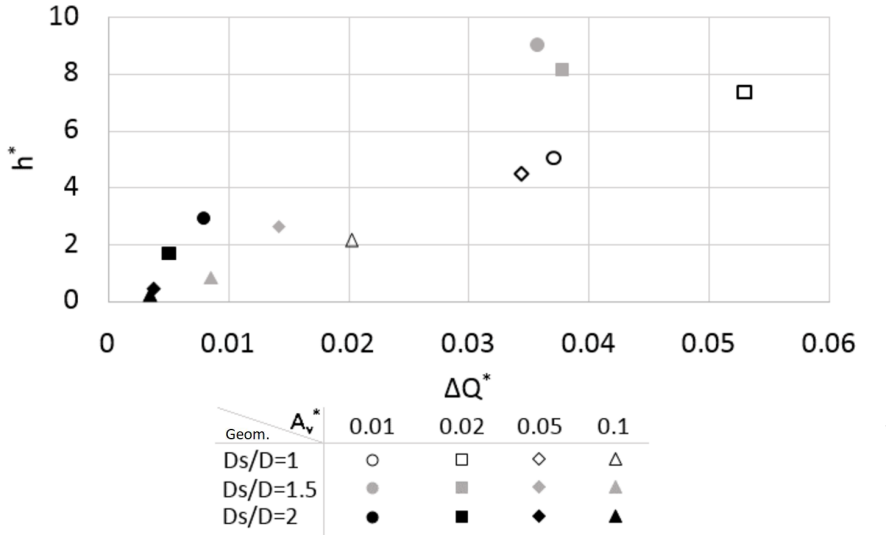

Figure 5.10: Normalized pressure spikes (h^*) vs. normalized difference of water rising flow rate (ΔQ^*) in the shaft prior to and after the air pocket collapse (Inertial Surge Model)

5.3.2 Air Pocket Release Model results

The process of manhole cover displacement associated with the uncontrolled release of entrapped air pockets was a complex process. The release of a large air pocket through a vertical shaft led to a process of compression and expansion of the rising pocket, downward water flow through film, water refilling at the bottom of the shaft, and the compression of air phase at the manhole headspace. As was indicated in Chapter 4, air release created fast vertical velocities in the water present in vertical shafts. Under limited ventilation condition, this could lead to more severe air pressurization and more severe impact of water phase against manhole cover when compared to the Inertial Surge Model. As pointed earlier, in all cases a pocket volume of 10 m^3 was released in the system.

Figure 5.11 and 5.12 showed the displacement and velocity of the water free surface in the shaft, respectively. As is shown in Figure 5.11, with higher air phase pressure levels the trajectory of the displaced water column was decreased, which points to an air cushioning effect. When $A_v^* = 1$ the free surface displacement was around 70 m, but for the case of $A_v^* = 0$ this displacement was only 30 m. There was a gradual variation in this displacement among all tested values of A_v^*. It would also be anticipated that the air cushioning effect would affect the velocity of the free surface of the water as it moved toward the manhole cover. The peak

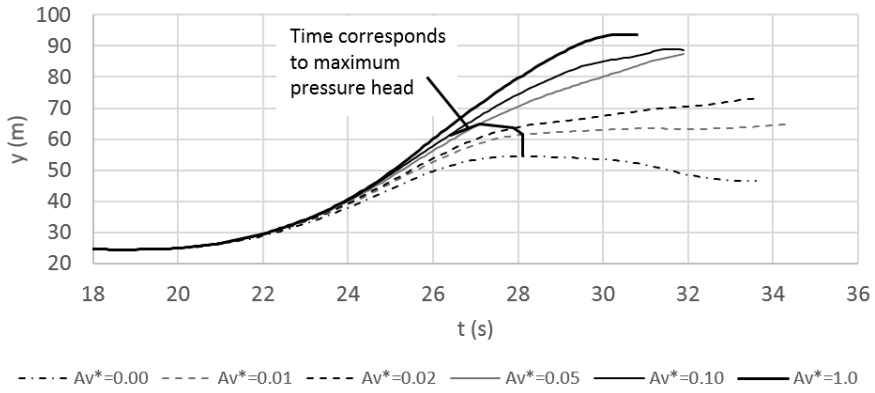

Figure 5.11: Displacement of the water-free surface in the shaft created by the rising air pocket ($W = 25m$)

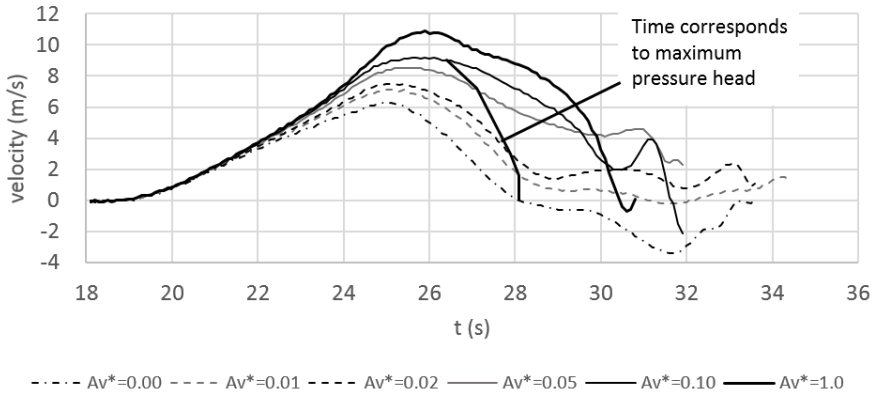

Figure 5.12: Change in the free surface velocity within the manhole for various A_v^* values ($W = 25m$)

velocity simulated for the conditions where $A_v^* = 0$ and $A_v^* = 1$ were 6.0 m/s and 10.9 m/s, respectively. In general, the velocity values grew for about 7s to 8s during the initial air pocket rise and decreased abruptly, as shown in Figure 5.12. Peak velocity times did not coincide with the time where pressure peaked. It was also noticed that the maximum air pressure occurred before the breakthrough of the rising air pocket at the top of the water column, and the peak velocity times did not coincide with the time where pressure peaked.

Air pressure results are presented in Figure 5.13 for both $D_s/D = 0.5$ and 1 cases and when $W = 25m$. There were three main characteristics of these results to be pointed out. First, the magnitude of the values of pressure were much larger than the conditions associated with the Inertial Surge Model tests. The second point was that peak pressure values decreased with larger A_v^* values, as it would be anticipated. Such drop was also expressed in terms of peak

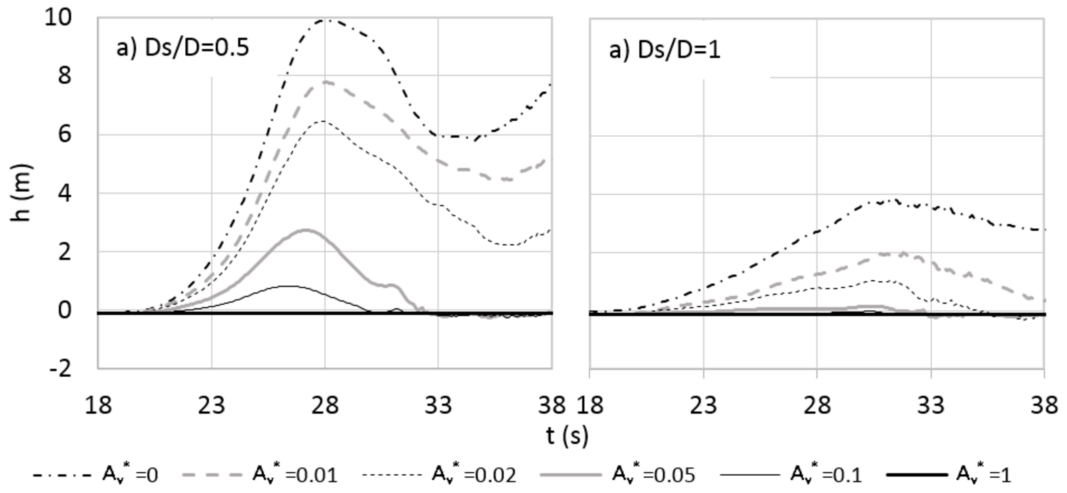

Figure 5.13: Pressure head evolution on the lower surface of manhole cover (Air Pocket Release Model) $W = 25m$, a) $D_s/D = 0.5$ and b) $D_s/D = 1$

Table 5.3: Maximum air pressure heads (m) at the lower surface of the manhole cover (Air Pocket Release Model, $W = 25m$)

Scenario	$D_s/D = 0.5$	$D_s/D = 1$
$A_v^* = 0$	9.91	3.85
$A_v^* = 0.01$	7.77	2.03
$A_v^* = 0.02$	6.44	1.05
$A_v^* = 0.05$	2.72	0.16
$A_v^* = 0.1$	0.81	< 0.01

h_a^* in terms of A_v^* in Figure 5.14. Finally, larger D_s/D had a major effect in decreasing the magnitude of the air pressure, as the upward velocity of the air pockets were decreased, a result that was consistent to the observations in Chapter 4. In most cases sudden air pocket releases led to values of pressure that were sufficient to create manhole cover displacement, as is shown in Table 5.3.

This point is relevant, since current research on uncontrolled release of air pockets had been focusing mostly on geysering events. There are many open questions related to needed research to characteristics of geysers. However, the results presented here indicated that even if the water level during an air pocket release did not reach grade level, the air pressurization associated with uncontrolled air pocket release could still displace manhole covers. On the other hand, if such covers were bolted to the manhole structure, care must be taken in ensuring

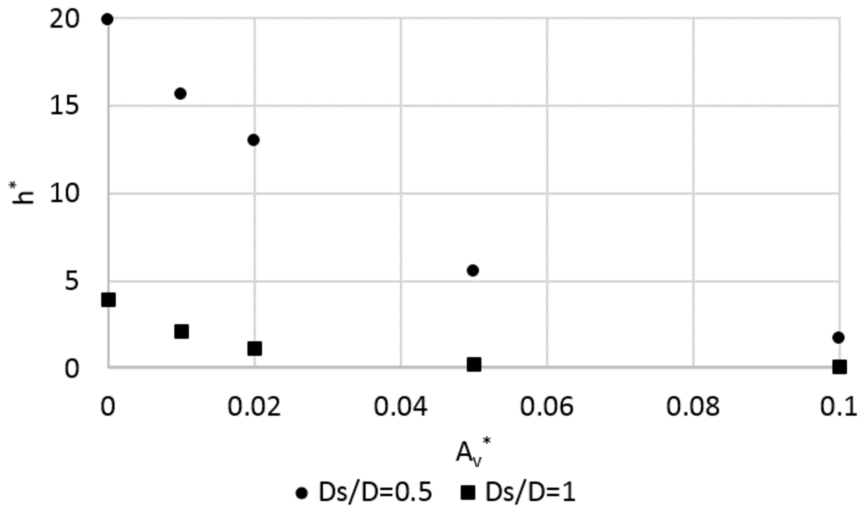

Figure 5.14: Normalized maximum air pressure head vs. normalized ventilation area (Air Pocket Release Model, $W = 25m$)

that the structure is ready to absorb the forces associated with the air pressurization so that structural damage, as reported by Klaver et al. (2016), can be avoided.

One condition in which larger water depth in the vertical shaft ($W = 50m$) prior to the air pocket release was studied, and there was an indication that air pressurization was generally worsened, as is shown in Figure 5.15. Peak pressures were increased for the three smallest ventilation conditions ($A_v^* \leq 0.02$). Also, for the cases when ventilation was positive, water level increased sufficiently to the point where the rising water mass collided with the ventilation orifice, leading to geysering. While this was similar to the conditions observed in the Inertial Surge Model, the flow rate prior to the impact was higher and resulting pressure forces were much more significant. The overall pressure evolution near the ventilation orifice, characterized by slight air pressure oscillations followed by a waterhammer-like pressure was consistent to the Type 2 behavior reported in Zhou et al. (2002) and Zhou et al. (2004) for $A_v^* = 0.01$ and 0.02. There was minimum air cushioning for $A_v^* = 0.05$ and 0.10, also consistent with Type 3 behavior in Zhou et al. observations. No ventilation condition used in the present work yielded conditions that are analogous to Type 1 orifice presented by Zhou et al.

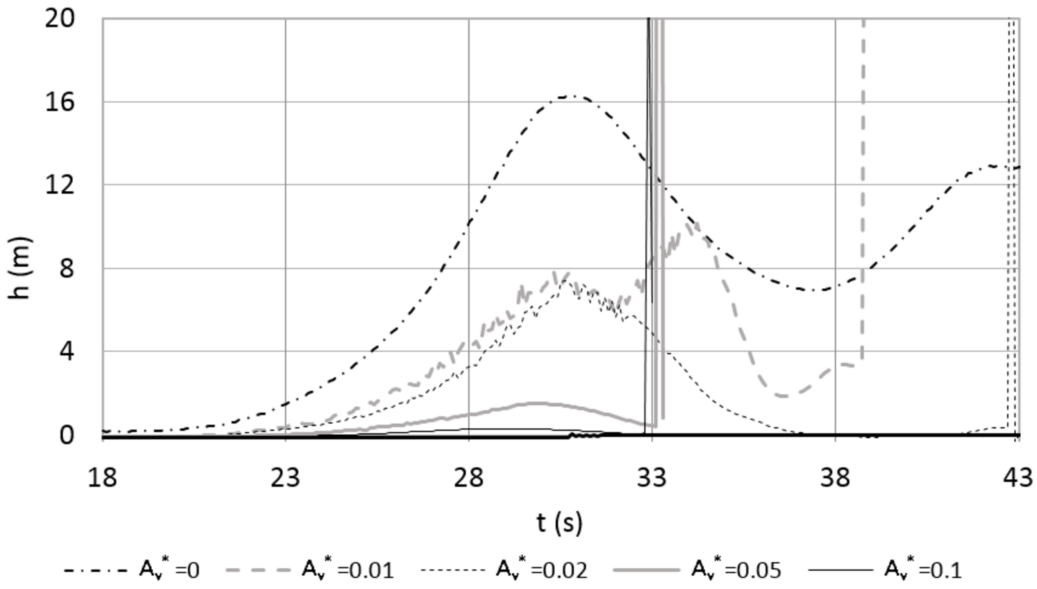

Figure 5.15: Pressure head evolution at the lower surface of manhole cover (Air Pocket Release Model, $D_s/D = 0.5$, $W = 50m$)

5.4 Summary and future work

The present work presented an investigation on the likelihood of manhole cover displacement caused by either the pressurized air at the vertical shaft headspace or water impact when stormwater system was undergoing rapid filling. There are two mechanisms that can lead to such operational issues, i.e. inertial surge and air pocket release through vertical shaft. Though many observations have shown such occurrences, the understanding of the magnitude of the air pressurization and the instantaneous water impact pressure, and the likelihood of the manhole cover displacement is still very limited. The key contribution of the present work is to fill this knowledge gap and discuss the similarities and differences of the two mechanisms that may lead to manhole cover displacement.

The key findings associated with sudden pressurization in vertical shafts associated with inertial surges are:

- Rapid filling of stormwater system could lead to inertial surge in vertical shaft. When the ventilation was limited, free surface oscillation could lead to air pressurization at the headspace in the shaft. Intuitively, the peak air pressure values decreased with larger

ventilation, e.g. the peak air pressure values decreased by more than 95% when A_v^* was increased from 0.01 to 0.05 and $D_s/D = 1$;

- Air pressurization triggered by inertial water surging can overcome the weight of a manhole cover when a combination of smaller vertical shaft diameter and restricted ventilation exist. Otherwise, research results indicated that air pressurization associated with inertial surge is not a common cause for manhole cover displacement;

- Direct impact from water during inertial surge could lead to very large instantaneous peak pressure, which was more likely to cause manhole cover displacement. The magnitude of peak pressure was well correlated with variation of upward water inflow rate created by smaller flow area of the ventilation orifice. This is consistent with the Joukowsky equation.

The key findings associated with sudden pressurization in water-filled shafts undergoing uncontrolled air pocket release are:

- The magnitude of air pressurization associated with air pocket release through vertical shafts was at least 4.6 times more than that associated with inertial surge under the tested conditions, and was capable to cause manhole cover displacement in most cases considered in the present study;

- The peak air pressure values also decreased with larger ventilation, e.g. it decreased by 92% when A_v^* was increased from 0.01 to 0.05 and $D_s/D = 1$. Larger D_s/D had a major effect in decreasing the magnitude of the air pressure as anticipated, leading to at least 74% of decrease when D_s/D was increased from 0.5 to 1 and $A_v^* > 0.01$;

- Higher initial standing water level in the vertical shaft prior to the air pocket release would worsen the air pressurization issues, including both higher magnitude of air pressurization and possible direct water impact with the manhole cover;

- With higher initial standing water level, the overall pressure evolution near the ventilation point can lead to all the three types of air pressure patterns presented by Zhou et al. (2002);

- Overall, this mechanism for air pressurization is more likely to cause manhole cover displacement and structural damage.

A practical recommendation from this work is to use, whenever possible, vertical shafts with plan areas at least as large as the tunnels and sewers cross sectional area. Also, adopt when possible ventilation in manholes at least equal to 10% of the vertical shaft plan area. If ventilation in manhole covers is not possible due to odors issues, they may be bolted to the manhole or shaft as long the efforts associated with air compression are properly considered in manhole/shaft design.

Though the conclusions are generic, it should be reiterated that the simulation results are also highly dependent to the specific geometry and flow conditions. More research is needed to understand the processes associated with sudden air pressurization in vertical shafts and manholes. More geometries, initial conditions and inflow scenarios still need to be considered. Currently there is not enough design guidelines to avoid this type of events, and with more intense rain events becoming more common this need will become even more clear. Further CFD simulation, particularly when the water reaches and impacts manhole covers is still needed, and possibly even in conditions where the mesh is dynamic to reflect temporary opening of manhole covers when pressure builds up underneath. It is intended to pursue these themes in further studies.

So far, several CFD models have been developed and the research results indicate the compressible two-phase flow CFD models is capable to describe the pressurized transient air-water flows in stormwater system. The following two chapters present both CFD and experimental research on another type of stormwater management application, sediment basins on construction side. The settling processes in sediment basins is presented first and followed with resuspension of soil particles.

Chapter 6

Settling Processes in Sediment Basins Undergoing Filling and Emptying Processes

6.1 Research objectives

The present chapter describes the experimental and numerical research on soil-water flow characterization in sediment basins during filling and dewatering processes. The performance of these basins can be evaluated in terms of the ability of retaining sediments while performing controlled dewatering. There are two major objectives in this chapter:

- To test the efficiency of various sediment basin configurations on reducing water turbidity;
- To develop a CFD model that is able to describe flows in sediment basins, including porous baffle effects.

To accomplish the above objectives, three tasks were conducted in this study:

- Experimental characterization of turbidity values and particle size characterization in sediment basins during filling events;
- Experimental tests with the treatment of the skimmer discharge with a SSHRS and PAM; and
- CFD characterization of flows within sediment basins of various basin aspect ratios with and without porous baffles.

The subsequent sections describe the methodology used in these studies, along with results and discussion of the findings. Summary and future work is presented in the chapter end.

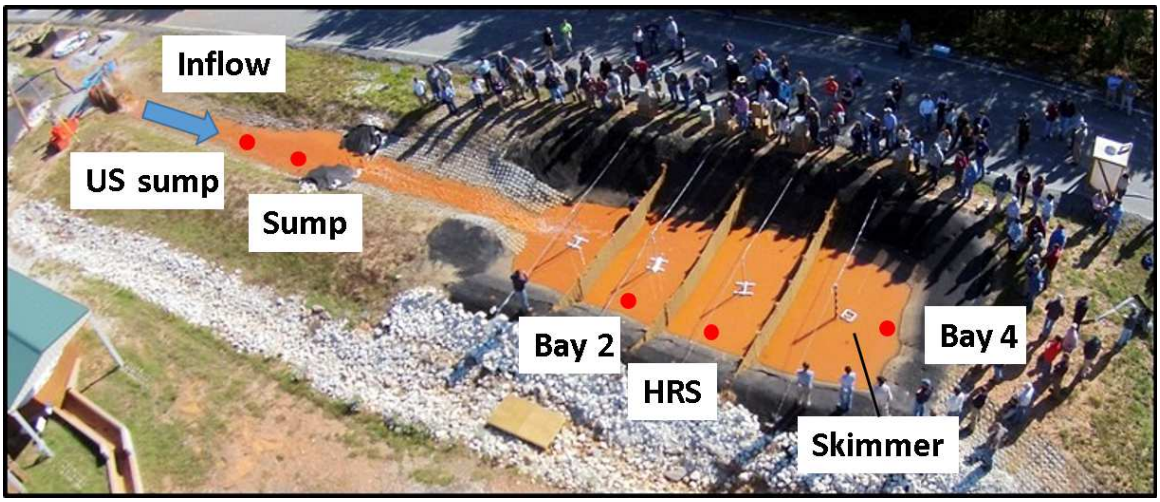

Figure 6.1: Aerial view of the sediment basin facility (Perez et al. 2016).

6.2 Methodology

6.2.1 Experimental methodology

Studies were conducted in the Auburn University-Erosion and Sediment Control Testing Facility (AU-ESCTF) to characterize the variation of turbidity values during basin filling events. Such studies were conducted in parallel to the investigation reported in Perez et al. (2016) that aimed to 1) create a methodology for the testing of a large-scale sediment basin; 2) study changes in surface turbidity selected locations in the basin; and 3) study the sediment mass balance after a sequence of tests. An aerial view of the sediment basin used by Perez et al. (2016) and this investigation is presented in Figure 6.1, in which the sampled points were denoted for the data in Figure 6.10.

The present investigation sampled water at three different depths (1 ft, 2 ft and 3 ft from the basin invert), and at each of the four bays in the basin. The vertical location within the bays where samples were taken corresponded to the same points that were selected in Perez et al. (2016) study. Samples from twelve points in the basin were siphoned out and collected with an array of 3/8 inch clear tubing. Flow in these tubes was initiated by means of a vacuum pump once the water level was large enough in the basin to sustain the siphoning. Samples were taken from these 12 locations approximately every 5 minutes, and stored in plastic bottles for subsequent turbidity evaluation. Unlike Perez et al. (2016) study, turbidity was not characterized

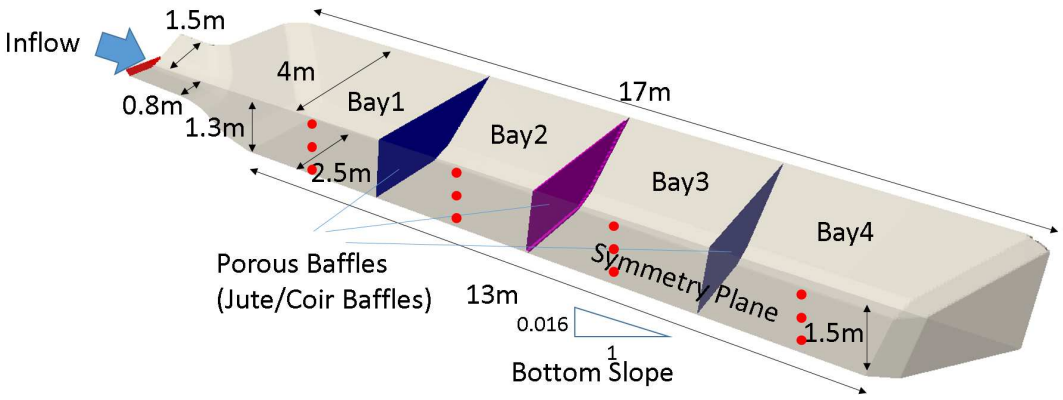

Figure 6.2: Schematic of the sediment basin used in this study. Red dots corresponded to the location where samples were taken.

with the aid of turbidity probes, but with a HACH 2100Q turbidimeter. The sampling points are the red dots in the schematic representation of the sediment basin presented in Figure 6.2.

These samples were collected for each of the three repetitions associated with the tests, with the goal of evaluating how the sequence of sediment loading in the basin impacts the turbidity over time. These tests were also conducted over all the configurations that were tested by Perez et al. (2016), which were based on the original standard ALDOT sediment basin design, as presented in Figure 6.3:

- Configuration 1: Original basin design;
- Configuration 2: Original design with a denser jute/coir porous baffle, of which the percent open area was 10.9% compared to the original 21.7% (Perez, 2016), separating the 1^{st} and 2^{nd} bays, also referred to as improved baffle configuration;
- Configuration 3: Original design with a high-rate settler (HRS) installed within the 3^{rd} bay, creating upward flow configuration, referred to as HRS upward; and
- Configuration 4: Original design with a HRS installed within the 3^{rd} bay, creating a longitudinal flow configuration and referred to as HRS longitudinal.

The deployment of HRS in configurations 3 and 4 were represented in Figure 6.4, and it may be noticed that the settlers occupied most of the space available in Bay 3. As a result, in these configurations samples were collected only at Bays 1, 2, and 4, for a total of 9 points. The

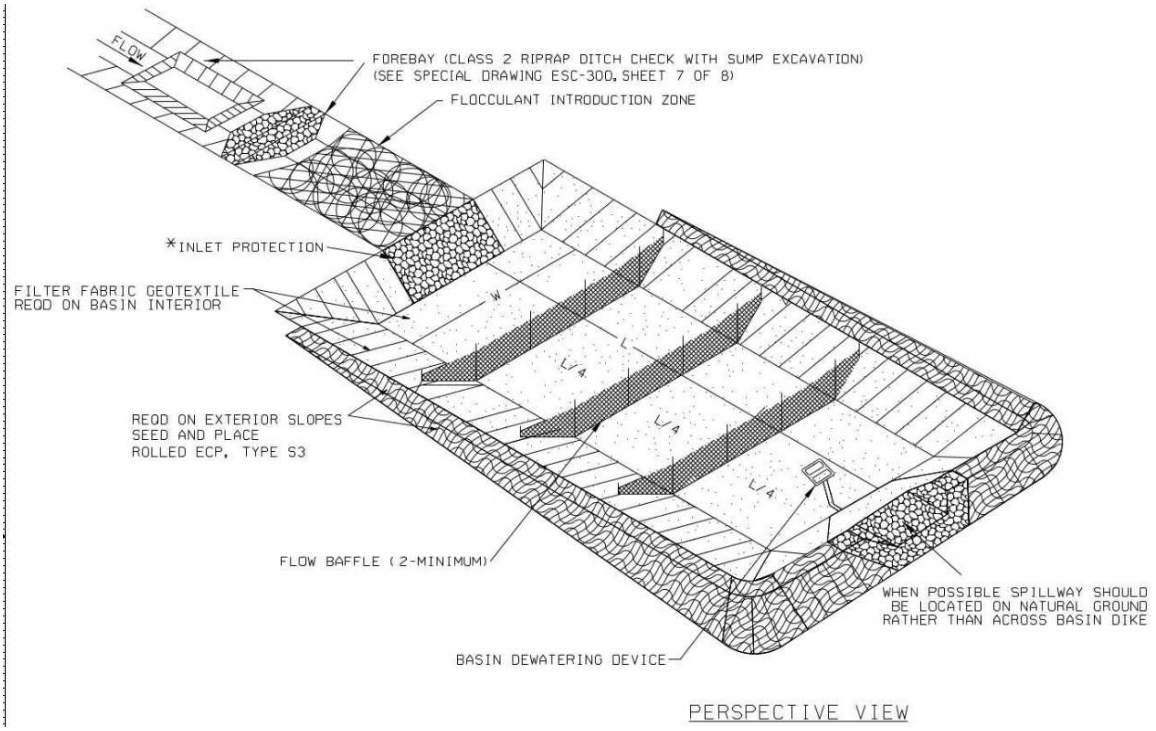

Figure 6.3: Standard ALDOT sediment basin design (ALDOT)

results presented here included the test runs that involved the filling of the basin in two phases. The first filling stage (referred here as Test A) started with an empty basin and ran for half hour with water inflows of $0.042m^3/s$ or 1.5cfs and the soil particle load rate of $20.5kg/min$ or $45.2lb/min$. This test did fill the basin close to its capacity, but did not result in overflow. The basin underwent a dewatering process for 4.5 hours, in which turbidity levels drop across the basin. Then the second filling stage (referred here as Test B) initiated, raising the water depth within the basin to a point in which overflows occur through the emergency spillway and lasting for half hour. No addition of flocculant occurred during these experimental runs.

It should be noted that, prior to the first repetition of a given configuration, the basin was cleaned of sediment. However, basin cleaning was not performed during the two subsequent repetitions within the tested configuration. Also, since the tests were conducted in different seasons, which impact water temperature and consequently its viscosity, a correction in the observed turbidity was implemented in all reported results, following the empirical relation proposed by Perez (2016):

$$NTU_C = \frac{NTU_M}{1.76e^{-0.025*T}} \tag{6.1}$$

Figure 6.4: The deployment of HRS corresponding to configuration 3 and 4 (Perez, 2016).

where NTU_C is the corrected turbidity value, NTU_M is the measured turbidity value, T is the water temperature in ^{o}C.

Then, for one of the tested configurations (HRS with longitudinal flows), 500 mL samples were collected at five points along the sediment basin apparatus (seen in Figure 6.1). These samples were taken to the Geomorphology Laboratory at Auburn University Department of Geosciences. Particle size distributions (PSD) of the soils presented in the water samples were obtained with the aid of a laser diffraction apparatus Malvern Mastersizer 3000 analyzer. This apparatus provided a distribution of soils particles with sizes ranging from 0.1 μm up to 3 mm. Unlike PSD tests based on sieve analysis that quantify size ranged by weight, soil particles were individually counted by this equipment, and percentages preselected size ranges were reported. Repetition of these types of measurements were not performed over different configurations, and the results from the collected samples were compared with the PSD from a soil sample taken from the original stockpiles used in the investigation.

In the last step, further treatment with SSHRS and PAM were applied to the discharge from the skimmer. The overarching goal of the approach was to assess the benefits of using of a high-rate settler and PAM to treat the effluent of a sediment basin discharged by the skimmer after it passed through the sediment basin in Configuration 4. The SSHRS tank and its typical operating status are shown in Figure 6.5. The PAM treatment panel with zig-zag chicanes and its typical operating status are shown in Figure 6.6. This panel was designed to enable enough turbulence and contact time by creating relatively high flow velocity at the chicanes for the PAM to mix well with sediment. As shown in the figure, the panel was installed above the SSHRS tank and the skimmer discharge pipe was extended under this configuration. This mixing unit had dimensions of 4 ft by 8 ft, and has shallow (4-in height) walls. It was designed to allow for residence time of water in the range of 50 to 80 seconds, depending on the flow rate and slopes, and discharge water with flocculants in the SSHRS unit. Two small Applied Polymer Systems (APS) 706b Floc Log blocks were cut into pieces and these were installed in the contraction flow zones of the mixing unit, where velocity and turbulence was higher. This allowed for improved mixing of PAM and the sediment-laden flows.

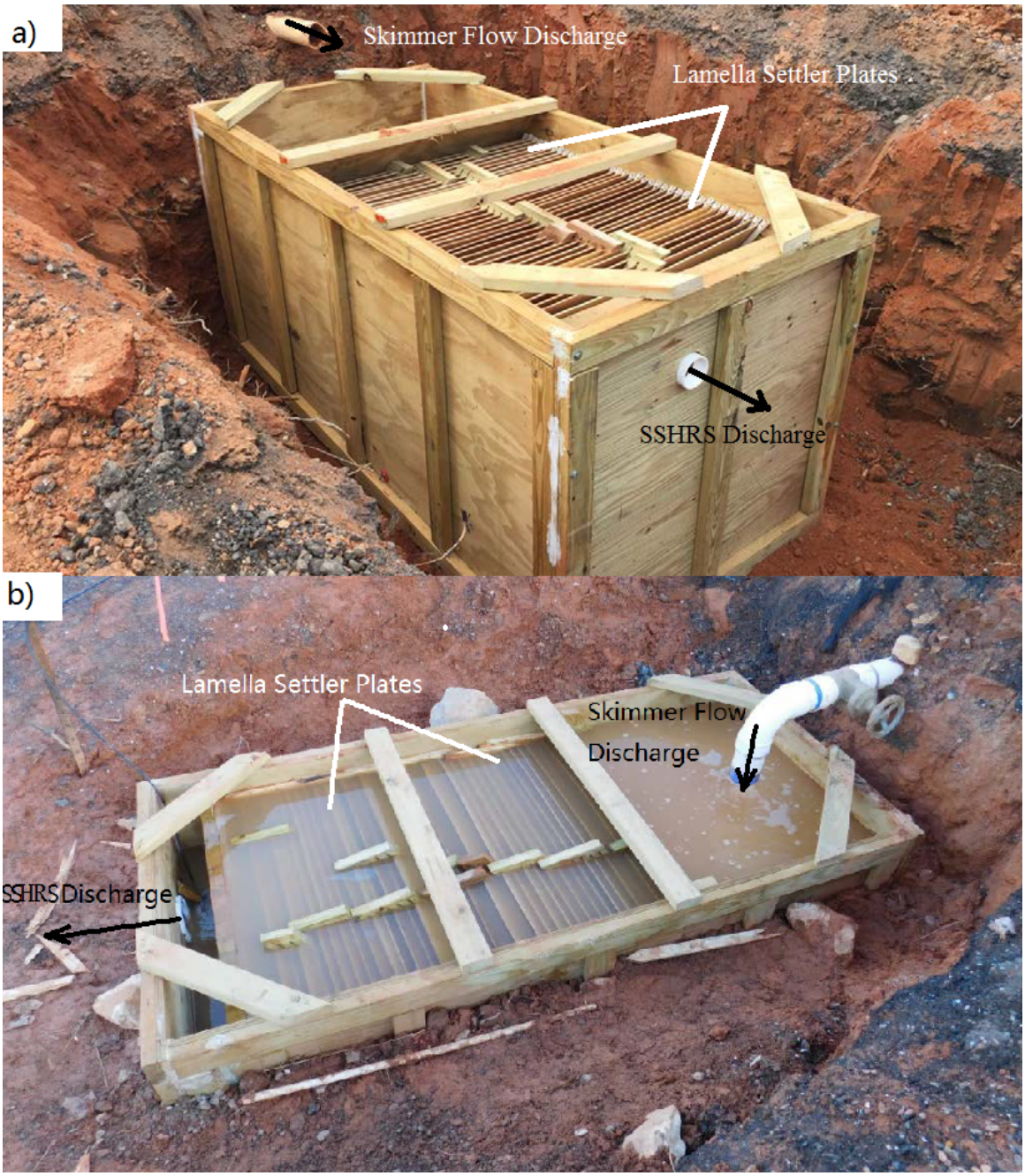

Figure 6.5: a) SSHRS tank and b) its operating status

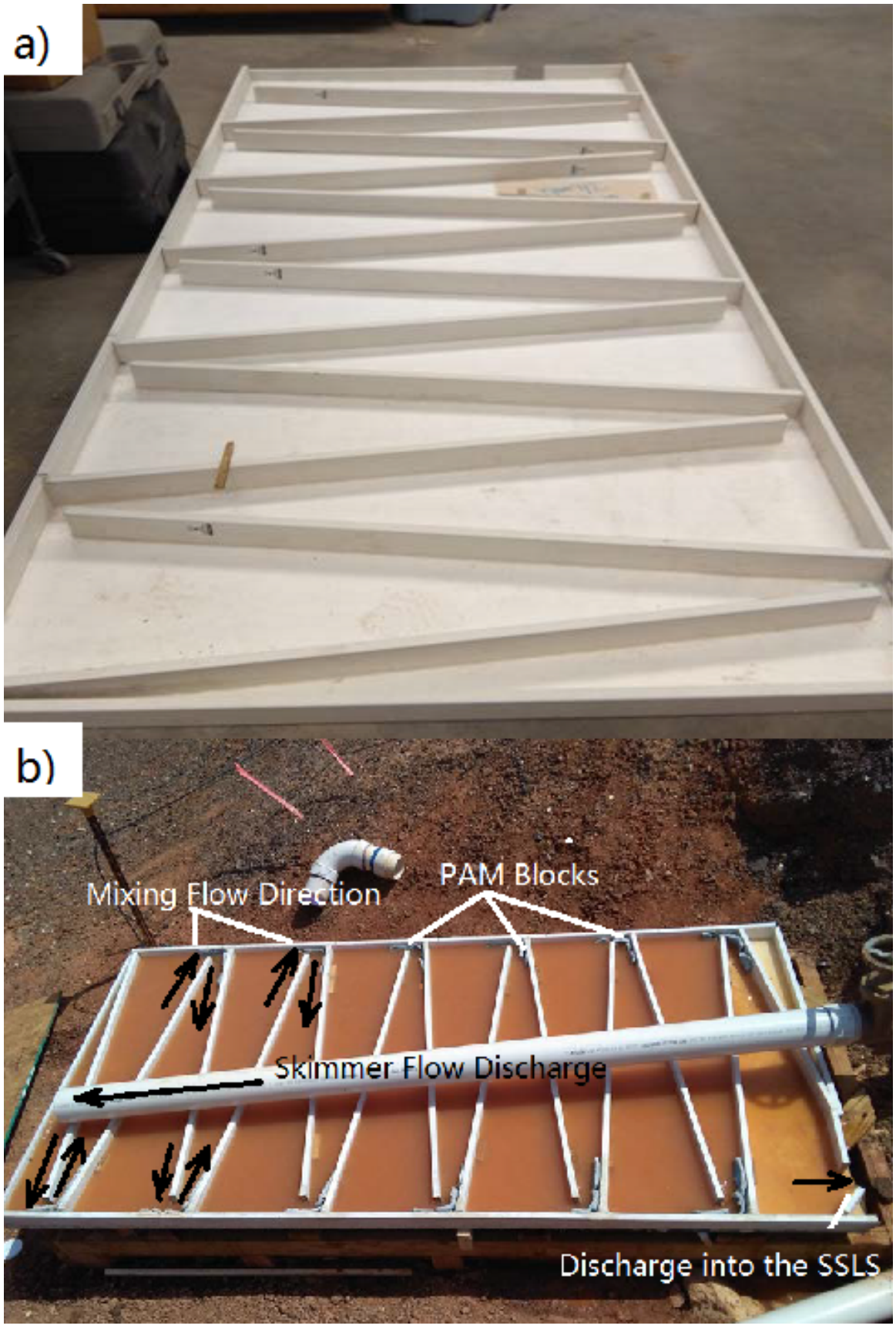

Figure 6.6: a) PAM treatment panel with zig-zag chicanes and b) its operating status

6.2.2 Numerical modeling methodology

The numerical simulation in current chapter was also achieved with OpenFOAM. Differently from the previous two chapters, air phase compressibility was neglected here due to open channel conditions and very little air entrainment. Thus, the VOF based incompressible two-phase flow solver interFOAM was applied, of which the governing equations were the same as Equation 3.6 and 3.7. $SST\ k-\omega$ turbulence model were used to resolve the turbulence. The shear stress transport (SST) combined turbulence model $SSTk-\omega$ model (Menter, 1993) could be expressed as:

$$\rho\frac{\partial k}{\partial t}+\rho\nabla\cdot(\vec{U}k)=P-\beta^{*}\rho k\omega+\rho\nabla\cdot\Big[(\nu+\sigma_{k}\nu_{t})\nabla k\Big] \tag{6.2}$$

$$\rho\frac{\partial \omega}{\partial t}+\rho\nabla\cdot(\vec{U}\omega)=\frac{\gamma}{\nu_{t}}P-\beta\rho\omega^{2}+\rho\nabla\cdot\Big[(\nu+\sigma_{\omega}\nu_{t})\nabla\omega\Big]+2(1-F_{1})\frac{\rho\sigma_{\omega^{2}}}{\omega}\nabla k\cdot\nabla\omega \tag{6.3}$$

where k was the turbulence kinetic energy, ω was specific dissipation rate, P was a production term related to shear stress, ν and ν_t were kinematic viscosity and turbulent kinematic viscosity, respectively, F_1 was a blending function, β, σ, and γ were all constants.

The CFD basin model was based on the basin geometry used in the large-scale testing described in Perez et al. (2016), with few simplifications such as assuming an axis of symmetry and a shorter inlet channel to reduce the mesh size and speed up simulations. The specific model setup and dimensions were the same shown in Figure 6.2. The basin was separated into four bays with three layers of porous baffles.

Porous media are materials with pores that allow fluid passage but also lead to an dissipation of the kinetic energy (Roth, 2012). There are various types of porous media, such as soil, porous or fissured rocks, ceramics, fibrous aggregates, filter paper, sand filter, etc. (Bear, 1972). The porous media that is relevant to the current research are jute/coir baffles, as shown in Figure 6.7, of which the percent open area was 21.7% (Perez, 2016). As stated in Chapter 2, Thaxton et al. (2004) showed that jute/coir outperformed other baffle alternatives in reducing mean flow velocities in basins through experiments. However, there was no previous studies on the simulation fluids passing though jute/coir baffles using CFD.

Figure 6.7: Single layer of jute/coir baffles used in experimental research of sediment basin flows

In OpenFOAM, porous media is defined as a flow region that create head loss governed by Ergun Equation (Ergun, 1952), which refers the pressure head loss is caused by simultaneous kinetic and viscous energy losses. Such relation can be expressed as:

$$\Delta p = -(D_v \mu U + 0.5 I \rho |U|^2) L_p \tag{6.4}$$

where Δp is pressure loss, D_v is Darcy coefficient or viscous resistance, μ is dynamic viscosity, U is velocity, I is inertial coefficient or inertial resistance, ρ is fluid density, and L_p is the porous media length in the flow direction. The Darcy coefficient D_v and inertial coefficient I are determined by the following formulas:

$$D_v = \frac{150(1-e)^2}{\phi^2 D_p^2 e^3} \tag{6.5}$$

$$I = \frac{2 * 1.75(1-e)}{\phi D_p e^3} \tag{6.6}$$

where e is porosity of the media, ϕ is sphericity of the particles making the media (assumed as 0.75), and D_p is the diameter of particles making the media. The present CFD model with porous baffles applied three layers of porous baffles with $D_v = 2000$ and $I = 1000$. These parameters were not calibrated.

6.3 Research results

6.3.1 Turbidity distribution during filling and dewatering a basin with soil-mixed water

The present subsection shows the measured results of turbidity distribution during the basin filling and dewatering processes for each of the configurations presented in the previous section. Figure 6.8 presented the turbidity at each of the three monitored depths in the basin for the first and last bays in the sediment basin for Configuration 1 (ALDOT standard design). The turbidity results were averaged over the three repetitions for this test configurations, and time zero corresponded to the flow introduction into the basin. For Test A (initial filling) turbidity results were reported for each depth as soon as the water depth reached the elevation of the

sampling point. This corresponded in average to 15 minutes for the 1-ft elevation station, 24 minutes for the 2-ft elevation station and close to 29 minutes for the 3-ft elevation station. As for Test B (second filling), samples were collected in the 1-ft and 2-ft elevation stations as soon as 5 minutes into the test. Within 10 minutes, water depth increased to a point where samples could also be collected by the 3-ft elevation station.

For Test A results, as it would be anticipated, turbidity values were at the highest levels during flow admission stages. Turbidity declined immediately after inflow introduction stopped, and the rate of drop was more pronounced in the Bay 1. Turbidity values were in general higher at the Bay 1 than Bay 4 within the sediment basin during filling stages. Also, turbidity levels increased from the surface toward the bottom of the basin.

For Test B results, it was noticed that the average turbidity of the lower two layers in Bay 1 increased from 350NTU to 900NTU within 5 minutes when the second inflow was introduced into the basin. Turbidity levels of samples collected at the three elevations were consistent, with smallest turbidity values reported at the 3-ft elevation station. As inflows stopped, turbidity values began to drop in the Bay 1 immediately. Results on the Bay 4 were not as straightforward. The growth in turbidity in the last bay was delayed by 15-20 minutes after flow started, and was first noticed in samples collected at the 3-ft elevation station. Turbidity in samples from the 3-ft elevation station were the maximum one for about 15 minutes into the test, and then was surpassed by the turbidity at lower layers. This seemed to indicate that a plume of fine soils was advected in the upper layer of the flow within the basin. It should also be noted that since the instantaneous water turbidity could be affected by many other factors, such as wind and blockage of sampling tubing, which can explain some unusual fluctuation in turbidity results.

As it was noticed, the turbidity values of samples collected in all bays and depths varied considerably over the duration of a given test. In order to quantify this process, it was decided to calculate the average turbidity during the filling process and the early dewatering stages, which ranged from 45 to 60 minutes. This calculation was performed for all four tested configurations, and for each configuration averages were computed for Test A (initial filling) and Test B (second filling). Results from these calculations are presented in Figure 6.9.

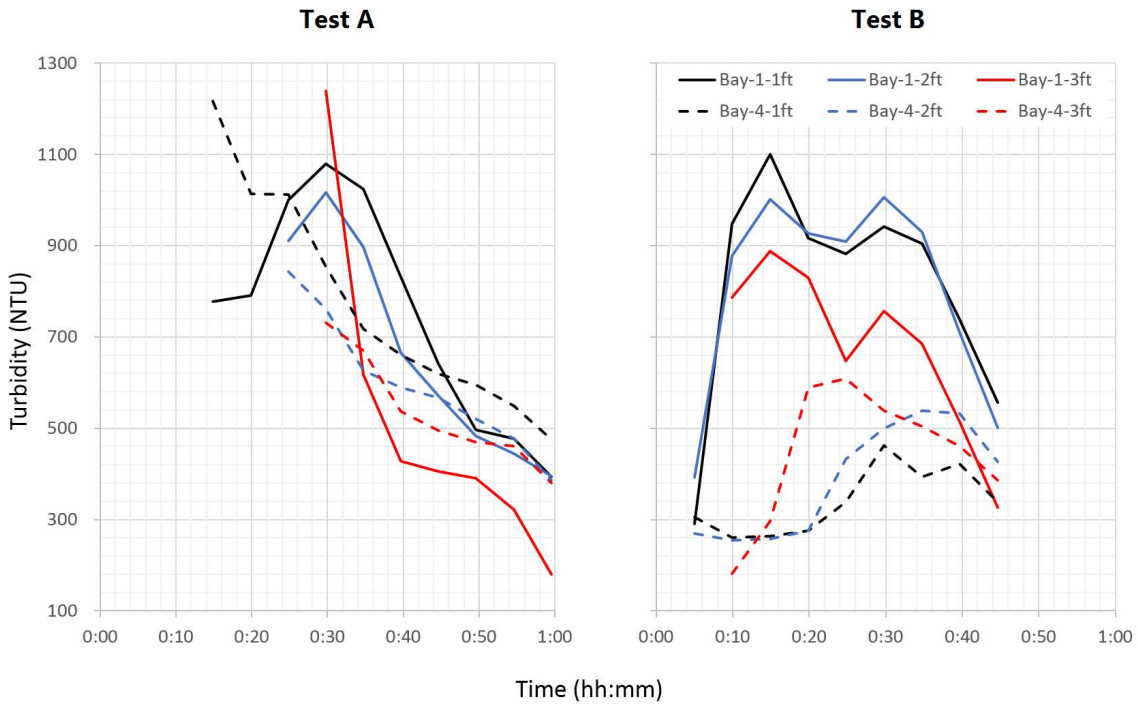

Figure 6.8: Turbidity hydrograph at different layers of water flows during filling and dewatering a basin with Configuration 1 during initial filling (Test A), and second filling that led to overflows (Test B). Results corresponded to the average over three repetitions measured in Bay 1 and Bay 4.

Config.	Test	Run 1	Run 2	Run 3
1	A	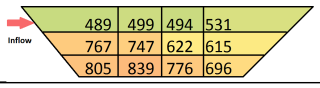	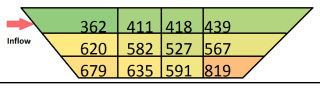	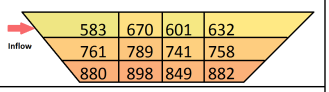
1	B	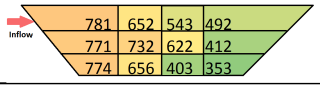	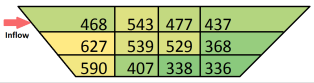	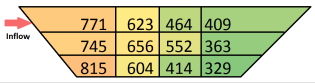
2	A	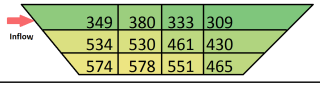	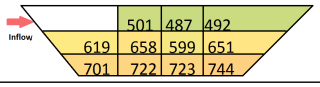	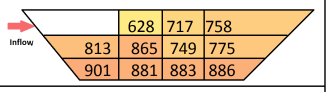
2	B	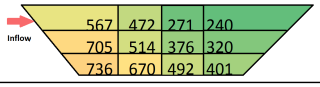	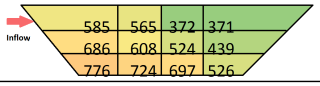	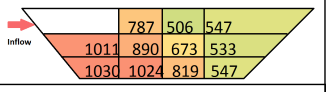
3	A	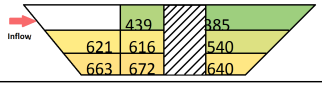	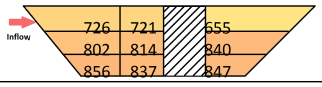	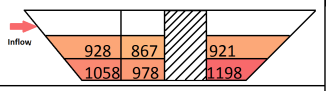
3	B	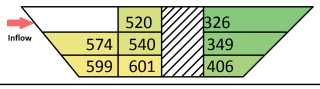	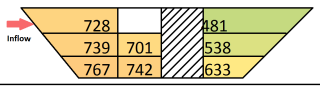	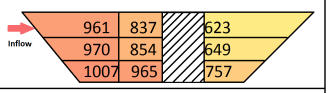
4	A	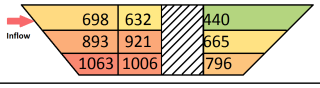	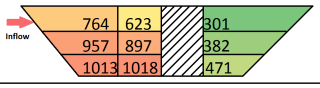	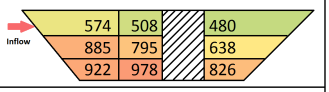
4	B	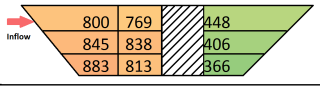	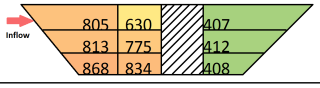	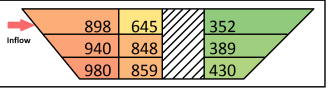

Figure 6.9: Average turbidity calculated for each run at different depths and bays. Results are presented for each tested configuration and Tests A and B. The hatched area in bay 3 for configurations 3 and 4 corresponded to the location of the HRS. White cells indicated occurrences where sampling failure occurred.

Table 6.1: Ratio of average turbidity measured at Bay 4 to the one measured in Bay 1 during the test runs

Config.	Test	Run 1	Run 2	Run 3
1	A	89%	110%	102%
	B	54%	68%	47%
2	A	83%	95%	94%
	B	48%	65%	53%
3	A	81%	98%	107%
	B	61%	74%	69%
4	A	72%	42%	50%
	B	48%	49%	42%

As was noticed, despite of the efforts in execute the experimental runs following the methodology explained in Perez et al. (2016), there were significant differences in the turbidity values measured in Bay 1, even when temperature correction in turbidity values were implemented. Highest inflow turbidities were observed in Configuration 4 (HRS longitudinal flow) tests, and smallest turbidity values were measured in the Configuration 2 (Improved baffle). One interesting observation was the difference in tests A and B results. For Test A results, turbidity in general increase between run 1 and 3 for all bays and depths, and at the third run the average turbidity at Bay 4 was comparable with the other bays. This was an important outcome, as it showed a loss in performance of basins in the early stages of dewatering with a sequence of sediment laden inflows. The ratio of average turbidity measured at Bay 4 to the one measured in Bay 1 during the test runs is listed in Table 6.1. Results for test A show that over the repetitions the basin loses its effectiveness in decreasing turbidity due to sediment accumulation, except for configuration 4. There is no clear trend for test B results.

On the other hand, experiments that involved a higher initial basin water level showed in general a decreasing turbidity gradient as flows moved from Bay 1 toward Bay 4 and the basin spillway. These tests were less impacted by the effect of the repetitions, and indicated that the basin was more effective in decreasing the turbidity across the bays when it was initially partially filled. From all the tested configurations, the HRS longitudinal was the most effective in decreasing turbidity across the basin. The average drop in turbidity measured in the top layer of the basin was 352 NTU, which corresponded to a drop of 46.5% in the average turbidity

measured in the top of Bay 1, which was the sample most representative of the inflows arriving at the sediment basin. By comparison, the relevant average turbidity drop ratios were 14.9%, 9.5%, and 38.6% for Configuration 1, 2, and 3, respectively.

6.3.2 Particle size characterization during filling and dewatering a basin with soil-mixed water

As it was pointed earlier, some samples were taken for a single experimental run (Configuration 4, Test A, Run 1) to evaluate eventual differences in the characteristics of soils present in the water-sediment suspensions that were created in sediment basin tests. It was hypothesized that during the different stages of the sediment-laden flow in the basin characteristics of the sediment sizes would differ, with coarser fractions being less abundant as inflows advanced toward Bay 4.

Indeed, as is shown in Figure 6.10, the original soil contained much higher percentage of particle with sizes ranging from 0.1 mm to 1.0 mm than the samples collected upstream from the sump (UP sump) and at the sump. However, it was noticeable the difference in the soil particles present in the sample taken from Bay 2, which had a greater fraction of fines and a statistical mode (i.e. peak percentage) of 7 μm. Samples taken downstream from the HRS plates (HRS) and at Bay 4 were similar and presented statistical mode also of 7 μm, however the fraction of fines was higher. Comparing PSD results from Bay 2 and Bay 4, it could be noticed a reduction in the concentration of soil sizes between 12 μm and 0.1 mm. This indicated that this was the particle size range in which the physical settling within the HRS takes place.

6.3.3 Experimental tests with the treatment of SSHRS and PAM

Figure 6.11 presented a comparison among the turbidity values of flow at basin entrance, the discharge from the skimmer and the SSHRS (Vasconcelos et al. 2017). Results indicated that the use of a SSHRS eliminated completely spikes in turbidity in the discharge. Such spikes were noticeable during the 2nd stage of the inflow admission, which generated overflows. By having the SSHRS treating the skimmer outflow, there was no sign of any turbidity increase, indicating that first flush conditions had been eliminated and that the turbidity levels were more

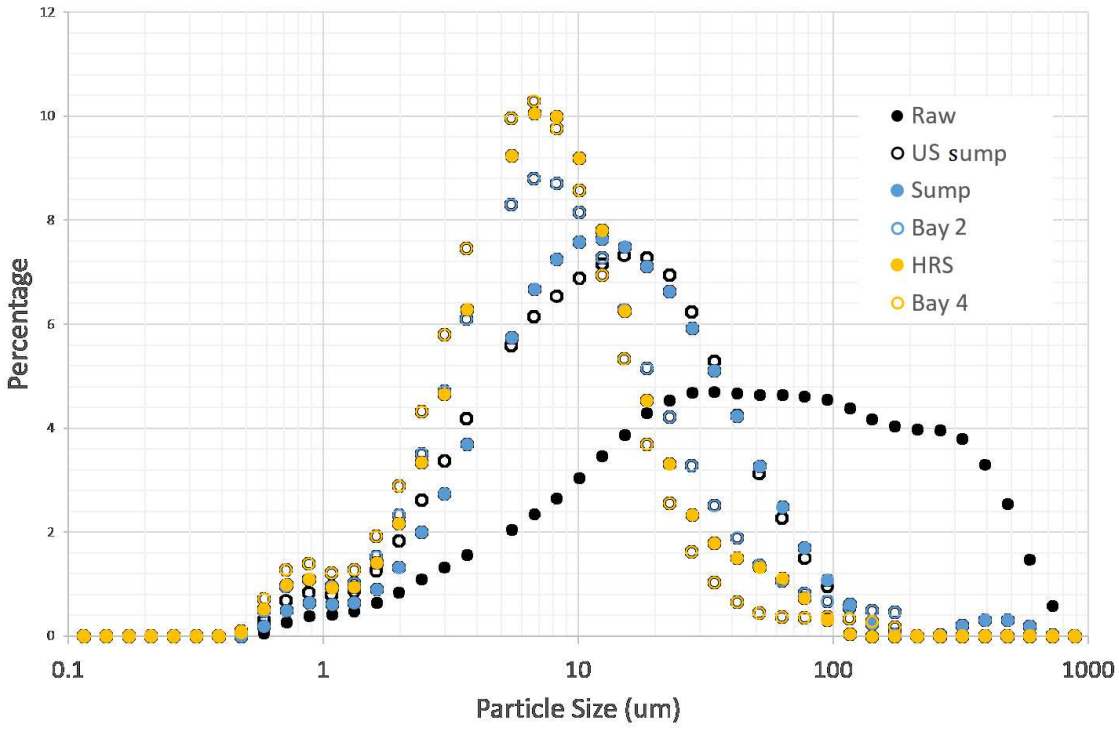

Figure 6.10: Particle size distribution of turbid water samples at different basin regions to the end of the test

predictable as they exiting the system. In absolute terms, however, there were no significant changes in the turbidity observed in Bay 4 (downstream from the lamella settlers within the sediment basin) and the turbidity discharged from the smaller settler unit. This might indicate a limit had been achieved for the particles that can be removed by physical processes within the sediment basin.

The physical limit of the settling efficiency was attributed to the size of the sediment particles in suspension, which were generally too small to be removed even by means of settling using the SSHRS with upward flow configuration. However, the effectiveness of this last treatment step could be improved by means of flocculants, such as PAM. One key difference of the proposed approach is to apply PAM only to the basin outflow. This provided an opportunity for physical sediment settling to occur first, and then used PAM only to facilitate settling of very fine sediments (e.g. clay size). The rationale was to decrease the PAM dosage in sediment basins, decreasing the potential of environmental discharge of these flocculants. The retaining of these flocculants that would prevent the discharge would be promoted within the actual SSHRS unit. Figure 6.12 showed the sediments accumulation on the PAM treatment panel with

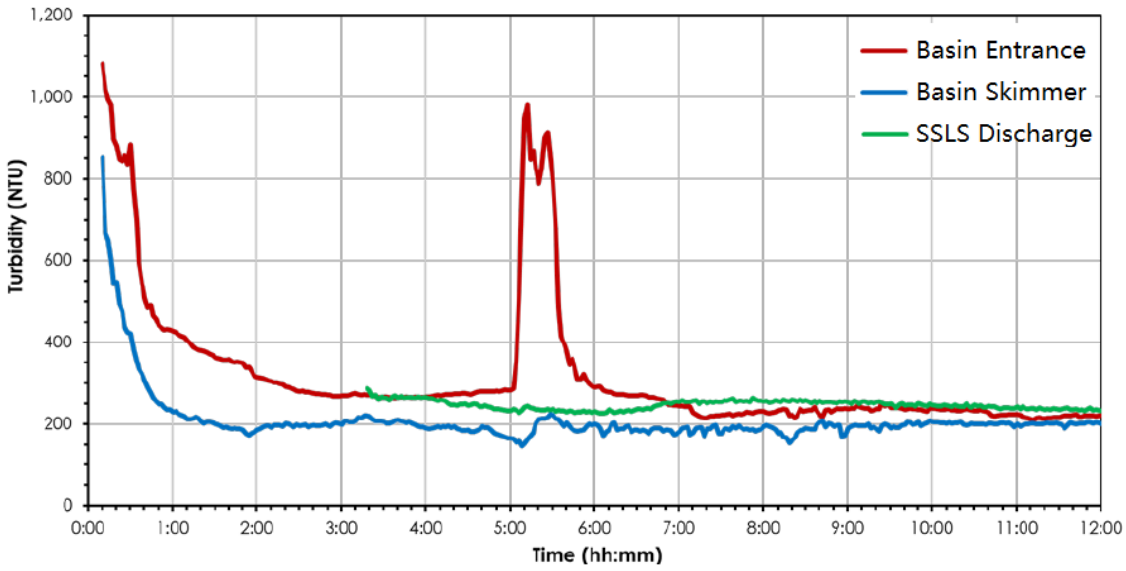

Figure 6.11: Turbidity results of the discharge from the skimmer and the SSHRS (Vasconcelos et al. 2017)

zig-zag chicanes towards the end of the third test repetition. The test results indicated that the sediment particles had been coagulated by the flocculant.

Turbidity results measured at the basin skimmer discharge and the outlet of the SSHRS with PAM treatment are presented in Figure 6.13. The results corresponded to three experimental repetitions in sequence (Runs 1 to 3) in which the lamella settlers were present in the sediment basin. Samples were collected every 5 to 10 minutes during the tests. The conditions mimic the runs performed earlier in this research, with the difference that the outflow from the skimmer passed through the PAM treatment panel with zig-zag chicanes and the SSHRS unit. As it could be noticed, turbidity results presented a significant drop between the inlet and outlet of the PAM treatment panel with zig-zag chicanes and the SSHRS. The range of turbidity drop between these two points was between 46%, observed in the initial tests, and 88% which was observed in the third run, with a very significant average turbidity reduction of 75%. One limitation of this study result was some samples were not collected.

While the mechanisms for PAM addition, as well the corresponding dosage, still need to be fine-tuned, these results indicated great potential of this combination. This can potentially avoid the use of active treatment processes, such as water recirculation via pumps within sediment basins, reducing costs and increasing the effectiveness of sediment control. Also of

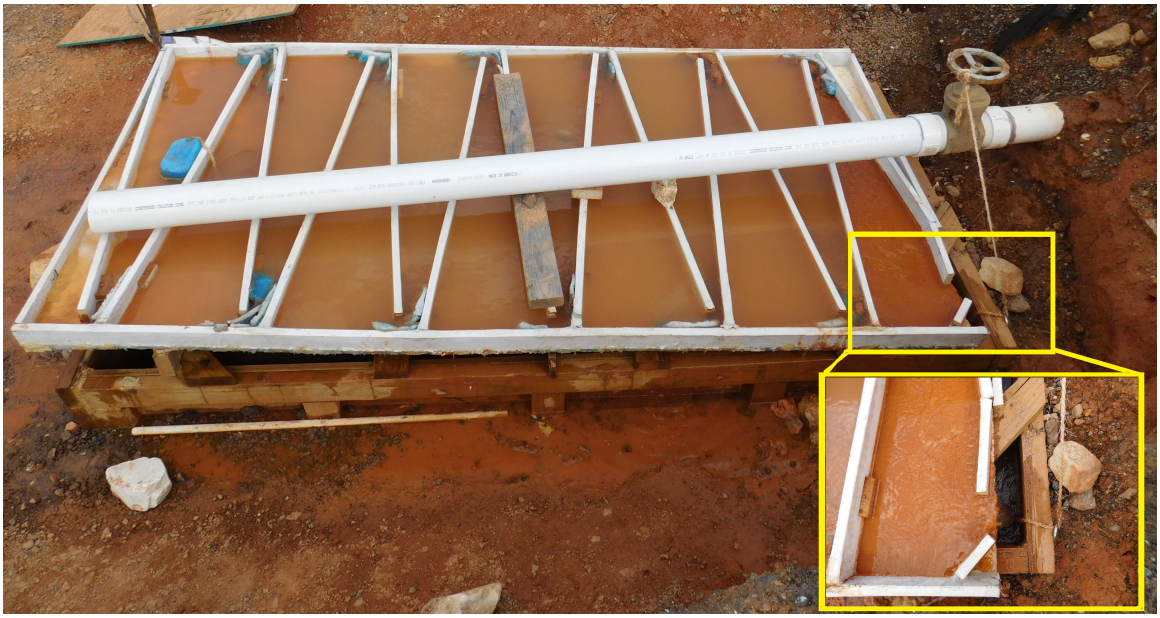

Figure 6.12: Sediments on the PAM treatment panel with zig-zag chicanes

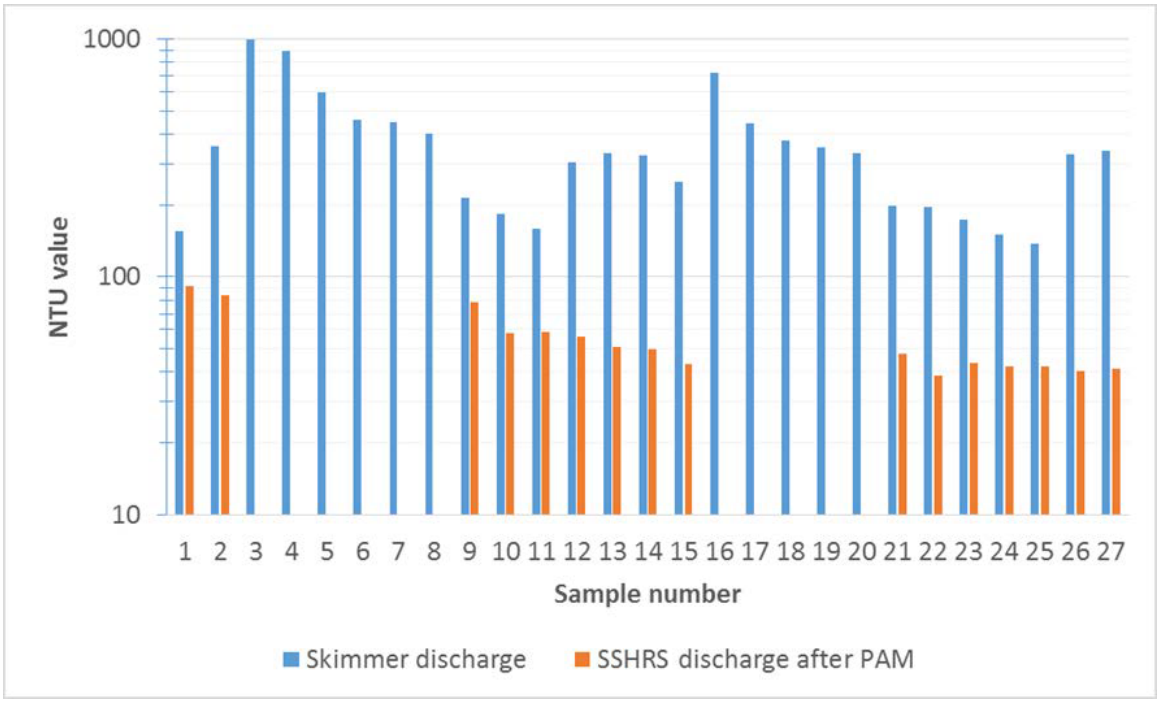

Figure 6.13: Turbidity results from samples collected at the inlet of the mixing tank (blue bars) and the outlet of the SSHRS with the use of PAM (orange bars). Orange bar results were only obtained when the water within small lamella settler reached its discharge level.

significance, the use of this alternative might result in decreased use of PAM, as these would be added to skimmer flows carrying the smallest particles that were not removed. This is a more desirable strategy compared to adding flocculant to sediment basin inflows that carry large fractions of particles that did not need PAM for improving settling. One limitation of the use of SSHRS with PAM was that it would not prevent the discharge of turbid water in case there is basin overflow. Such situation would be possible in sediment basins that had small storage volumes due to limiting factors such as limited available surface areas. In such conditions, a possible alternative would be the combination of high rate lamella settlers within the sediment basin with the use of PAM. Such conditions, however, were not tested in the present research.

6.3.4 Porous baffles and basin aspect ratio effects on flow fields during filling process

This subsection presented CFD results representing the process of basin filling with the use of interFOAM, focusing on determining the effects of porous baffles and basin aspect ratio to the flow characteristics. The simulations were performed with a mesh size of 371,000 cells, with higher discretization present near the boundaries of the basin. The rationale was that velocity values were significant in terms of settling and resuspension processes, and baffles had shown to influence velocity distribution in basins. The flow velocities magnitude and distribution in each bay of the configuration with intermediate basin aspect ratio, i.e. Length/Width=2.8, are presented first, followed with a velocity comparison among the three configurations with various basin aspect ratios.

Averages of velocity magnitudes in each bay over time with and without baffles were calculated and are presented in Figure 6.14. It should be pointed out that because the mesh size at the bottom of the basin was 2.5cm, during the initial filling stage, there could be some unusual fluctuations on the averaged flow velocities, which also appeared in Figure 6.16. Simulation results indicate that during the initial minutes the averaged flow velocity was very high due to the small depth across the basin. The average velocity at Bay 1 with and without baffles was comparable, however significant differences in the average velocity at Bays 2 to 4 were noticed. Porous baffles, as it would be anticipated, have created a strong drop in velocities in all bays. Within 2 minutes of the simulation there was a drop in the flow velocity in Bay 1, due to water

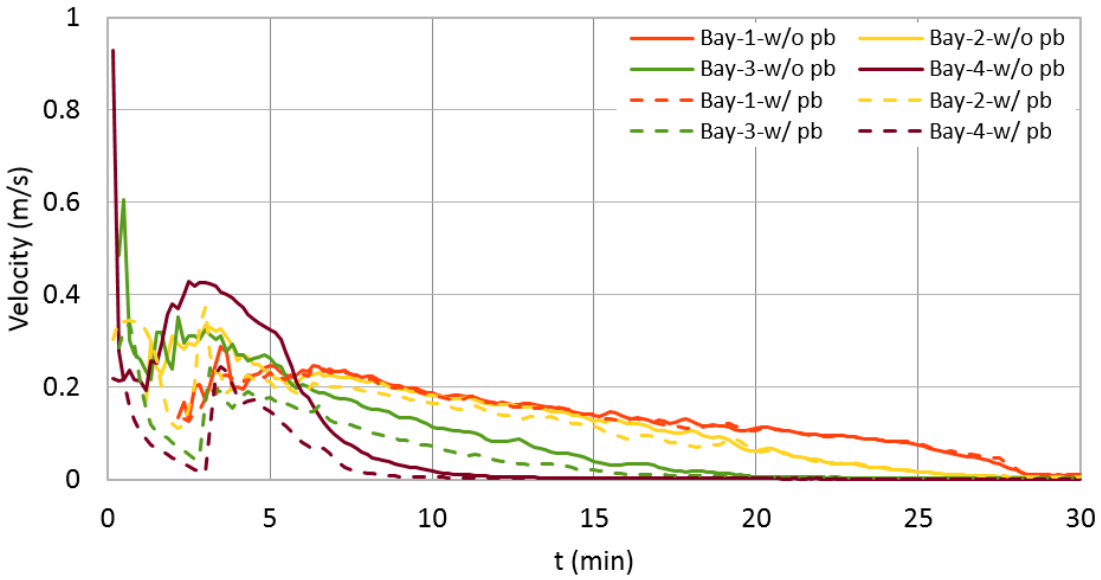

Figure 6.14: Averaged water phase velocity in the sediment basin undergoing filling process for the treatment without and with porous baffles

depth growth created by filling. At about 3-4 minutes the average velocity values across the basin were comparable, but results with baffles were consistently smaller. Over time, however, the difference between average velocity results with and without porous baffles decreased.

The presence of baffles also influenced the water circulation patterns in the sediment basin, particularly in the early stages of the flow, as it is shown in Figure 6.15. Velocity magnitudes and streamlines were shown at 3 minutes following the flow admission. While flow pattern was not too different in the region of Bay 1, it might be noticed that the absence of baffles created a zone of strong recirculation near Bay 4, right about where the skimmer was installed. On the other hand, results with porous baffles indicated smaller velocities and more circulation of flow between Bays 2 and 3.

The results in Figure 6.16 indicated that basins with larger length-to-width ratio could significantly reduce the average flow velocity in Bay 4 when compared to short basins when porous baffle was not applied. However, when porous baffles were used, no significant flow velocity decline was observed between basins with low and high aspect ratios while the highest average flow velocity appeared in the basin with intermediate length-width ratio. This could be attributed to that the flow velocity that had been significantly reduced after passing through

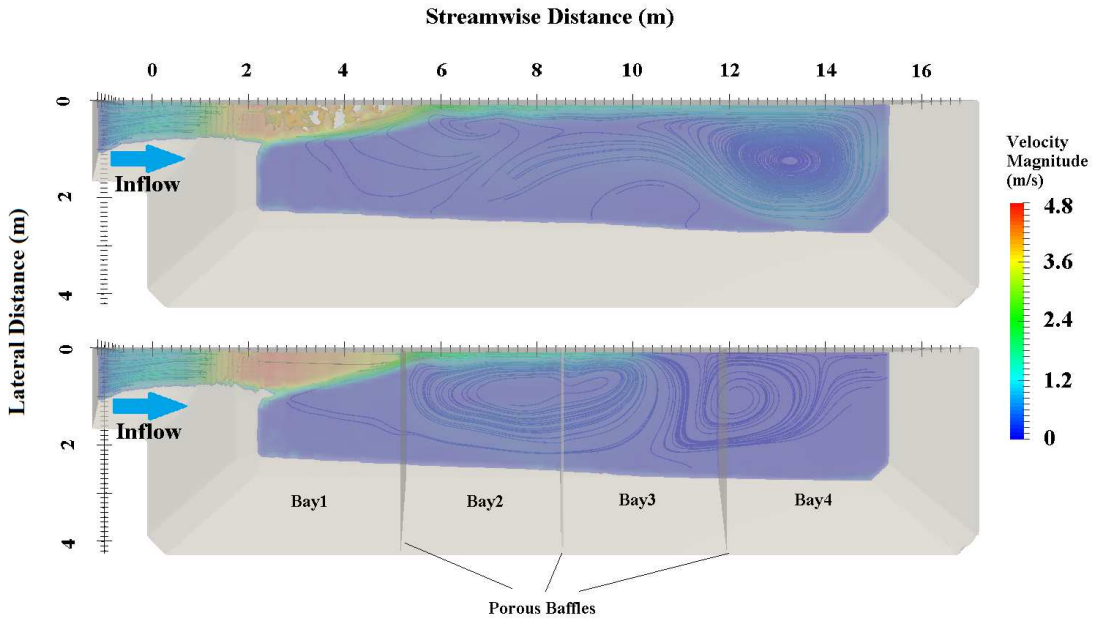

Figure 6.15: Plan view of flow velocity distribution in the sediment basin for the treatment without (upper) and with (lower) porous baffles (t=3min)

the porous baffles and the effects from the basin aspect ratio were no longer as significant as the configuration without porous baffles. At this point it could not be explained why the basin with intermediate aspect ratio performed worst so far and further investigation needed to be implemented.

The above simulation results are interesting and indicate the potential of using CFD results to understand flow characteristics within sediment basins. Much work is still needed in this topic, which include calibration of porous baffle characteristics to achieve a better understand of flow circulation patterns for varying conditions in these basins.

6.4 Summary and future work

Flow characterization in sediment basins undergoing filling and dewatering processes are still largely unknown and most design recommendations are based on empirical evaluations. While valuable, use of flow simulation may provide further insights on the processes and result in some design recommendations. This work presented results of experimental data collection of turbidity at various locations within the depth and length of a sediment basin, as well obtained PSD characterization of suspended soils present in a sediment basin during a filling event. It

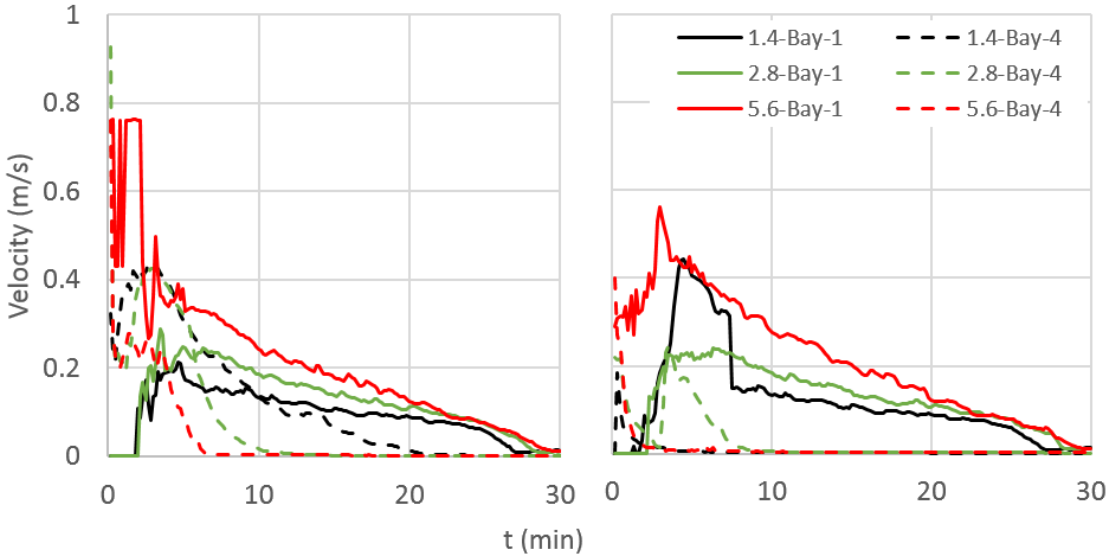

Figure 6.16: Averaged flow velocities in Bay 1 and 4 of basins with various basin aspect ratios a) without porous baffles and b) with porous baffles

was hoped that these results could help in the development and calibration of future numerical models to represent such flows. Flocculant was also tested to treat fine soil particles by using a mixing panel and an SSHRS tank. Also a CFD model was constructed with the objective of evaluate the effects of porous baffles and basin aspect ratios in the simulation. While the results obtained in this research are intuitive, more work is needed to assess how the modeling parameters of baffles can influence the numerical solution.

In all, it is recommended to apply the longitudinal configuration of Lamella High Rate Settler in a sediment basin on construction sites. The flocculant and SSHRS tank proved very effective in treating the discharge from skimmers, and are thus recommended with adequate dosage of polyacrylamide. The next chapter presents another interesting topic regarding flows in sediment basins, the resuspension of soil particles, and proposes and evaluates a cellular confinement system that is used for preventing resuspension.

Chapter 7

Resuspension of Soil Particles Caused by Shear Forces

7.1 Research objectives

The last part of the present work aims to evaluate the effectiveness of a cellular confinement system (CCS) as means to prevent soil resuspension in sediment basins. In this process, various geometries of cellular confinement were simulated with different shear flows. Velocity and turbulence kinetic energy (TKE) were the key parameters being considered here to assess the protection effectiveness of the CCS. TKE was correlated with geometric and flow characteristics and with the observed turbidity of the flow with resuspended particles.

7.2 Methodology

InterFOAM was also applied to simulation the flow conditions in current chapter and both $k-\epsilon$ and $SST\ k-\omega$ models were attempted to resolve the turbulence. SnappyHexMesh was used to generate for coarse, intermediate, and fine mesh resolutions for a mesh independence study. The approximate mesh size at the cellular confinement cell region was 2 by 2 mm (23,000 mesh cells in total), 1 by 1 mm (28,000 mesh cells in total), and 0.5 by 0.5 mm (53,000 mesh cells in total) for coarse, intermediate, and fine mesh resolutions, respectively. Mesh independence test was achieved with intermediate and finer mesh, and intermediate mesh size was finally selected as the applicable resolution that would be used in the rest of the work.

The CFD model created in current research was attempted to describe the flow characteristics of the experiments conducted by Simpson et al. (2016). To better replicate the experimental apparatus, the CFD geometric model (Figure 7.1) was very similar to the physical model, but a 2D simplification was performed to reduce the computational effort, and was justifiable considering that lateral flows (e.g. across the 12.5 cm width of the apparatus) were visually absent. The cell were set as 2D walls with front (upstream) and back (downstream) faces. A 0.3 m wide

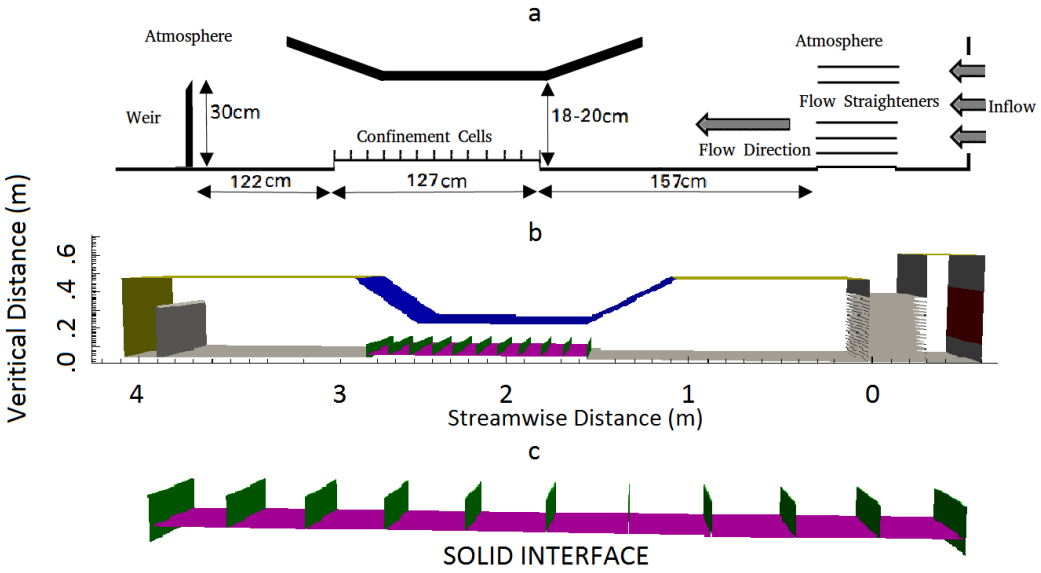

Figure 7.1: CFD geometric model: a) sketch, b) CFD model, and c) details of 2D CCS model

Table 7.1: Scenarios tested in sediment resuspension experiments

Geometric characteristics	Low flow velocity (25 cm/s)	High flow velocity (50 cm/s)
H= 5.0 cm, W = 3.0 cm	H5-W3-25	H5-W3-50
H= 5.0 cm, W = 6.1 cm	H5-W6-25	H5-W6-50
H= 5.0 cm, W = 12.2 cm	H5-W12-25	H5-W12-50
H= 7.5 cm, W = 3.0 cm	H8-W3-25	H8-W3-50
H= 7.5 cm, W = 6.1 cm	H8-W6-25	H8-W6-50
H= 7.5 cm, W = 12.2 cm	H8-W12-25	H8-W12-50

2D rectangular inlet was applied, and the bottom wall inside the cellular confinement cells was raised by 25 mm in order to replicate the initial thickness of sediments within the cells.

All the configurations of experiments tested were studied with CFD as shown in Table 7.1. The cell height and width were represented with H_c and W_c, respectively. Similarly to the experiments, the channel was partially filled prior to the simulation beginning. The top of the calculation field was setup with atmospheric conditions with the exception of the contracted section. Two velocities at the contracted section, 0.50 m/s and 0.25 m/s, were enforced as in the experiments. The numerical simulations were conducted with resources from the Alabama Supercomputer Authority (Alabama Supercomputer Authority, 2016) and the Hopper Cluster at Auburn University.

7.3 Results

Simulation of the cellular confinement scenarios were performed with interFOAM for all geometries. One limitation of the technique used was the inability of simulating the motion of the sediment particles explicitly. However, this limitation did not impact the main goals for the CFD modeling, which were to calculate the velocity intensity and patterns inside the confinement cells. It was designed to calculate the peak TKE at the soil interface in initial stages of the flow, and developing an estimate of the relationship between peak turbidity, and flow velocities inside the cellular confinement cells.

Figures 7.2 and 7.3 presented the results for all the velocity patterns for the cases involving the use of cellular confinement protection. In these two figures, flows were represented from right to left, and the bottom of each figure corresponded to the initial position of the soil interface. Also, only the initial 38 cm of the flows over the confinement cells are presented, since after this point the counter-clockwise recirculation zones were repeated in the cells downstream. Figure 7.2 results show that for W6 and W12 cases, flow velocities near the soil interface can be comparable to the free stream velocity, particularly within the two cells at the leading edge. To a smaller extent, the region at the bottom of W3 cells exposed to larger velocities was comparatively smaller. The same general observations were valid for the 7.5-cm cell height results (H8 cases) presented in Figure 7.3.

However, one interesting observation was drawn from flow patterns within confinement cells in the H8-W3-25 and H8-W3-50 cases, which were the cases that yielded the smallest peak turbidities in the laboratory experiments. These patterns were distinct in that there were two recirculation zones within each cell, creating smaller velocity values at the bottom of the cells, which in turn led to less soil resuspension. Based on these observations, it appeared that confinement cells with geometries having ratios of H_c/W_c in excess of 2.5 create these dual recirculation zones, and reduce the likelihood of soil resuspension.

It was speculated that flow velocities and geometric characteristics of the cellular confinement cells would influence the turbulence experienced by soil particles. CFD results of the peak TKE for every cell in each geometry were calculated, and results are presented in Figure 7.4. It

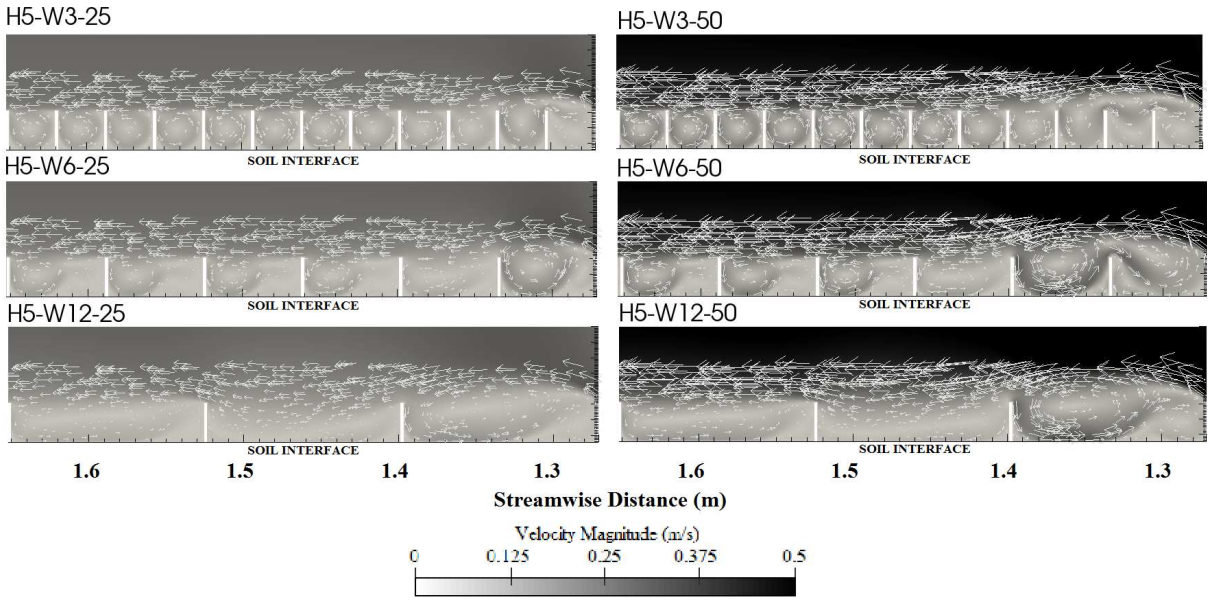

Figure 7.2: Velocity patterns in confinement cells calculated with the CFD model for 5.0-cm height confinement cells

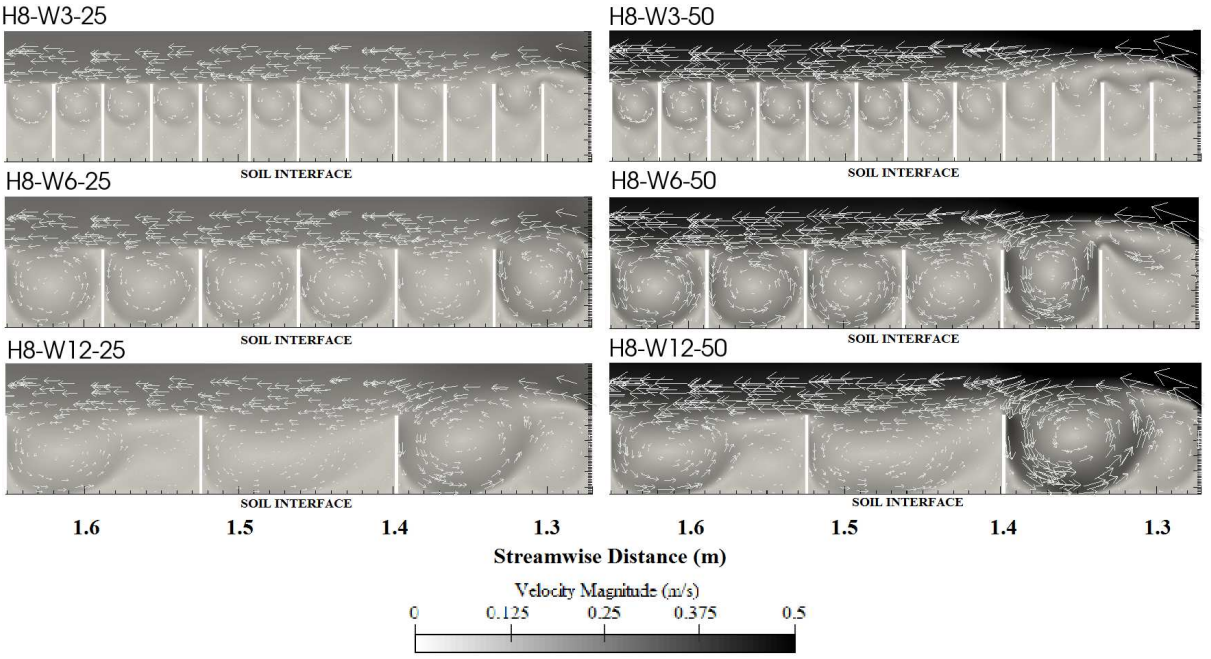

Figure 7.3: Velocity patterns in confinement cells calculated with the CFD model for 7.5-cm height confinement cells

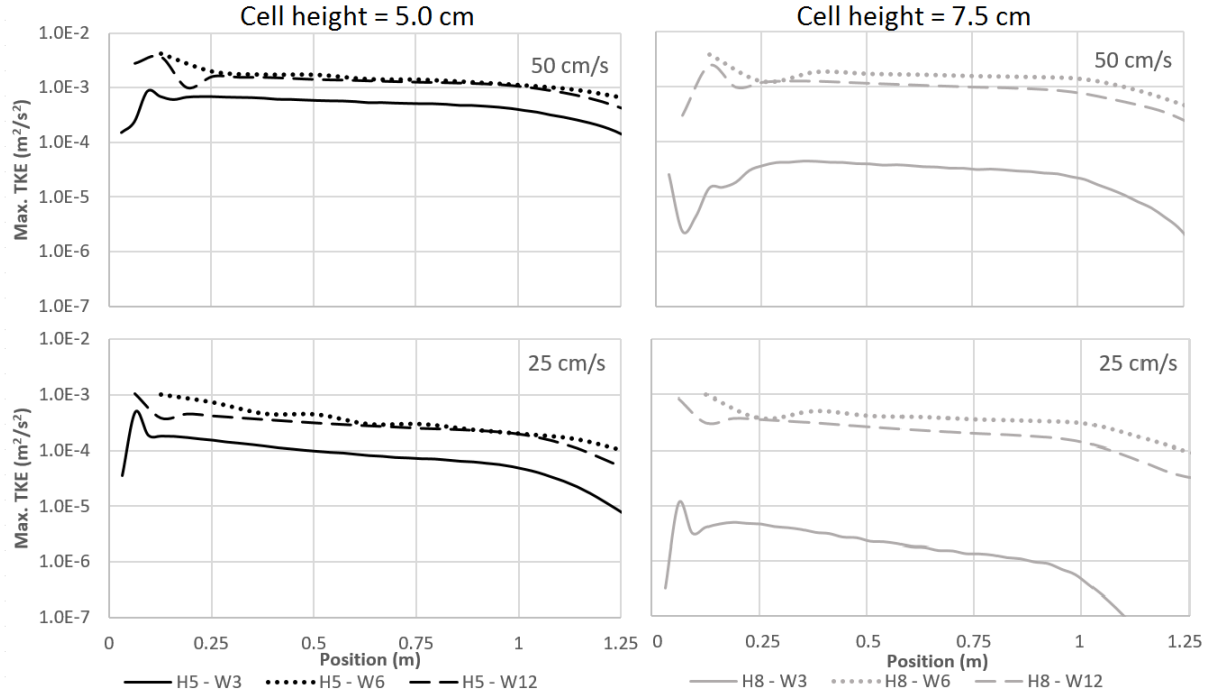

Figure 7.4: Relationship between the geometry and free stream velocity and the peak TKE for all confinement cells tested

should be anticipated that the free stream flow velocity had a major influence in the peak TKE. The height of the cells had a significant influence in TKE, particularly for the smallest cell width of 3.0 cm. Based on these observations, a non-dimensional parameter was proposed that combine the effects of flow velocity at the soil interface and its geometric characteristics. This parameter was referred to as resuspension parameter (R_P), and was expressed in the equation 4.3:

$$R_P = \frac{V_{int}(W_c^2/H_c)}{\nu} \tag{7.1}$$

Where V_{int} was the peak velocity at the soil interface, averaged among the confinement cells, ν was the kinematic viscosity. The relationship between R_P and the peak turbidity in the tests are presented in Figure 7.5. A regression equation relating R_P and the peak turbidity ($R^2 = 0.804$) was derived for the soils used in this investigation, and presented as equation 4.4. However, it should be noted that it was limited to the soils used in this experiment.

$$NTU_{PEAK} = 42.5 + 0.0064R_P \tag{7.2}$$

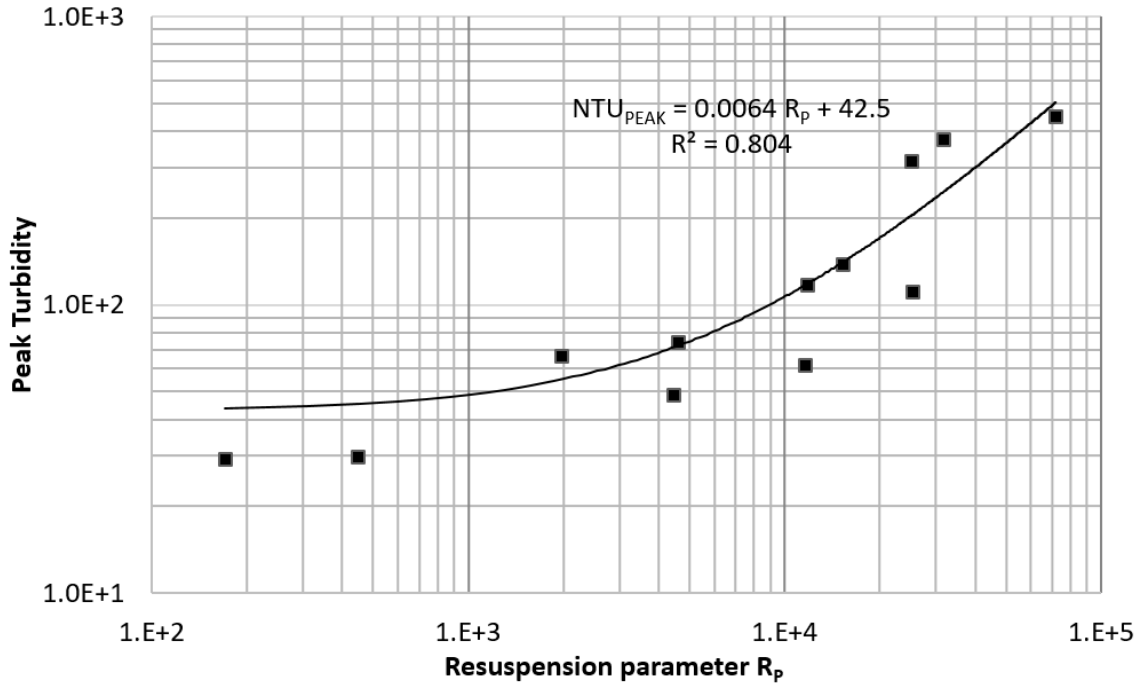

Figure 7.5: Peak turbidity in measured in experiments versus the calculated R_P

The resuspension parameter could be a potentially useful means to provide a general idea of the combination of cell heights/widths and intra-cell velocities, and how these impact the anticipated peak turbidity that would be linked to the processes of resuspension.

7.4 Summary

Sediment resuspension is particularly worsened in situations when new inflows are admitted in sediment basins in which the dewatering process is almost complete. In such cases, these new inflows create large velocities and turbulence that will result in resuspension. It is intuitive that to provide protection for settled sediments against shear forces should have an impact in the process of resuspension of sediments, and with this, a reduction in the turbidity of the water that is discharged from sediment basins. However, there was no study to date that has looked in to this process with the objective of quantifying the benefits of different cellular confinement cell geometries against resuspension.

Simulations of flow scenarios within the cells using CFD indicated that the confinement cells that presented the smallest turbidity peaks corresponded to the cases where there were two recirculation zones within the cells. A recommendation for adopting CCS geometries is that

cells should have H_c/W_c ratios exceeding 2.5. These cells were shown to be more effective in preventing resuspended sediments, causing a decrease in the velocity close to the soil-water interface in the range of 95% of the original free stream velocity. It was also noticed that the peak TKE in each containment cell increased with larger cell width W_c and smaller cell height H_c, as would be anticipated. Based on these results, and on the flow patterns that were simulated, it was decided to compute the peak velocity within each containment cell and relate this calculated velocity and cell geometry within the non-dimensional Resuspension Parameter (R_P). It was shown that for the tested soil there was a positive correlation between R_P and the peak turbidity for all 12 tested cases that involved protection. The relationship derived between R_P and NTU is unique for each soil, however, once it was determined experimentally, R_P could be useful in estimating peak turbidity values that were expected for soils protected by cellular confinement cells. Future research can focus on applying the CCS on a large scale test apparatus and heavy sediment loading conditions. More sophisticated CFD models are also desired to be used in relevant research, such as particle tracking models.

Chapter 8

Conclusions

The present work applied CFD models and large-scale experiments to achieve new insights in flow characteristics associated with of unsteady multiphase flows in different contexts of stormwater management applications. In particular, the research showed the potential of CFD models on representing complex and relevant problems, including air water interactions in stormwater systems and flows in sediment basins. The following sections summarize the major findings in the sequence of the chapters presented in this dissertation.

8.1 Flow characteristics of stormwater geysering caused by air pocket releasing

To achieve the objectives presented in the chapter focusing on stormwater geysering events, a CFD model created with OpenFOAM was initially calibrated with experimental data. The calibration was successful and showed the capability of the CFD model to describe this type of flow conditions. Subsequent CFD simulations of large scale geometries indicated that in general, the normalized incremental free surface elevation in the vertical shaft increased with larger air pocket, smaller vertical shaft diameter, and smaller initial water levels. The velocity of free surface motion increased with larger air pocket and smaller initial water levels. Among all tested vertical shaft diameters, $D_s/D = 0.5$ was the worst vertical shaft geometric configuration. The CFD simulations also indicated that a sequence of geyser events was relevant to the release of a sequence of air pockets and the water fluctuation and geyser intensity can be worsened by the release of a sequence of small air pockets. It was also shown that geyser events could be mitigated by applying the strategy of extending the lower rim of the vertical shaft into the horizontal tunnel alignment.

There are still many knowledge gaps yet to be addressed in future research, for instance, other CFD modeling approaches and more sophisticated turbulence modeling should be attempted in the context of stormwater geyser applications. Also, more detailed studies of sequences of air pocket release with various geometries and flow conditions need to be implemented in physical experiments. Many issues regarding to shaft retrofit strategy have not been solved, like energy loss caused by the blockage of the extended shaft lower rim. The ultimate aim of the research is to provide guidelines for designers with more detailed understanding of geysering events, and how to design against such occurrences.

8.2 Manhole cover displacement created by sudden pressurization of vertical shafts during rapid filling of stormwater systems

The chapter focusing on manhole cover displacement aimed to describe the sudden pressurization of vertical shafts in stormwater systems undergoing rapid filling using CFD approach. Such investigation aimed to evaluate the likelihood of manhole cover displacement during intense rain events. Two mechanisms were considered, including inertial surge and air pocket release through vertical shaft. The CFD results indicated that with limited manhole ventilation, both mechanisms might lead to air pressurization at the headspace of a vertical shaft, however the release of entrapped air pockets was more likely to cause manhole cover displacement. The results also found that for both mechanisms manhole cover could be triggered by the direct impact of water, which was also damaging to connected structures and/or pavement.

While this research advanced the understanding on the possibility of manhole cover displacements, some aspects of this problem require further investigation. First, it should be noticed that the simulation results are highly dependent to the specific geometry and flow conditions. Future work should focus on simulations with varying shaft geometries, initial flow conditions, as well as different inflow scenarios. Moreover, experimental data is still needed for more detailed CFD model validation. Future research could also consider the motion of the manhole cover when pressure builds up underneath with dynamic mesh techniques.

8.3 Settling processes in sediment basins undergoing filling and emptying processes

This chapter presented both experimental and CFD studies of flows in sediment basins undergoing filling and emptying processes with various basin configurations. The experimental data of the turbidity distribution and variation in the basin indicated that the Lamella High Rate Settler with longitudinal configuration was the most efficient in decreasing turbidity among all tested configurations. The experiments also found that the treatment with flocculant and SSHRS could significantly remove soil particles that could not settle in the basin. The CFD simulations attempted to represent porous baffles in sediment basins and the results indicated that porous baffles could significantly decrease the flow velocity in the basins, particularly in the downstream bays, where skimmers are typically located. The CFD simulations also compared the performance of basins with various length-width aspect ratios and indicated that longer basin was more effectively to reduce the flow velocity in the downstream bays when porous baffles were not applied.

In the future, additional experiments with more detailed study on the SSHRS and flocculant treatment should be implemented, particularly on optimizing flocculant dosage amount. It should also be noted that the CFD simulation of the porous baffles is still at the preliminary stage, and the calibration of the parameters is still needed.

8.4 Resuspension of soil particles caused by shear forces

This chapter presented an study of flows associated with the soil particle motion and resuspension in sediment basins. A geometry similar to Cellular Confinement Systems(CCS) was utilized to prevent resuspension in a laboratory scale test. CFD model was applied to describe the flow conditions within the cells. It was found that the confinement cells that presented the smallest turbidity peaks corresponded to the cases where two recirculation zones were observed within each cell. Large scale CCS deployments should attempt to mimic this geometry to effectively reduce soil particle resuspension. It was also noticed that the peak TKE in each containment cell increased with larger cell width and smaller cell height. Future research can

focus on validating CCS strategy to prevent sediment particle resuspension on large scale apparatus and heavy sediment loading conditions. More sophisticated CFD models, such as particle tracking models, should be applied in future related investigations.

References

[ALDOT] Alabama Department of Transportation (ALDOT). Typical Temporary Erosion/Sediment Control Applications. ESC-200-1, Index No. 1161.

[ALDOT (2015)] Alabama Department of Transportation (ALDOT) (2015). Standard Best Management Practices. Montgomery, AL.

[Alabama SWCC (2014)] Alabama Soil and Water Conservation Committee (SWCC) (2014). Alabama Handbook for Erosion Control, Sediment Control and Stormwater Management on Construction Sites and Urban Areas. Vol. 1, Developing Plans and Designing Best Management Practices.

[Allen and Voiland (2017)] Allen, J. and Voiland, A. (2017 April 11). Dam Breach at Mount Polley Mine in British Columbia. NASA (Visible Earch). Retrieved from https://visibleearth.nasa.gov/.

[Baines (1991)] Baines, W.D. (1991). Air cavities as gravity currents on slope. *J. Hydr. Eng.*, DOI: 10.1061/(ASCE)0733-9429(1991)117:12(1600).

[Batchelor(1967)] Batchelor,G. K. (1967). *Introduction to Fluid Dynamics*. Cabridge University Press. Cambridge, U. K.

[Bear (1972)] Bear, J. (1972). *Dynamics of fluids in porous media*. American Elsevier Publishing Company, Inc. New York, U.S.A.

[Benjamin (1968)] Benjamin, T.B. (1968). Gravity currents and related phenomena. *J. Fluid Mech.* 31: 209-248, 1968.

[Bentzen et al. (2009)] Bentzen, T.R., Larsen, T., and Rasmussen, M.R. (2009). Predictions of resuspension of highway detention pond deposits in interrain event periods due to wind-induced currents and waves. *Journal of Environmental Engineering.* 135(12): 1286-1293, 2009.

[Booth et al. (2000)] Booth, J.G., Miller, R.L., McKee, B.A., and Leathers, R.A. (2000). Wind-induced bottom sediment resuspension in a microtidal coastal environment. *Continental Shelf Research.* 20(7): 785-806, 2000

[CASQA (2011)] California Stormwater Quality Association (CASQA) (2011). CASQA Stormwater BMP Handbook Portal: Construction.

[Catano-Lopera et al.(2014)] Catano-Lopera, Y., Tokyay, T., Martin, J., Schmidt, A., Lanyon, R., Fitzpatrick, K., Scalise, C., and Garcia, M.(2014) Modeling of a Transient Event in the Tunnel and Reservoir Plan System in Chicago, Illinois. *J. Hydr. Eng.*, DOI: 10.1061/(ASCE)HY.1943-7900.0000888.

[Chan et al. (2017)] Chan, S.N., Cong, J., and Lee, J.H.W. (2017). 3D Numerical Modeling of Geyser Formation by Release of Entrapped Air from Horizontal Pipe into Vertical Shaft. *J. Hydr. Eng.*, DOI: 10.1061/(ASCE)HY.1943-7900.0001416.

[Chien and Wan (1999)] Chien, N. and Wan Z.H. (1999). Mechanics of Sediment Transport: Incipient motion of sediment.

[Choi et al. (2014)] Choi, Y., Leon, A.S., and Apte, S.V. (2014). Three-dimensional numerical modeling of air-water geyser flows. *Proc., 2014 ASCE World EWRI Congress*, 2014.

[Chosie et al. (2014)] Chosie, C.D., Hatcher, T.M., Vasconcelos, J.G. (2014). Experimental and numerical investigation on the motion of discrete air pockets in pressurized water flows. *J. Hydr. Eng.*, DOI: 10.1061/(ASCE)HY.1943-7900.0000898.

[Clar et al. (2004)] Clar, M.L., Barfield, B.J., and OConnor, T.P. (2004). Stormwater Best Management Design Guide Volume 3 Basin Best Management Practices. *Environmental Protection Agency*, 2004

[Cong et al. (2017)] Cong, J., Chan, S.N., and Lee, J.H.W. (2017). Geyser Formation by Release of Entrapped Air from Horizontal Pipe into Vertical Shaft. *J. Hydr. Eng.*, DOI: 10.1061/(ASCE)HY.1943-7900.0001332.

[Crimaldi and Ramos (2016)] Crimaldi, L. and Ramos, N. (Feb. 12, 2016).. Answers sought in manhole cover fatality on Expressway. Retrieved on Jun. 22, 2017 from https://www.bostonglobe.com/.

[CWA] Clean Water Atlanta. Combined Sewer Overflow (CSO) Remediation Plan. Retrieved on Apr. 18, 2017 from http://www.cleanwateratlanta.org/wastewater/CSOFactSheet.pdf/.

[Cundall and Strack (1979)] Cundall, P.A. and Strack, O.D. (1979). A discrete numerical model for granular assemblies. *geotechnique.* 29(1): 47-65, 1979.

[Dufresne et al. (2009)] Dufresne, M., Vazquez, J., Terfous, A., Ghenaim, A., and Poulet, J.B. (2009). Experimental investigation and CFD modelling of flow, sedimentation, and solids separation in a combined sewer detention tank. *Computers and fluids.* 38(5): 1042-1049, 2009.

[EPA (1976)] EPA (1976). Erosion and sediment control-Surface mining in the eastern US.

[EPA (2004)] EPA (2004). Report to Congress on Impacts and Control of CSO's and SSO's.

[EPA (2005)] EPA (2005). NPDES General Permit for Storm Water Discharges From Construction Activities.

[EPA (2007)] EPA (2007). Developing your stormwater pollution prevention plan: a guide for construction sites.

[EPA (2012)] EPA (2012). Construction General Permit.

[Ergun (1952)] Ergun, S. (1952). Fluid flow through packed columns. *Chemical Engineering Progress.* 48: 89-94, 1952.

[FEMA (2009)] Federal Emergency Management Agency (FEMA) (2009 November). Protecting Manufactured Homes from Floods and Other Hazards: A Multi-Hazard Foundation and Installation Guide. FEMA P-85, Second Edition. November, 2009.

[Fernndez and Nirshl (2013)] Fernndez, X.R. and Nirschl, H. (2013). Simulation of particles and sediment behaviour in centrifugal field by coupling CFD and DEM. *Chemical Engineering Science.* 94: 7-19, 2013.

[Festa and Hansen (1976)] Festa, J.F. and Hansen, D.V. (1976). A two-dimensional numerical model of estuarine circulation: the effects of altering depth and river discharge. *Estuarine and Coastal Marine Science.* 4(3): 309-323, 1976.

[Festa and Hansen (1978)] Festa, J.F. and Hansen, D.V. (1978). Turbidity maxima in partially mixed estuaries: A two-dimensional numerical model. *Estuarine and Coastal Marine Science.* 7(4): 347-359, 1978.

[Fourie (2015)] Fourie, C. (Jun. 13, 2015). Dislodged manhole cover causes accident. Retrieved on Apr. 18, 2017 from http://krugersdorpnews.co.za/.

[Foxnews.com, 2016] Foxnews.com (Aug. 5, 2016). 'Dancing' manhole cover takes internet by storm Retrieved on Jun. 18, 2018 from http://video.foxnews.com/.

[Griffin et al. (1985)] Griffin, M.L., Barfield, B.J., and Warner, R.C. (1985). Laboratory studies of dead storage in sediment ponds. *Transactions of the ASAE.* 28(3): 799-804, 1985.

[Guedes de Carvalho et al. (2000)] Guedes de Carvalho, J. R. F., Talaia, M. A. R., Ferreira, M. J. F.(2000) *Flooding instability of high-density gas slugs rising in vertical tubes filled with water. Chem. Engrg. Sci.* **55**: 3785-3802, 2000.

[Guo and Song, 1991] Guo, Q. and Song, C.S.S. (1991). Dropshaft Hydrodynamics under Transient Conditions. *J. Hydr. Eng.*, DOI: 10.1061/(ASCE)0733-9429(1991)117:8(1042).

[Hazen (1904)] Hazen, A. (1904). On sedimentation. *Transactions of the American Society of Civil Engineers.*53(2): 45-71, 1904.

[He and Marsalek (2014)] He, C. and Marsalek, J. (2014). Enhancing sedimentation and trapping sediment with a bottom grid structure. *Journal of Environmental Engineering.* 140(1), 21-29, 2014.

[Hirt and Nichols (1981)] Hirt, C.W. and Nichols, B.D. (1981). Volume of fluid (VOF) method for the dynamics of free boundaries. *J. Comput. Phys.* **39**(1): 201-225, 1981.

[Holmes, 2017] Holmes, S. (Jul. 26, 2017). 'It could have killed her: Manhole cover explodes and rockets 12ft in the air landing just a metre from where a woman was standing during flash floods in Gloucester city centre. Retrieved on Jun. 18, 2018 from http://www.dailymail.co.uk/.

[Launder and Spalding (1974)] Launder, B.E. and Spalding, D.B. (1974). The numerical computation of turbulent flows. *Computer methods in applied mechanics and engineering*, **3**(2): 269-289, 1974

[Lee et al. (2008)] Lee, B.J., Molz, F.J., Khan, A.A., and Schlautman, M.A. (2008). Simulation of Turbulent Flocculation and Sedimentation in Flocculent-Aided Sediment Retention Basins. 2008.

[Leon (2016)] Leon, A.S. (2016). New Evidence on the Causes of Explosives Geysers in Stormwater and Combined Sewer Systems: A Simplified Model for the Prediction of These Geysers. *Proc., 2016 ASCE World EWRI Congress*, 2016.

[Lewis (2011)] Lewis, J. W. (2011). *A Physical Investigation of Air/Water Interactions Leading to Geyser Events in Rapid Filling Pipelines*. Ph.D. Thesis. University of Michigan, 2011

[Lewis and Wright (2012)] Lewis, J.W. and Wright, S.J. (2012). Air-Water Interactions that Generate Large Water Lift through Vertical Shafts in Stormwater Conduits. *J. Water Mngmt. Modeling*, DOI: 10.14796/JWMM.R245-02, 2012.

[Lewis and Maynard (2016)] Lewis IV, M.R., Maynard, N.J. (2016). The DigIndy CSO Tunnel System.: 1239-1247, 2016

[Li and McCorquodale (1999)] Li, J. and McCorquodale, A. (1999). Modeling Mixed Flow in Storm Sewers. *J. Hydr. Eng.* **125**(11): 1170-1180, 1999.

[Lo (2018)] Lo, T. (Jun. 8, 2018). Spooky moment a manhole cover appears to dance in heavy rain on a Chinese street. Retrieved on Jun. 18, 2018 from http://www.dailymail.co.uk/.

[Keiser and Shapiro (2016)] Keiser, D.A. and Shapiro, J.S. (2016). Consequences of the Clean Water Act and the demand for water quality. *2016 Annual Meeting, Boston, Massachusetts, no. 235437.* Agricultural and Applied Economics Association, 2016.

[Klaver et al. (2016)] Klaver, P., Collins, D., Robinson, K., and Bell S.(2016). Modeling of Transient Pneumatic Events in a Combined Sewer Overflow Storage Tunnel System. *J. Water Mngmt. Modeling*, DOI: 10.14796/JWMM.C409.

[Kouyi et al. (2010)] Kouyi, G.L., Arias, L., Barraud, S., and Bertrand-Krajewski, J.L. (2010). CFD Modelling of flows in a large stormwater detention and settling basin. *NOVATECH.* 2010.

[Krone (1979)] Krone, R.B. (1979). Sedimentation in the San Francisco bay system. *San Francisco Bay: the urbanized estuary.* 85-96, 1979.

[Mandal et al. (2009)] Mandal, T.K., Das G., and Das P.K. (2009). Liquid Taylor bubbles rising in a vertical column of a heavier liquid: an approximate analysis. *Journal of Fluids Engineering.* 131,(1), 2009.

[Martin (1976)] Martin, C. S. (1976). Entrapped air in pipelines. In Proc., 2nd Int. Conf. on Pressure Surges, vol. 2, pp. 15-27. Bedford, UK: British Hydromechanics Research Association, 1976.

[Matsubara et al. (2013)] Matsubara, C., Kuo, T., and Wu, H. (2013). Comparison of the effects of $k-\epsilon$, $k-\omega$, and zero equation models on characterization of turbulent permeability of porous media. *J Water Resource Hydraul Eng*, **2**(2): 43-50, 2013

[McCaleb and Mclaughlin (2008)] McCaleb, M.M. and McLaughlin, R.A. (2008). Sediment trapping by five different sediment detention devices on construction sites. *Transactions of the ASABE.* 42(21): 1613:1621, 2008.

[McLaughlin (2015)] McLaughlin, R. (2015a, March 10). Chemical Treatment to Control Turbidity on Construction Sites. Retrieved from https://content.ces.ncsu.edu/.

[McLaughlin (2015)] McLaughlin, R. (2015b, March 10). Using Baffles to Improve Sediment Basins. Retrieved from https://content.ces.ncsu.edu/.

[MDEQ (2014)] Michigan Department of Environmental Quality (MDEQ) (2014). Michigan Nonpoint Source Best Management Practices Manual.

[Menter (1993)] Menter, F. (1993). Zonal two equation kw turbulence models for aerodynamic flows. *In 23rd fluid dynamics, plasmadynamics, and lasers conference.*: 2906, 1993.

[Metcalfe (2012)] Metcalfe, J. (Jul. 25, 2012). The Hidden Dangers of Driving Over Manholes: Watch cars get launched into the air like rockets due to ill-fitting manhole covers. Retrieved on Jun. 22, 2017 from https://www.citylab.com/.

[Millen et al. (1997)] Millen, J.A., Jarrett A.R., and Faircloth, J.W. (1997). Experimental evaluation of sedimentation basin performance for alternative dewatering systems. *Transactions of the ASAE.* 40(4): 1087-1095, 1997.

[minneapolismn.gov] minneapolismn.gov. City of Minneapolis Storm Tunnels: Tunnel Condition Ranking. Retrieved on Apr. 18, 2017 from http://www.minneapolismn.gov/.

[Muller and Vasconcelos (2016)] Muller, K. and Vasconcelos J.G. (2016). Large-Scale Testing of Storm Water Geysers Caused by the Sudden Release of Air PocketsPreliminary Research Findings. *In World Environmental and Water Resources Congress 2016*, pp. 442-451

[NASA (2004)] NASA,2004. Retrieved on April 14, 2017 from https://earthobservatory.nasa.gov/NaturalHazards/view.php?id=13683

[Naser et al. (2015)] Naser, G., Karney, B.W., and Salehi, A.A. (2005). Two-dimensional simulation model of sediment removal and flow in rectangular sedimentation basin. *Journal of environmental engineering.* 131(12): 1740-1749, 2005.

[NOAA (2008)] National Oceanic and Atmospheric Administration (2008). A Brief History of Pollution. Retrieved on April 14, 2017 from http://oceanservice.noaa.gov/education/kits/pollution/02history.html/.

[NRC (2009)] National Research Council (2009). Urban stormwater management in the United States. *National Academies Press*, 2009

[Nielsen and Davis (2009)] Nielsen, K. D. and Davis, A. L.(2009). Air migration analysis of the Terror Lake tunnel. *Proc., 33rd IAHR Congress, International Association for Hydraulic Research, Madrid, Spain, 262268.*

[NRCS (2010)] National Resources Conservation Service (2010). 2007 National Resources Inventory: Soil Erosion on Cropland.

[OpenFOAM Foundation, 2016] OpenFOAM Foundation (2016). OpenFOAM User Guide, version 4.0, Jun. 2016.

[Overbey (2014)] Overbey, D. (2014, October 15). Indianapolis Digs Deep to Fix its Enormous Sewer Overflow Problem [Web log post]. Retrieved on April 14, 2017 from http://danieloverbey.blogspot.com/.

[Parmakian, 1963] Parmakian, J. (1963). Waterhammer analysis. *Dover Publications Inc.*, 1963.

[Patrick and Vasconcelos (2015)] Patrick, A. and Vasconcelos, J. (2015). Air Entrainment Effects on the Pressure Wave Celerities Following Rapid Filling Pipe Flows. *Proc. 2015 ASCE EWRI Congress*, Austin, TX. pp. 1638-1647. doi: 10.1061/9780784479162.159

[Perez et al. (2016)] Perez, M.A., Zech, W.C., Fang, X., and Vasconcelos, J.G. (2016). Methodology and Development of a Large-Scale Sediment Basin for Performance Testing. *Journal of Irrigation and Drainage Engineering.* 142(10), 2016: 04016042.

[Perez (2016)] Perez, M. (2016). Improvements in the Design and Application of Erosion and Sediment Control Technologies for the Construction Industry. PhD Dissertation, Auburn University, 2016.

[Ramezani and Karney (2016)] Ramezani, L. and Karney, B. (2016). Water column separation and cavity collapse for pipelines protected with air vacuum valves: Understanding the essential wave processes. *Journal of Hydraulic Engineering.* 2016: 04016083.

[Ritter (1892)] Ritter, A. (1892). Die Fortpflanzung der Wasserwellen. *Zeitschrift des Vereines Deutscher Ingenieure.* 36.33(1892):947-954.

[Roth (2012)] Roth, K. (2012). Soil Physics Lecture Notes: Chapter 3 - Fluids in Porous Media. v2.2, 2012.

[Shao (2013)] Shao, Z.S.(2013). Two-dimensional hydrodynamic modeling of two-phase flow for understanding geyser phenomena in urban stormwater system. PhD Thesis, University of Kentucky.

[Shao and Yost (2018)] Shao, Z.S. and Yost, S.A. (2018). Numerical investigation of driving forces in a geyser event using a dynamic multi-phase NavierStokes model. *Engineering Applications of Computational Fluid Mechanics*, DOI: 10.1080/19942060.2018.1459322.

[Stoker (1948)] Stoker, J.J. (1948). The formation of breakers and bores the theory of nonlinear wave propagation in shallow water and open channels. *Communications on Pure and Applied Mathematics*, DOI: 10.1002/cpa.3160010101.

[Svenungsson (2016)] Svenungsson, J. (2016). Solving electric field using Maxwell's equations and compressibleInterFOAM solver Material course at Chalmers University of Technology, 2016.

[Teller (2012)] Teller, S. (2012). The Clean Water Act: 40 Years of Progress in Peril. Retrieved on April 14, 2017 from http://www.iwla.org/docs/default-source/conservation-docs/water-docs/clean-water-act/clean-water-act-40-years-of-progress-in-peril.pdf?sfvrsn=10/.

[Thaxton et al. (2004)] Thaxton, C.S., Calantoni, J., and McLaughlin, R.A. (2004). Hydrodynamic assessment of various types of baffles in a sediment retention pond. *Transactions of the ASAE.* 47(3): 741-749, 2004.

[Torres et al. (1982)] Torres, A., Kouyi, G.L, Bertrand-Krajewski, J.L., Guilloux, J., Barraud, S., and Paquier, A. (2008). Modelling of hydrodynamics and solid transport in a large stormwater detention and settling basin. *In 11 th International Conference on Urban Drainage.* 2008.

[Tsavdaris et al. (2015)] Tsavdaris, A., Mitchell, S., and Williams, J.B. (2015). Computational fluid dynamics modelling of different detention pond configurations in the interest of sustainable flow regimes and gravity sedimentation potential. *Water and Environment Journal.* 29(1): 129-139, 2015.

[Vasconcelos and Wright (2006)] Vasconcelos, J.G. and Wright, S.J. (2006). Mechanisms for air pocket entrapment in stormwater storage tunnels. *Proc., 2006 ASCE EWRI Congress, Omaha, NE*, 2006

[Vasconcelos et al (2009)] Vasconcelos, J.G., Moraes, J.R., and Gebrim, D.V. (2009). Field measurements and numerical modeling of a water pipeline filling events. *In Event Proc. 33rd IAHR Congress.* 2009.

[Vasconcelos and Wright (2011)] Vasconcelos, J.G. and Wright, S.J. (2011). Geysering generated by large air pockets released through water-filled ventilation shafts. *J. Hydr. Eng.*, DOI: 10.1061/(ASCE)HY.1943-7900.0000332.

[Vasconcelos et al. (2012)] Vasconcelos, J.G., Chosie, C.D., and Leite G.M. (2012). Investigation of air pockets compression and motion in stormwater storage tunnels. *In World Environmental and Water Resources Congress 2012: Crossing Boundaries.* 1458-1468, 2012.

[Vasconcelos and Wright (2016)] Vasconcelos, J.G. and Wright, S.J. (2016). Anticipating Transient Problems during the Rapid Filling of Deep Stormwater Storage Tunnel Systems. *J. Hydr. Eng.* 06016025, 2016.

[Vasconcelos et al. (2017)] Vasconcelos, J.G., Perez, M.A., Wang, J., Zech, W.C., and Fang, X.(2017). Final report: Evaluation of high-rate settling technology for sediment control in roadway construction sites. Jul. 2017.

[Webster (1981)] Webster, S.L. (1981). Investigation of Beach Sand Trafficability Enhancement Using Sand-Grid Confinement and Membrane Reinforcement Concepts. Report 2. Sand Test Sections 3 and 4 No. WES/TR/GL-79-20. Army Engieer Waterways Experiment Station, Vicksburg, MS, Geotechnical Lab, 1981.

[Weller et al. (1998)] Weller, H.G., Tabor, G., and Fureby, C. (1998). A tensorial approach to computational continuum mechanics using object-oriented techniques. *Comput. Phys.* **12**(6): 620-631, 1998.

[Wilkinson (1982)] Wilkinson, D.L. (1982). Motion of air cavities in long horizontal ducts. *J. Fluid Mech.* 118: 109-122, 1982.

[Wilcox (1998)] Wilcox, D.C. (1998). Turbulence modeling for CFD. (2). La Canada, CA: DCW industries, 1998.

[Wright et al. (2011)] Wright, S.J., Lewis, J.W. and Vasconcelos, J.G. (2011). Geysering in rapidly filling storm-water tunnels. *J. Hydr. Eng.* **137**(5): 543-555, 2011.

[Wright (2013)] Wright, S.J. (2013). Influence of Air Pocket Volume on Manhole Surge. *J. Water Mngmt. Modeling*, DOI: 10.14796/JWMM.R246-09, 2013.

[Wu et al. (2000)] Wu, W., Rodi, W., and Wenka, T. (2000). 3D numerical modeling of flow and sediment transport in open channels. *Journal of Hydraulic Engineering.* 126(1), 4-15, 2000.

[Wylie et al. (1993)] Wylie, E.B., Streeter, V.L., and Suo, L.(1993). Fluid transients in systems. Vol. 1. Englewood Cliffs, NJ: Prentice Hall, 1993.

[Yang (1965)] Yang, C.T. (1996). Sediment transport: theory and practice. *McGraw-Hill series in water resources and environmental engineering.* 1996.

[Zhou et al. (2002)] Zhou, F., Hicks, F.E., and Steffler, P.M. (2002). Transient flow in a rapidly filling horizontal pipe containing trapped air. *J. Hydr. Eng.*, DOI: 10.1061/(ASCE)0733-9429(2002)128:6(625).

[Zhou et al. (2004)] Zhou, F., Hicks, F.E., and Steffler, P.M. (2004). Analysis of effects of air pocket on hydraulic failure of urban drainage infrastructure. *Canadian Journal of Civil Engineering.*, DOI: 10.1139/l03-077.

[Zhou et al. (2013)] Zhou, L., Liu, D., and Karney, B. (2013). Investigation of hydraulic transients of two entrapped air pockets in a water pipeline. *J. Hydr. Eng.*, DOI: 10.1061/(ASCE)HY.1943-7900.0000750.

[Zhou et al. (2011)] Zhou, L., Liu, D., and Ou, C. (2011). Simulation of flow transients in a water filling pipe containing entrapped air pocket with VOF model. *Engineering applications of computational fluid mechanics*, DOI: 10.1080/19942060.2011.11015357.

Appendices

Appendix A

CFD model setting

Appendix A provides some relevant input files regarding to the settings of the CFD models presented in current research. The typical structure of a CFD model created with OpenFOAM in current research can be expressed with Figure A.1 (OpenFOAM Foundation, 2016), and contains:

- A *constant/* directory: the physical property and mesh directory;
- A *system/* directory: setting parameter directory;
- A *0/* or *0.org/* directory: the boundary condition and initial condition directory; and
- Other *time* directories: simulation result directories at specific time.

The *constant/* directory contains the model constant physical property files and mesh files, and sometimes contains the model geometry files. Constant physical properties include gravity acceleration g, thermal properties *thermophysicalProperties*, *thermophysicalProperties.air*, *thermophysicalProperties.water*, and turbulence model *turbulenceProperties*, etc. The model mesh information is stored in *polyMesh/* directory, including a list of boundary types and conditions *boundary*, a list of cell vertices *points*, a list of cell faces *faces*, a list of owner cell labels *owner*, a list of neighbour cell labels *neighbour*, etc. The model geometry files with respect to current research are 3D geometric model files in the format of ".stl" stored in *triSurface/* directory.

The *system/* directory contains the setting parameters of the model, including the mesh generation dictionaries *blockMeshDict* and *snappyHexMeshDict* for setting up blockMesh and snappyHexMesh utilities, respectively, time control dictionary *controlDict*, parallel computing control dictionary *decomposeParDict*, customized initial condition initialization dictionaries *setFieldsDict* and *funkySetFieldsDict*, post-processing dictionaries *probeDict* and *sampleDict*, numerical scheme controller *fvSchemes*, equation solvers, tolerances and algorithms controller *fvSolution* etc. For the models simulating porous baffles, a baffle creation dictionary *createBafflesDict* is also set up in this directory.

The *0/* or *0.org/* directory contains files of fluid variables that are solved by the specific CFD solver, such as water volume fraction *alpha.water*, pressure p, velocity U, temperature T, turbulence kinetic energy k, turbulence dissipation ϵ, etc. In each file, specific initial conditions are initialized on each boundary. Other *time* directories are often created as the simulation is running, containing the same variables as directory *0/* or *0.org/* and other interested simulated variables, such as fluid density ρ.

The following sections provide parameters, typical boundary condition and initial condition settings, as well as some control dictionaries of each model presented in this dissertation. For brevity, only one model is provided with respect to chapter 4, 5, 6, and 7. Meanwhile, since all the models can be developed based on the existing tutorials provided by OpenFOAM 4.1, only files with important modifications are provided.

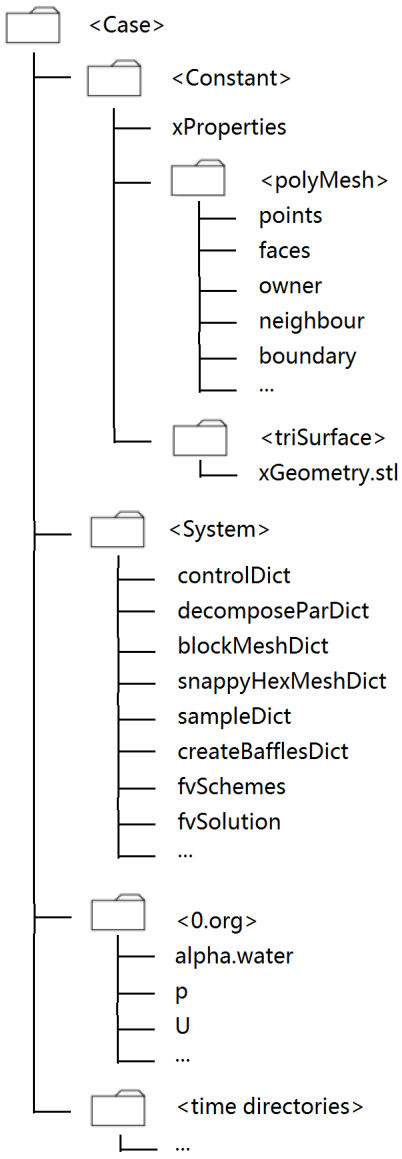

Figure A.1: Typical structure of a OpenFOAM CFD model in current research.

A.1 Geyser model

The CFD model settings of geyser model provided here is from the experimental conditions in Section 4.2.2, Chapter 4. It is developed based on the *depthCharge3D* model of compressibleInterFoam solver tutorial. In this section, the major modification of the model settings are presented below.

The first step of creating a CFD model using OpenFOAM is to develop the geometric model, which is not the focus of this research and relevant steps are skipped here for brevity. Since the geometric model introduced in current section is complex, snappyHexMesh utility is used to generate the mesh and the *snappyHexMeshDict* dictionary is provided here.

```
FoamFile
{
   version 4.0;
   format ascii;
   class dictionary;
   object snappyHexMeshDict;
}

castellatedMesh true;
snap true;
addLayers true;

geometry // Load in STL files here
{
      atmbegin.stl {type triSurfaceMesh; name atmbegin;}
      atmend.stl {type triSurfaceMesh; name atmend;}
      atmout.stl {type triSurfaceMesh; name atmout;}
      main.stl {type triSurfaceMesh; name main;}
      Geyser.stl {type triSurfaceMesh; name Geyser;}
      refinementmain {type searchableBox; min
         ↪  (-0.464 -0.2 -0.153); max (13.748 0.25 0.153);}
      refinementtower {type searchableBox; min (10.0 0.2 -0.2)
         ↪ ; max (10.4 7.5 0.2);}
      refinementbranch {type searchableBox; min (0.81 -0.3 -4)
         ↪ ; max (1.12 0.2 0.48);}
};

castellatedMeshControls
{
   maxLocalCells 1000000; //max cells per CPU core
   maxGlobalCells 8000000; //max cells to use before mesh
      ↪ deletion step
   minRefinementCells 10; //was 0 - zero means no bad cells
      ↪ are allowed during refinement stages
   maxLoadUnbalance 0.10;
   nCellsBetweenLevels 3; // expansion factor between each
      ↪ high & low refinement zone
```

```
// Explicit feature edge refinement
// ~~~~~~~~~~~~~~~~~~~~~~~~~~~~~~~~

features // taken from STL from each .eMesh file created by
   ↪  "SurfaceFeatureExtract" command
(
   {file "atmbegin.eMesh"; level 1;}
   {file "atmend.eMesh"; level 1;}
   {file "atmout.eMesh"; level 1;}
   {file "main.eMesh"; level 2;}
);

// Surface based refinement
// ~~~~~~~~~~~~~~~~~~~~~~~~

refinementSurfaces // Surface-wise min and max refinement
   ↪ level
{
   atmbegin {level (1 1);}
   atmend {level (1 1);}
   atmout {level (1 1);}
   main {level (2 2);}
}

resolveFeatureAngle 80; // Resolve sharp angles // Default
   ↪  30
refinementRegions
{
   refinementmain
   {
      mode inside;
      levels ((1E15 1));
   }
   refinementtower
   {
      mode inside;
      levels ((1E15 2));
   }
   refinementbranch
   {
      mode inside;
      levels ((1E15 1));
   }
}
```

```
    locationInMesh (-2 3 0.1); //to decide which side of mesh
        ↪ to keep **
    allowFreeStandingZoneFaces true;
}


// Settings for the snapping.
snapControls
{
    nSmoothPatch 3;
    tolerance 4.0;
    nSolveIter 30;
    nRelaxIter 5;
    nFeatureSnapIter 15; // default is 10

// New settings from openfoam 2.2 onwards for SHMesh

implicitFeatureSnap false; // default is false - detects
    ↪ without doing surfaceFeatureExtract
explicitFeatureSnap true; // default is true
multiRegionFeatureSnap false; // deafault is false - detects
    ↪ features between multiple surfaces
}

// Settings for the layer addition.
addLayersControls //add the PATCH names from inside the STL
    ↪ file so STLpatchName_insideSTLName
{
    relativeSizes false; // was true
    layers
    {
        refinementmain
              {nSurfaceLayers 3;} // was 3
        refinementtower
              {nSurfaceLayers 3;} // was 3
        refinementbranch
              {nSurfaceLayers 3;} // was 3
    }

    expansionRatio 1.0;
    finalLayerThickness 0.01; //was 0.00016
    minThickness 0.005; //was 0.00008
    nGrow 0; // was 1

    // Advanced settings
```

```
    featureAngle 80; // was 70 //- When not to extrude surface
        ↪ . 0 is flat, 90 is right angle.
    nRelaxIter 3; //- Max# of snapping relaxation iter. Should
        ↪ stop before upon reaching a correct mesh.
    nSmoothSurfaceNormals 1; // Number of smoothing iterations
        ↪ of surface normals
    nSmoothNormals 3; // Number of smoothing iterations of
        ↪ interior mesh movement direction
    nSmoothThickness 10; // Smooth layer thickness over surface
        ↪  patches
    maxFaceThicknessRatio 0.5; // Stop layer growth on highly
        ↪ warped cells
    maxThicknessToMedialRatio 0.3; // Reduce layer growth where
        ↪  ratio thickness to medial distance is large
    minMedianAxisAngle 130; // Angle used to pick up medial
        ↪ axis points
    nBufferCellsNoExtrude 0; // Create buffer region for new
        ↪ layer terminations
    nLayerIter 50; // Overall max number of layer addition
        ↪ iterations
}

// Generic mesh quality settings. At any undoable phase these
    ↪ determine
// where to undo.
meshQualityControls
{
    maxNonOrtho 65;
    maxBoundarySkewness 20;
    maxInternalSkewness 4;
    maxConcave 80;
    minFlatness 0.5;
    minVol 1e-13;
    minTetQuality 1e-9;
    minArea -1;
    minTwist 0.02;
    minDeterminant 0.001;
    minFaceWeight 0.02;
    minVolRatio 0.01;
    minTriangleTwist -1;

    // Advanced

    nSmoothScale 4;
    errorReduction 0.75;
}
```

```
// Advanced

debug 0;

// Merge tolerance. Is fraction of overall bounding box of
   ↪ initial mesh.
// Note: the write tolerance needs to be higher than this.
mergeTolerance 1E-6;
```

The next step is to setup the turbulence model in *constant/turbulenceProperties*:

```
FoamFile
{
   version 4.1;
   format ascii;
   class dictionary;
   location "constant";
   object turbulenceProperties;
}

simulationType RAS;

RAS
{
   RASModel kEpsilon;

   turbulence on;

   printCoeffs on;
}
```

Then, the variables of turbulence model k and epsilon files are added in *0.org/* directory: *k*:

```
FoamFile
{
   version 4.1;
   format ascii;
   class volScalarField;
   location "0";
   object k;
}

dimensions [0 2 -2 0 0 0 0];

internalField uniform 0.1;

boundaryField
{
```

```
   main //walls boundary
   {
      type kqRWallFunction;
      value uniform 0.1;
   }

   atm //atmosphere boundary
   {
      type inletOutlet;
      inletValue uniform 0.1;
      value uniform 0.1;
   }
}
```

epsilon:

```
FoamFile
{
   version 4.1;
   format ascii;
   class volScalarField;
   location "0";
   object epsilon;
}

dimensions [0 2 -3 0 0 0 0];

internalField uniform 0.1;

boundaryField
{
   main
   {
      type epsilonWallFunction;
      value uniform 0.1;
   }

   atm
   {
      type inletOutlet;
      inletValue uniform 0.1;
      value uniform 0.1;
   }
}
```

The *system/fvSchemes* and *system/fvSolution* are also modified for resolving turbulence.
fvSchemes:

```
FoamFile
```

```
{
   version 4.1;
   format ascii;
   class dictionary;
   location "system";
   object fvSchemes;
}

ddtSchemes
{
   default Euler;
}

gradSchemes
{
   default Gauss linear;
}

divSchemes
{
   div(phi,alpha) Gauss vanLeer;
   div(phirb,alpha) Gauss linear;

   div(rhoPhi,U) Gauss upwind;
   div(Phi,U) Gauss upwind;//
   div(phi,thermo:rho.water) Gauss upwind;
   div(phi,thermo:rho.air) Gauss upwind;
   div(rhoPhi,T) Gauss upwind;
   div(rhoPhi,K) Gauss upwind;
   div(rhoPhi,epsilon) Gauss upwind;
   div(rhoPhi,k) Gauss upwind;
   div(Phi,T) Gauss upwind;//
   div(Phi,K) Gauss upwind;//
   div(phi,p) Gauss upwind;
   div(phi,k) Gauss upwind;
   div(phi,epsilon) Gauss upwind;//

   div(((rho*nuEff)*dev2(T(grad(U))))) Gauss linear;//
   div((muEff*dev2(T(grad(U))))) Gauss linear;
}

laplacianSchemes
{
   default Gauss linear uncorrected;
}

interpolationSchemes
```

```
{
   default linear;
}

snGradSchemes
{
   default uncorrected;
}

fluxRequired
{
   default no;
   p_rgh;
   pcorr;
}
```

fvSolution:

```
FoamFile
{
   version 4.1;
   format ascii;
   class dictionary;
   location "system";
   object fvSolution;
}

solvers
{
   alpha.water
   {
      nAlphaCorr 1;
      nAlphaSubCycles 1;
      cAlpha 1;
   }

   pcorr
   {
      solver PCG;
      preconditioner
      {
         preconditioner GAMG;
         tolerance 1e-05;
         relTol 0;
         smoother DICGaussSeidel;
         nPreSweeps 0;
         nPostSweeps 2;
         nFinestSweeps 2;
```

```
        cacheAgglomeration true;
        nCellsInCoarsestLevel 10;
        agglomerator faceAreaPair;
        mergeLevels 1;
    }
    tolerance 1e-05;
    relTol 0;
    maxIter 100;
}

".*(rho|rhoFinal)"
{
    solver diagonal;
}

p_rgh
{
    solver GAMG;
    tolerance 1e-07;
    relTol 0.01;
    smoother DIC;
    nPreSweeps 0;
    nPostSweeps 2;
    nFinestSweeps 2;
    cacheAgglomeration true;
    nCellsInCoarsestLevel 10;
    agglomerator faceAreaPair;
    mergeLevels 1;
}

p_rghFinal
{
    solver PCG;
    preconditioner
    {
        preconditioner GAMG;
        tolerance 1e-07;
        relTol 0;
        nVcycles 2;
        smoother DICGaussSeidel;
        nPreSweeps 2;
        nPostSweeps 2;
        nFinestSweeps 2;
        cacheAgglomeration true;
        nCellsInCoarsestLevel 10;
        agglomerator faceAreaPair;
        mergeLevels 1;
```

```
        }
        tolerance 1e-07;
        relTol 0;
        maxIter 20;
    }

    "(U|e|k|epsilon).*"//
    {
        solver smoothSolver;
        smoother symGaussSeidel;
        tolerance 1e-06;
        relTol 0;
        minIter 1;
    }

    "(T|B|nuTilda).*"//
    {
        solver smoothSolver;
        smoother symGaussSeidel;
        tolerance 1e-08;
        relTol 0;
    }
}

PIMPLE
{
    momentumPredictor no;
    transonic no;
    nOuterCorrectors 1;
    nCorrectors 2;
    nNonOrthogonalCorrectors 0;
}
```

The water volume fraction and pressure distribution settings are initialized in *system/setFieldsDict* and *system/funkySetFieldsDict*, respectively.

setFieldsDict:

```
FoamFile
{
    version 4.1;
    format ascii;
    class dictionary;
    location "system";
    object setFieldsDict;
}

defaultFieldValues
(
```

```
   volScalarFieldValue alpha.water 0
);

regions
(
   boxToCell
   {
      box (-1.1 -0.3 -0.8382) (14.5 2.5 0.153);
      fieldValues
      (
         volScalarFieldValue alpha.water 1
      );
   }

   boxToCell
   {
      box (-3.1 1.8 -1.1) (-0.9 2.5 1.1);
      fieldValues
      (
         volScalarFieldValue alpha.water 1
      );
   }

   boxToCell
   {
      box (14 1.8 -1.1) (16.5 2.5 1.1);
      fieldValues
      (
         volScalarFieldValue alpha.water 1
      );
   }
);
```

funkySetFieldsDict:

```
FoamFile
{
   version 4.1;
   format ascii;
   class dictionary;
   location "system";
   object funkySetFieldsDict;
}

expressions
(
   pressureWater
   {
```

```
        field p; //field to initialise
        expression "9810.*(2.5-pos().y)+100000";
        condition "(pos().y<2.5) && (pos().y>=-1) && (pos().z
            ↪ >=-0.8382)";
        keepPatches 1; //keep the boundary conditions that were
            ↪ set before
    }
    pressureAir
    {
        field p; //field to initialise
        expression "9810.*4.6+100000";
        condition "(pos().y<0.153) && (pos().y>=-1) && (pos().z
            ↪ <-0.8382)";
        keepPatches 1; //keep the boundary conditions that were
            ↪ set before
    }
    pressureAir
    {
        field p; //field to initialise
        expression "100000";
        condition "(pos().y>2.5)";
        keepPatches 1; //keep the boundary conditions that were
            ↪ set before
    }
);
```

Another major change is on post-processing dictionary *system/sampleDict*, sampling pressure at the selected location.

```
FoamFile
{
    version 4.1;
    format ascii;
    class dictionary;
    object sampleDict;
}

setFormat raw;

surfaceFormat vtk;

formatOptions
{
    ensight
    {
        format ascii;
    }
}
```

```
interpolationScheme cellPoint;

fields
(
      p
);

sets
(
   somePoints
   {
      type cloud;
      axis xyz;
      points (
                  (1.62 -0.07 -0.13)
                  (10.2 -0.1045 -0.1045)
                  (10.2 1.403 -0.076)
            );
   }
);
```

A.2 Manhole cover displacment model

In this section, relevant changes in the Inertial Surge Model in Chapter 5 are presented. It should be noted the model setup is very similar as the previous section and the only difference is on the inlet and outlet boundaries. The inlet and outlet boundary and initial conditions are provided as below for $0.org/alphat$, $0.org/alpha.water$, $0.org/epsilon$, $0.org/k$, $0.org/nut$, $0.org/p$, $0.org/p\_rgh$, $0.org/T$, $0.org/T.air$, $0.org/T.water$, and $0.org/U$, respectively.

alphat:

```
   "inlet.*"
   {
      type calculated;
      value  uniform 0;
   }
   outlet
   {
      type calculated;
      value uniform 0;
   }
```

alpha.water:

```
   "inlet.*"
   {
      type fixedValue;
      value  uniform 1;
```

```
}
outlet
{
   type inletOutlet;
   value  uniform 1;
   inletValue uniform 1;
}
```

epsilon:

```
"inlet.*"
{
   type  inletOutlet;
   inletValue uniform 0.00931;
   value uniform  0.00931;
}
outlet
{
   type inletOutlet;
   inletValue uniform 0.0574;
   value uniform 0.0574;
}
```

k:

```
"inlet.*"
{
   type  inletOutlet;
   inletValue uniform 0.0158;
   value uniform  0.0158;
}
outlet
{
   type inletOutlet;
   inletValue uniform 0.0531;
   value uniform 0.0531;
}
```

nut:

```
"inlet.*"
{
   type calculated;
   value  uniform 0;
}
outlet
{
   type calculated;
   value uniform 0;
}
```

p:

```
"inlet.*"
{
   type fixedValue;
   value uniform 100000;
}
outlet
{
   type fixedValue;
   value uniform 58872;
}
```

p_rgh:

```
"inlet.*"
{
   type fixedFluxPressure;
   gradient uniform 0;
   value  uniform 100000;
}
outlet
{
   type fixedValue;
   value uniform 58872;
}
```

T:

```
"inlet.*"
{
   type fixedValue;
   value  uniform 300;
}
outlet
{
   type inletOutlet;
   inletValue uniform 300;
   value uniform 300;
}
```

$T.air$:

```
"inlet.*"
{
   type fixedValue;
   value  uniform 300;
}
outlet
{
   type inletOutlet;
```

```
    inletValue uniform 300;
    value uniform 300;
}
```

$T.water$:

```
"inlet.*"
{
    type fixedValue;
    value  uniform 300;
}
outlet
{
    type inletOutlet;
    inletValue uniform 300;
    value uniform 300;
}
```

U:

```
    "inlet.*"
    {
    type flowRateInletVelocity;
    volumetricFlowRate table
    (
    (0 0)
    (0.1 0.208)
    (0.2 0.394)
    (0.3 0.538)
    (0.4 0.642)
    (0.5 0.710)
    (0.6 0.754)
    (0.7 0.780)
    (0.8 0.783)
    );
    value uniform (0 0 0);
    }
    outlet
    {
    type  zeroGradient;
    value uniform (0 0 0);
    }
```

A.3 Sediment basin model

The model settings provided here are for the sediment basin model with porous baffles in Chapter 6. The model is developed based on the *waterChannel* model using $SSTk-\omega$ turbulence model of the interFoam solver tutorial. The major change during the model developing is to add

a *createBafflesDict* dictionary, presented as below, in the *system/* directory to generate porous baffles in the model.

```
FoamFile
{
   version 4.1;
   format ascii;
   class dictionary;
   object createBafflesDict;
}

internalFacesOnly true;


// Baffles to create.
baffles
{
   cyclicFaces1
   {
      //- Select faces and orientation through a
         ↪ searchableSurface
      type searchableSurface;
      surface searchablePlate;
      origin (5.18 -1.4 -4.3);
      span (0 1.4 8.6);

      patches
      {
         master
         {
            //- Master side patch

            name porous_half0;
            type cyclic;
            neighbourPatch porous_half1;

            //- Optional override of added patchfields. If not
               ↪  specified
            // any added patchfields are of type calculated.
            patchFields
            {
               p_rgh
               {
                  type porousBafflePressure;
                  patchType cyclic;
                  D 2000;
                  I 1000;
                  length 0.02;
```

```
                jump uniform 0;
                value uniform 0;
            }
        }
    }
    slave
    {
        //- Slave side patch

        name porous_half1;
        type cyclic;
        neighbourPatch porous_half0;

        patchFields
        {
            ${...master.patchFields}
        }
    }
  }
}

cyclicFaces2
{
    //- Select faces and orientation through a
      ↪ searchableSurface
    type searchableSurface;
    surface searchablePlate;
    origin (8.53 -1.4 -4.3);
    span (0 1.4 8.6);

    patches
    {
        master
        {
            //- Master side patch

            name porous_half2;
            type cyclic;
            neighbourPatch porous_half3;

            //- Optional override of added patchfields. If not
              ↪  specified
            // any added patchfields are of type calculated.
            patchFields
            {
                p_rgh
                {
```

```
                type porousBafflePressure;
                patchType cyclic;
                D 2000;
                I 1000;
                length 0.02;
                jump uniform 0;
                value uniform 0;
            }
        }
    }
    slave
    {
        //- Slave side patch

        name porous_half3;
        type cyclic;
        neighbourPatch porous_half2;

        patchFields
        {
            ${...master.patchFields}
        }
    }
}

cyclicFaces3
{
    //- Select faces and orientation through a
      ↪ searchableSurface
    type searchableSurface;
    surface searchablePlate;
    origin (11.89 -1.4 -4.3);
    span (0 1.4 8.6);

    patches
    {
        master
        {
            //- Master side patch

            name porous_half4;
            type cyclic;
            neighbourPatch porous_half5;

            //- Optional override of added patchfields. If not
              ↪  specified
```

```
            // any added patchfields are of type calculated.
            patchFields
            {
               p_rgh
               {
                  type porousBafflePressure;
                  patchType cyclic;
                  D 2000;
                  I 1000;
                  length 0.02;
                  jump uniform 0;
                  value uniform 0;
               }
            }
         }
         slave
         {
            //- Slave side patch

            name porous_half5;
            type cyclic;
            neighbourPatch porous_half4;

            patchFields
            {
               ${...master.patchFields}
            }
         }
      }
   }
}
```

A.4 Soil particle resuspension model

This section provides setting information of the soil particle resuspension model in Chapter 7. The model is similar as the model in the previous section but is a 2D model instead of 3D model. When using snappyHexMesh utility to generate 2D model, two dictionaries are required in *system/* directory, including *extrudeMeshDict* and *createPatchDict*:

extrudeMeshDict:

```
FoamFile
{
   version 4.1;
   format ascii;
   class dictionary;
   object extrudeMeshDict;
}
```

```
constructFrom patch;
sourceCase "";
sourcePatches (symFront);

// If construct from patch: patch to use for back (can be same
   ↪ as sourcePatch)
exposedPatchName symBack;

// Flip surface normals before usage. Valid only for extrude
   ↪ from surface or
// patch.
flipNormals false;

//- Linear extrusion in point-normal direction
extrudeModel linearNormal;

nLayers 1;

expansionRatio 1.0;

linearNormalCoeffs
{
   thickness 0.05;
}

mergeFaces false; //true;

mergeTol 0;
```

createPatchDict:

```
FoamFile
{
   version 4.1;
   format ascii;
   class dictionary;
   object createPatchDict;
}

pointSync false;

patches
(
   {
      // Name of new patch
      name front;
```

```
      // Type of new patch
      patchInfo
      {
         type empty;
      }

      // How to construct: either from 'patches' or 'set'
      constructFrom patches;

      // If constructFrom = patches : names of patches.
         ↪ Wildcards allowed.
      patches (symFront);
   }
   {
      // Name of new patch
      name back;

      // Type of new patch
      patchInfo
      {
         type empty;
      }

      // How to construct: either from 'patches' or 'set'
      constructFrom patches;

      // If constructFrom = patches : names of patches.
         ↪ Wildcards allowed.
      patches (symBack);
   }
);
```

Appendix B

Research outcomes

B.1 Published journal manuscripts

1. Wang, J. and Vasconcelos, J.G. Manhole cover displacements created by the release of entrapped air pockets. Journal of Water Management Modeling, February 2018. DOI: 10.14796/JWMM.C444.

2. Simpson, T.D., Wang, J., and Vasconcelos, J.G. Cellular confinement cell strategy to prevent resuspension in sediment basins. ASCE Journal of Environmental Engineering 144, no. 5 (2018): 04018024. DOI: 10.1061/(ASCE)EE.1943-7870.0001363.

3. Muller, K.Z., Wang, J. and Vasconcelos, J.G. Water displacement in shafts and geysering created by uncontrolled air pocket releases. ASCE Journal of Hydraulic Engineering 143, no. 10 (2017): 04017043. DOI: 10.1061/(ASCE)HY.1943-7900.0001362.

B.2 Submitted manuscripts under review

1. Wang, J. and Vasconcelos, J.G. Investigation of manhole cover displacement during rapid filling of stormwater systems. Submitted to ASCE Journal of Hydraulic Engineering, Jun. 2018, HYENG-11287.

B.3 Book chapters under preparation

1. Huang, B., Wang, J., and Vasconcelos, J.G. Geysering. Chap. 23 in ASCE-EWRI: Computational Fluid Dynamics: Applications in Water, Wastewater and Stormwater Treatment, in preparation.

B.4 Conference papers and presentation

1. Wang, J. and Vasconcelos, J.G. Flow characteristics of stormwater geyser created by the release of a sequence of uncontrolled air pockets. In ASCE World Environmental and Water Resources Congress 2018, Minneapolis, MN (Oral Presentation).

2. Wang, J. and Vasconcelos, J.G. Preliminary assessment of a retrofit strategy in dropshafts impacted by geysering using CFD. In ASCE World Environmental and Water Resources Congress 2017, Sacramento, CA (Oral Presentation).

3. Wang, J. and Vasconcelos, J.G. CFD study on the flow patterns in sediments basins during rapid filling conditions. In ASCE World Environmental and Water Resources Congress 2017, Sacramento, CA (Oral Presentation Only).

4. Wang, J. and Vasconcelos, J.G. Manhole lid displacements created by the release of entrapped air pockets. In International Conference On Water Management Modeling 2017, Toronto, CA (Presented by Dr. Vasconcelos).

5. Wang, J., Muller, K., and Vasconcelos, J.G. A Preliminary Assessment of Geysering Simulations Using OpenFOAM. In World Environmental and Water Resources Congress 2016, West Palm Beach, FL (Poster Presentation).

6. Simpson, T., Vasconcelos, J.G., and Wang, J. Cellular Confinement in Sediment Basins. In World Environmental and Water Resources Congress 2016, West Palm Beach, FL.

7. Wang, J. and Vasconcelos, J.G. Numerical simulation of air-triggered geysers using OpenFOAM. In International Conference On Water Management Modeling 2016, Toronto, CA (Presented by Dr. Vasconcelos).

8. Wang, J. and Vasconcelos, J.G. Comparing the trajectories of shockwaves and rarefaction waves from CFD and Saint-Venant models during dambreak events. In ASCE World Environmental and Water Resources Congress 2015, Austin, TX (Oral Presentation).

B.5 Project reports

1. Vasconcelos, J.G., Simpson, T.D., and Wang, J. Research report: Cellular confinement approach for the improvement of sediment basin effectiveness. Feb. 2018.

2. Vasconcelos, J.G., Perez, M.A., Wang, J., Zech, W.C., and Fang, X. Final report: Evaluation of high-rate settling technology for sediment control in roadway construction sites. Jul. 2017.

3. Vasconcelos, J.G., Muller, K.Z., and Wang, J. Final report: Experimental and numerical investigations on geysers caused by the release of large air pockets. Jan. 2017.